

Numerical simulation of permeability heterogeneity in
single- and two-phase flow systems to assess the performance of
enhanced geothermal system

Dissertation for the award of the doctorate (Dr. rer. nat.)
of the Georg-August-University Göttingen

within the doctoral program, Geoscience
of the Georg-August University School of Science (Gauss)

submitted
by Dejian Zhou
from Hefei, Anhui province, China

Göttingen, June 2022

Thesis Committee

Prof. Dr. Martin Sauter

(Department of Applied Geology, Georg-August University of Göttingen)

Dr. Alexandru Tatomir

(Department of Applied Geology, Georg-August University of Göttingen)

Prof. Dr. Ingrid Tomac

(Geo-Micromechanics Research Group, University of California, San Diego)

Members of the Examination Board

Reviewer: Prof. Martin Sauter

(Department of Applied Geology, Georg-August University of Göttingen)

Second Reviewer: Prof. Dr. Ingrid Tomac

(Geo-Micromechanics Research Group, University of California, San Diego)

Further members of the Examination Board:

Dr. Alexandru Tatomir

(Department of Applied Geology, Georg-August University of Göttingen)

Dr. Jannes Kordilla

(Department of Applied Geology, Georg-August University of Göttingen)

Prof. Rui Hu

(School of Earth Science and Engineering, Hohai University)

Prof. Andreas Pack

(Department of Geochemistry and Isotope Geology, Georg-August University of Göttingen)

Date of the oral examination: 27.07.2022

Abstract

The development of Enhanced Geothermal System (EGS) technology leads to the possibility of an extensive application of geothermal energy, which is attractive because of its ability to reduce CO₂ emissions and dependence on traditional fossil fuels. Different from the conventional porous geothermal reservoirs, the EGS reservoirs are located several kilometers underground and formed by artificial fractured zones and surrounding rock matrix. Due to the higher permeability and porosity, the artificial fractured zones determine the fluid flow and heat transfer in EGS reservoirs. Thus, the representation of fractured zones is crucial to investigating the multi-physical processes and energy performances in EGS reservoirs. On the other hand, working fluid is another factor affecting the EGS reservoir performance since the fluid properties, i.e., density and viscosity, play a role in reservoir pressure and heat production rate. This thesis, based on a commercial software, COMSOL Multiphysics, and an open-source research software, DuMu^X, employs 1) fractured zone, 2) the discrete fracture network, and 3) the rough single fracture to represent the natural fractures for the investigation of reservoir performances using scCO₂ and H₂O as working fluids.

In the first part, a three-dimensional thermal-hydraulic-mechanical (THM) coupled model is established with COMSOL Multiphysics. The THM model is validated with analytical solutions and existing published results. The effects of coupled physical processes among multi-fractures are investigated. The results show that the growth of the number and spacing of fracture zone can effectively decrease the pore pressure difference between injection and abstraction wells; it also increases the production temperature at abstraction, the service lifespan, and the heat production rate of geothermal reservoirs.

Then a discrete fracture model considering variable aperture fractures is presented and used to investigate the influence of fracture aperture distribution on EGS reservoir performance. The fracture apertures are randomly distributed within the networks, but

constant for one single fracture. It is found that the coefficient of variation of DFN aperture strongly affects the performance of geothermal reservoir. The heat production rate and outlet temperature can be divided into three stages based on the value aperture variation coefficient. Furthermore, the average heat production rate is proportional to fracture density, but its effect is reduced by increasing the variation coefficient.

Considering scCO₂ as the alternative to H₂O as EGS working fluid, the third part studies the possibility of using scCO₂ as EGS working fluid by comparing the three specific EGS setups: 1) The combined scCO₂-H₂O-EGS; 2) scCO₂-saturated EGS; and 3) H₂O-saturated EGS. The results illustrate that the EGS using scCO₂ as working fluid leads to a much considerably heat production rate and reservoir lifespan compared to H₂O. In addition, H₂O performs worse than scCO₂ at a higher injection rate due to the considerably shorter reservoir service period.

Finally, the roles of preferential flow path within the heterogeneous permeability field played on EGS performance are investigated. It is found that the preferential flow pathway significantly increases the fluid flow rate, such that the breakthroughs of scCO₂ and temperature at production well are advanced. However, a larger number of preferential flow leads to a worse long-term energy performance. On the other hand, the sequestered scCO₂ mass presents an independent, but a proportional relationship with the length and number of preferential flow pathways, respectively. Furthermore, the reservoir using scCO₂ as working fluid has a better energy performance than the reservoir whose working fluid is H₂O.

Acknowledgments

It has been more than three years since I started my Ph.D. work, time flies and things happened. Along with the excitements and expectations, my Ph.D. study begins on 18.11.2018. The sailing to doctor degree is never smooth; experiencing the non-converge models in 2019, the Covid-19 in 2020, and the pressure from paper submission and revision in 2021, finally, I stand before the throne of Ph.D.

Here, I would like to express my appreciation to my parents, supervisors, colleagues, and all my friends who accompany me during the challenging time.

I would like to thank Prof. Martin Sauter for your tremendous support during my Ph.D. period. I am so appreciating that you could give me the opportunity to be a member of the faculty of applied geology, the great support for the application of scholarship, and constructive suggestions for my manuscripts and research.

I am so grateful to Dr. Alexandru Tatomir for being not only a supervisor, but a friend during the last three years. I would express my greatest appreciation to you for your academic support for my research, encouragement when I am disappointed, and patience for my mistakes. The Covid-19 pulls people away, but you are always being my side when I need help.

I would like to thank Dr. Ingrid Tomac for providing me with professional suggestions and information for my research. My horizons are widely broadened and my work is well presented based on the information you provided.

I would like to thank all the committee members, Dr. Jannes Kordilla, Prof. Rui Hu, Prof. Andreas Pack, for reading my PhD thesis and attending my defense. Thank Prof. Dr. Tsing-Fu and Prof. Dr. Auli for their constructive suggestions on establishment of numerical model and discrete fracture networks.

I am grateful for the financial support by China Scholarship Council (CSC) for my working and living at the University of Göttingen.

I would be grateful for all the help and support from my colleagues and friends. Thank Huhao and Quan for the discussion on model development and research direction.

Thank Dr. Feng for the suggestions on PhD thesis. Thanks all my friends for the parties and badminton playing, we share a really happy time.

Special appreciation to my parents and beloved. Thank my father Shenglin and my mother Xinwen for always believing in me for my nearly thirty-year life, and providing me their most selfless love, without whom I could not come to this step. Thank Miss. Shimin for her tremendous patience, continual encouragement, firm confidence through all my PhD period. Great thanks to your support, I love you! Lastly, thank Xiao Guoba, my cat, your gentle meow always dispels my inner irritability.

Contents

List of Figures	viii
List of Tables.....	xii
Chapter 1.....	1
Introduction	1
1.1. Background	1
1.1.1. Enhanced Geothermal System	1
1.1.2. Simulation on EGS reservoir	3
1.1.3. Working fluids.....	5
1.2. Research objective.....	7
1.3. Thesis structure	7
1.4. Reference.....	9
Chapter 2.....	13
Thermo-hydro-mechanical modelling study of heat extraction and flow processes in enhanced geothermal systems	13
2.1. Introduction	14
2.2. Mathematical model of the THM coupled processes in the EGS.....	16
2.3. Numerical simulation of the heat extraction	18
2.3.1. Simulation strategy	18
2.3.2. Geometry and boundary conditions	19
2.3.3. Methodology to estimate the heat production performance.....	20
2.4. Model validation and verification	21
2.4.1 Two-dimensional validation of the coupled thermal- hydraulic model.....	21
2.4.2. Two-dimensional case for the thermal- hydraulic- mechanical couplings	23
2.4.3. Mesh sensitivity analysis.....	24
2.4.4. Validation and verification of the three-dimensional numerical model.....	25
2.5. Simulation results	26
2.6. Conclusion.....	32
2.7. Data availability	34
2.8. Author contribution	34
2.9. Competing interests.....	34
2.10. Acknowledgements	35
2.11. References	35

Chapter 3.	38
Study on the influence of randomly distributed fracture aperture in a fracture network on heat production from an enhanced geothermal system (EGS)	38
3.1. Introduction	40
3.2. Thermo- hydraulic coupled numerical model	43
3.2.1. Governing equations	44
3.2.2. Model verification.....	46
3.3. Generation of discrete fracture networks	48
3.3.1. Fracture configuration.....	48
3.3.2. Methodology	49
3.4. Numerical model	52
3.4.1. Modelling strategy	52
3.4.2. Monte-Carlo method	52
3.4.3. Model description	52
3.4.4. Definition of characteristic parameters	55
3.5. Results analysis	56
3.5.1. Effects of the number of realizations	56
3.5.2. Effects of coefficient of variation.....	58
3.5.3. Effect of fracture density.....	65
3.5.4. Effects from fracture aperture and fracture density.....	67
3.6. Conclusion.....	69
3.7. Appendix:	70
3.8. Acknowledgements	73
3.9. References	73
Chapter 4.	77
Assessment of EGS Performance Employing Supercritical CO ₂ and H ₂ O as Working Fluids in a Fractured-Porous Reservoir by Two-Phase Flow Modelling	77
4.1. Introduction	78
4.2. Methodology	81
4.2.1. Problem definition.....	81
4.2.2. Numerical and Mathematic model	84
4.2.3. Parameters for evaluating the geothermal reservoir performance.....	87
4.2.4. Initial and boundary conditions.....	87
4.2.4. Sensitivity analysis concerning the discretization.....	89
4.3. Results	90
4.3.1. Comparison of the geothermal reservoirs performances using working fluids scCO ₂ and H ₂ O.....	90
4.3.2. Sensitivity analysis with respect to the impact of injection rate	96

4.3.3. Effects of final cooldown production temperature on EGS performance	100
4.6. Discussion and Conclusions.....	102
4.7. Acknowledgment	104
4.8. References	104
Chapter. 5	109
Effects of Heterogeneous Fracture Permeability on the Performances of an Enhanced Geothermal System	109
Abstract	110
5.1. Introduction	110
5.2. Methodology	114
5.2.1 Mathematical and numerical model	114
5.2.2 Parameters for assessing the geothermal reservoir performance	116
5.2.3 Problem definition.....	117
5.2.4 Heterogeneous distribution of fracture permeability.....	120
5.2.5 Monte Carlo Method.....	121
5.3. Results	123
5.3.1 Effects of standard deviation on reservoir performances	123
5.3.2 Effects of the correlation length on the reservoir performance	130
5.3.3. Effects of the type of working fluid on reservoir performance	134
5.4. Conclusion.....	137
Chapter 6.	143
Conclusion and Outlook.....	143
6.1. Conclusion.....	143
6.1.1. The effects of multi-fracture zones on EGS reservoir performance.....	143
6.1.2. The influences of DFNs properties on EGS reservoir performance.....	144
6.1.3. The advantage of scCO ₂ as working fluid of EGS reservoir over H ₂ O.....	145
6.1.4. The role of preferential flow path on the performance of EGS reservoir using scCO ₂ as working fluid.	145
6.1.5. General conclusion of the thesis.....	146
6.2. Current research and Outlook.....	147
6.2.1. Current research	147
6.2.2. Outlook	147

List of Figures

Figure 1.1: Conceptual models for modeling of a fractured porous medium [29]. 4

Figure 2.1. Geometry and scenarios for the numerical simulation (Scenario 1: single fracture zone; Scenario 2: two parallel fracture zones with tight spacing; Scenario 3: two parallel fracture zones with loose spacing; Scenario 4: three parallel fracture zones). 19

Figure 2.2. Geometry of the single fracture TH model 21

Figure 2.3. Comparison between analytical solution and numerical simulation 23

Figure 2.4. Geometry of the thermal consolidation THM model 23

Figure 2.5. Comparison between analytical solution and numerical simulation 24

Figure 2.6. (a) Sensitivity analysis with respect to finite element mesh and (b) Sensitivity analysis with respect to distance between fracture zone and domain boundary 25

Figure 2.7: Pore pressure difference with time for the two numerical simulators, i.e. current THM model implemented in COMSOL Multiphysics and Figueiredo et al (2020) using TOUGH-FLAC 26

Figure 2.8. Temperature distribution at 30th year for 4 scenarios..... 28

Figure 2.9. (a) Pressure evolution over time and (b) Temperature evolution over time for the four modelling scenarios (the middle and side for scenario 4 indicate the fracture zones located in the middle part and the side parts, respectively). 29

Figure 2.10. Reservoir heat production rates variation with time for the four modelling scenarios. 30

Figure 2.11. Evolution of (a) pressure difference and (b) temperature at the production well for different flow rates (Scenario 2). 32

Figure 2.12. Evolution of energy production with time for three flow rates (Scenario 2). 32

Figure 3.1. Geometrical representation of the lower-dimensional fracture model used for validation, with the position of the fracture walls forming the aperture, **2df**, in an equal-dimensional model 47

Figure 3.2. Comparison between the analytical solution and the numerical simulation 48

Figure 3.3. Generation of discrete fracture networks followed by the simplification for obtaining the one used in numerical simulations. (a) the initial generated DFN; (b) eliminating the isolated fractures (red lines), (c) eliminating the fractures with dead ends (red lines); (d) remaining backbone fracture network. 50

Figure 3.4. Model concepts for a fracture aperture [36]. 51

Figure 3.5. Schematic representation of the partial raster- element concept, from natural to modelling. 52

Figure 3.6. Simulated geometries of the six backbone DFNs (1000m in length × 200m in height).....	55
Figure 3.7. Simulated average heat production rates as a function of the number of realizations for all six scenarios (mean aperture of 0.7mm and coefficient of variation of 1).57	
Figure 3.8. Pore pressure distributions with $\sigma_r = 0, 0.2, \text{ and } 0.6$ at 5 th and 30 th years.....	58
Figure 3.9. Temperature distributions with $\sigma_r = 0, 0.2, 0.6, \text{ and } 1$ at 5 th and 30 th years.....	59
Figure 3.10. the variation of (a) the outlet temperature and (b) the production flow rate over the production time with different coefficient of variations of aperture distributions. Solid lines: the average results of the realizations; colored area, the standard deviation of the realizations.....	60
Figure 3.11. the variation of (a) the heat production rates and (b) the cumulative energy production over the production time with different coefficient of variations of aperture distributions. Solid lines: the average results of the realizations; colored area, the standard deviation of the realizations.....	61
Figure 3.12. (a) Average heat production rate \mathbf{Ar} and (b) the variation of outlet temperature \mathbf{VT} at the end of simulation period as function of the coefficient of variation. Black points and line: the average of fifty realizations, blue points: the results of the realizations.....	62
Figure 3.13. The relationships between the average heat production rate and coefficient of variation for different mean apertures (upper panels) and the relationship between the average heat production rate and mean aperture for different networks (lower panels) at different stage of coefficient of variation (low: $\sigma_r < 0.3$, middle: $0.3 < \sigma_r < 0.6$, and high: $\sigma_r > 0.6$), (a) RG1, (b) RG2, (c) RG3.....	64
Figure 3.14. The relationships between the variation of outlet temperature and coefficient of variation for different mean apertures (upper panels) and the relationship between the variation of outlet temperature and mean aperture for different networks (lower panels) at different stage of coefficient of variation (low: $\sigma_r < 0.2$, middle: $0.2 < \sigma_r < 0.6$, and high: $\sigma_r > 0.6$), (a) RG1, (b) RG2, (c) RG3.	65
Figure 3.15. The relationships of average heat production rate with fracture density for different mean aperture at (a) low coefficient of variation stages, (b) middle coefficient of variation stage, and (c) high coefficient of variation stage.....	66
Figure 3.16. The relationships of average heat production rate with fracture density at three coefficient of variation stages when the mean aperture equals (a) 0.3 mm, (b) 0.5 mm, and (c) 0.7 mm.....	67
Figure 3.17. The relationships of average heat production rate with fracture density for different average aperture at three coefficient of variation stages.....	69
Figure 3.18. The relationships of average heat production rate with coefficient of variation and mean aperture for different discrete fracture networks, (a) RG4, (b) RG5, (c) RG6.....	70

Figure 3.19. The relationships of the variation of outlet temperature with coefficient of variation and mean aperture for different discrete fracture networks, (a) RG4, (b) RG5, (c) RG6.	71
Figure 3.20. Mathematical model for fractured hot dry rock [41]......	72
Figure 3.21. Comparison between the analytical solution and the numerical simulation.	72
Figure 4.1. The generation of discrete fracture network: (a) initial fracture network; (b) the main fractures (white) and isolated fractures (red), and (c) the main fractures.	84
Figure 4.2. Illustration of the boundary conditions of the proposed model and of the main fracture network aperture sizes (in coloured bar).	88
Figure 4.3. Representation of the different grid discretization and the corresponding finite element numbers.....	90
Figure 4.4. Relationship between scCO ₂ saturation at the production well in 30 th year and mesh refinement (element number).	90
Figure 4.5. Spatial distribution of scCO ₂ saturation after 1, 5, 10, and 20 years.....	91
Figure 4.6. Temperature (top) and fractures (bottom) velocity distributions among the combined scCO ₂ - H ₂ O- EGS, scCO ₂ - saturated EGS, and H ₂ O- saturated EGS after years 5 and 30.	93
Figure 4.7. The relationship between (a) production temperature and (b) heat production rate and production time in the combined scCO ₂ -H ₂ O EGS, scCO ₂ -saturated EGS, and H ₂ O-saturated EGS. The black dash line presents the results without considering the reservoir lifespan, i.e., the production still proceeds when production temperature is lower than 120 °C, and (c) The relationship between heat production rate ("power" in the legend) and scCO ₂ saturation ("Sn" in the legend).....	95
Figure 4.8. The relationship between total produced thermal energy and production time among combined scCO ₂ -H ₂ O EGS, scCO ₂ -saturated EGS, and H ₂ O-saturated EGS. The black dash line presents the results without considering the reservoir lifespan, i.e., the production still proceeds when the production temperature is lower than 120 °C.	96
Figure 4.9. Relationship between (a) production temperature and (b) heat production rate and production rate at an injection rate of 10.71 L/s for the combined scCO ₂ -H ₂ O EGS, scCO ₂ -saturated EGS, and H ₂ O-saturated EGS. The black dashed line presents the results without considering the reservoir lifespan, i.e., the production still processes when the production temperature is lower than 120 °C.	97
Figure 4.10. Relationship between (a) production temperature and production time and (b) heat production rate and the production rate for an injection rate of 24.99 L/s for the combined scCO ₂ -H ₂ O EGS, scCO ₂ -saturated EGS, and H ₂ O-saturated EGS setups. The dashed lines present the results without considering the reservoir lifespan, i.e., the production still progresses even with production temperatures below 120 °C.....	98

Figure 4.11. Temperature distribution when the cold plumes first arrive in the production well with (a) H ₂ O and (b) scCO ₂ as the working fluids for an injection rate of 24.99 L /s.....	99
Figure 4.12. Relationship between total produced thermal energy and production time with injection rates of (a) 10.71 L/s and (b) 24.99 L/s. The black dashed line presents the results without considering the reservoir lifespan, i.e., production still continues even for production temperatures lower than 120 °C.	100
Figure 4.13. Relationship between reservoir lifespan and injection rate with different final cooldown production temperature, i.e., the period before the production temperature drops to specific values: 120 °C, 90 °C, 60 °C, and 30 °C.....	102
Figure 5.1. Illustration of the modelled domain and boundary conditions.....	119
Figure 5.2. Examples of fracture permeability distributions over the change of (a) standard deviations (correlation length is 50), and (b) correlation lengths (standard deviation is 0.5).	121
Figure 5.3. (a)Comparison of the Monte Carlo result (red line from Eq. (12)) and realization results (dashed lines) based on 150 realizations for the CL-STD combination (100, 0.3); and (b) sensitive analysis on cumulatively produced energy over realizations at different time points.	122
Figure 5.4. Monte Carlo results with CL-STD combination of (100, 0.3) for: (a) temperature of production fluid, (b) scCO ₂ production rate, (c) total energy output, and (d) total sequestered scCO ₂ mass.	123
Figure 5.5. Example of scCO ₂ plume spatial distributions corresponding to different STDs at 0.5th, 10th, and 30th year. The “Hom” presents the homogeneous permeability distribution. For heterogeneous permeability field, the correlation length is kept as 100.	125
Figure 5.6. Example of scCO ₂ velocity distributions with different STDs at 1st, 10th, and 30th year. The Hom presents the homogeneous permeability distribution. The high velocity areas (red areas) represent the preferential flow pathway of scCO ₂ . The correlation length for the heterogeneous permeability field is kept as 100.....	125
Figure 5.7. The variation of production scCO ₂ saturation over the production period with different STDs: (a) long-term, i.e., 30 years, production, (b) short-term, i.e., first 3 years, production. The “Hom” in legend presents the homogeneous case.	127
Figure 5.8. (a) scCO ₂ production rate, and (b) production temperature over production period with different standard deviation (“STD” in the legend, and “Hom” represents the homogeneous permeability field). The correlation length is kept as 100.....	129
Figure 5.9. The relationship of (a) Cumulative produced energy and (b) the total sequestered scCO ₂ mass with production period with different STD, “Hom” donates the homogeneous permeability field. The correlation length is kept as 100.	130

Figure 5.10. Example of scCO ₂ velocity distributions with different CLs at 1st, 10th, and 30th year. The high velocity areas (red areas) represent the preferential flow pathway of scCO ₂ . The STD for the heterogeneous permeability field is kept as 0.3.	131
Figure 5.11. (a) Relationship between scCO ₂ saturation at production well and production period with different correlation length of gauss distribution; and (b) Relationship between scCO ₂ saturation at production well and correlation length at different time points. The standard deviation is kept as 0.3.....	132
Figure 5.12. Variation of (a) scCO ₂ production rate and (b) production temperature per time as a function of CL. The STD is kept as 0.3.....	133
Figure 5.13. The variation of (a) cumulative produced energy and (b) total mass of sequestered scCO ₂ over the production period for different CL. The STD is kept as 0.3.....	134
Figure 5.14. Comparison of the cumulative energy produced over the entire production period of a geothermal reservoir using scCO ₂ and H ₂ O as working fluids. The permeability is isotropic and homogeneous.	135
Figure 5.15. Relationships among energy variation, STD and CL in different production periods for (a) scCO ₂ -H ₂ O combined EGS, (b) H ₂ O-saturated EGS, (c) scCO ₂ -H ₂ O combined EGS, and (d) H ₂ O-saturated EGS.....	137

List of Tables

Table 2.1. Parameters used in models	20
Table 2.2. Parameters for single fracture model.....	22
Table 2.3. Cumulative produced energy for 4 scenarios at 30 th year.	30
Table 3.1. Parameters for the single fracture TH model validation.....	47
Table 3.2. Parameters of fracture network generation.....	53
Table 3.3. Parameters for the simulations	54
Table 3.4. Combinations of mean aperture and coefficient of variations.....	57
Table 4.1. Parameters for the simulations	88
Table 4.2. Relationships between Peclet number (Pe), temperature breakthrough time, and heat production rate.	93
Table 5.1. Parameter values for modelling of the geothermal system.....	119

Chapter 1.

Introduction

1.1. Background

After the third industrial revolution, the financial requirement increased with the economic and technological developments. According to a theoretical approximation, the total energy consumption worldwide is 4.0×10^{20} J [1], in which 81.3% of the energy is supported by the traditional fossil fuels, i.e., oil (31.6%), coal (26.9%), and natural gas (22.8%). The use of fossil fuels produces 34.81-billion-ton greenhouse gas into the atmosphere, which plays an essential role in global warming and climate anomalies [2]. As an alternative to fossil fuels, green energy, especially geothermal energy, has generally been attractive over the decades in the new century due to its low-carbon generation and environmental friendliness [3], [4].

Traditional geothermal energy is stored in hot water within hot wet rocks (HWR), in which the naturally reservoir exists with high porosity and permeability. However, such HWRs are rare and unevenly distributed worldwide. Nearly 98% of the geothermal energy is stored in hot dry rocks (HDR), in which no natural water is available [5]. The HDRs, whose temperatures range between 150°C and 650°C, are widely distributed over the world [6]. However, the application of geothermal energy is usually restricted by the HDRs location. Generally, the HDRs are located in the 3-10km underground, where the low permeability and porosity are the main obstacle for successful geothermal energy extraction [7]. Thus, the application of geothermal energy is still challenging and requires further development.

1.1.1. Enhanced Geothermal System

To overcome the restriction of low permeability and porosity on the geothermal energy application within the HDRs, a new technology has been developed recently. It forms

a so-called Enhanced Geothermal System or Engineered Geothermal System (EGS) in underground structures [8]. The EGS is a man-made fractured reservoir where hot rocks are available. The most common approach for creating an EGS reservoir is by the injection of cold fracturing fluid into the subsurface to increase the rock permeability and porosity by the generation of new fractures or re-opening of the pre-existing fractures. The increased permeability allows the circulation of the working fluid through the newly formed fractured zone [9]. Then the application of the geothermal energy is achieved by extracting the hot working fluid heated by the surrounding hot rocks from the production well.

The investigations on EGS have been generally implemented worldwide since the first EGS effort at Fenton Hill in the 1970s and 1980s [10]. An EGS reservoir was first created in Fenton Hill at a depth of approximately 2.6km underground with a temperature of 185°C. The experiments in Fenton Hill were sustained for approximately one year, and the results demonstrated that the geothermal energy could be extracted at a reasonable production rate from the EGS reservoir.

Up to date, the world's major economies, i.e., the United States, Germany, France, United Kingdom, Australia, and China, have been invested into the development and test of EGS reservoirs [11]–[18]. Australia has the largest EGS project in the world, whose energy production rate reached to nearly 25 MW. The successful operation of the EGS project in Australia proves the feasibility of extracting heat sources in the deep HDRs in EGS reservoirs [19].

However, the researches on EGS reservoir are not a straightforward process. One primary factor restricting the development of EGS reservoirs is the induced seismicity, which results from the injection of working fluid into the HDRs. Depending on rock properties and injection pressure, the HDRs may respond with tensile failure and generate induced seismicity [20]. The magnitudes of induced seismicity are gradually lower than that of earthquakes and tremors [21]. Pohang of South Korea observed the maximum observed magnitude, i.e., 5.5, related to EGS projects in 2017, as a result, the EGS project was stopped in the following month of the event [15]. Similarly, the

induced seismicity also leads to the cancellation of the EGS tests in Basal of Swaziland in December 2009 [22]. Therefore, the currently existing EGS projects are primarily small-scale to avoid to the generation of induced seismicity. Besides the environmental problem, i.e., the induced seismicity, the high cost of the field experiments within EGS reservoirs is another factor affecting the EGS development. The initial investments of the field experiments consist of the cost for the creation of high permeable rock matrix and the purchasing of required fluids, which are usually ranged between several hundred thousand to several million euros [23].

The high investment and potential environmental damage caused by induced seismicity indicate that the conductions of field experiments on EGS reservoirs are challenging. As an alternative, the numerical simulations provide an additional tool for studying and understanding the performance of EGS reservoirs with the rapid development of computation technology. Recently, the mathematical models capable of handling the thermal, hydraulic, mechanical, and chemical (THMC) coupled processes were developed and implemented within different numerical simulators [24]–[27]. The THMC model can simulate the fluid flow, phase migration, thermal transfer, rock deformation, and chemical reactions in the fractured underground structures and becomes a solid approach to investigating the multi-physical processes in EGS reservoirs. For example, the Fenton Hill EGS reservoir is simulated by hydraulic-chemical coupled model and thermal-hydraulic coupled model is employed to simulate the Qiabuqia EGS reservoir [10], [16].

1.1.2. Simulation on EGS reservoir

Different from the conventional geothermal reservoirs within porous media, EGS reservoirs are based on fractured rocks, where numerous fractures form the flow pathway of the working fluids. Compared to porous media, fractured rocks are more considerably heterogeneous. Thus, the conventional single-porosity models, in which the behaviors of the geological structures, i.e., fractures and rocks, are represented by a single porous media, are not available for the simulation of the EGS reservoir. The ability of well simulating the fractures is essential to developing numerical models for

EGS reservoirs. **Figure 1.1** summarizes the common method to simulate the EGS reservoirs. The discrete fracture network (DFN) model can well present the fractures, but ignore the interaction between fractures and the surrounding rock matrix. In this case, the dual-porosity models, i.e., the discrete fracture model (DFM) and multi-continuum model, are usually employed. The dual-porosity model assumes that a porous medium can be separated into two distinct pore systems, which have separate flow and solute transport properties and are characterized by two governing equations [28]. A step further, the dual-porosity models can be divided into single-dimensional models and multi-dimensional models.

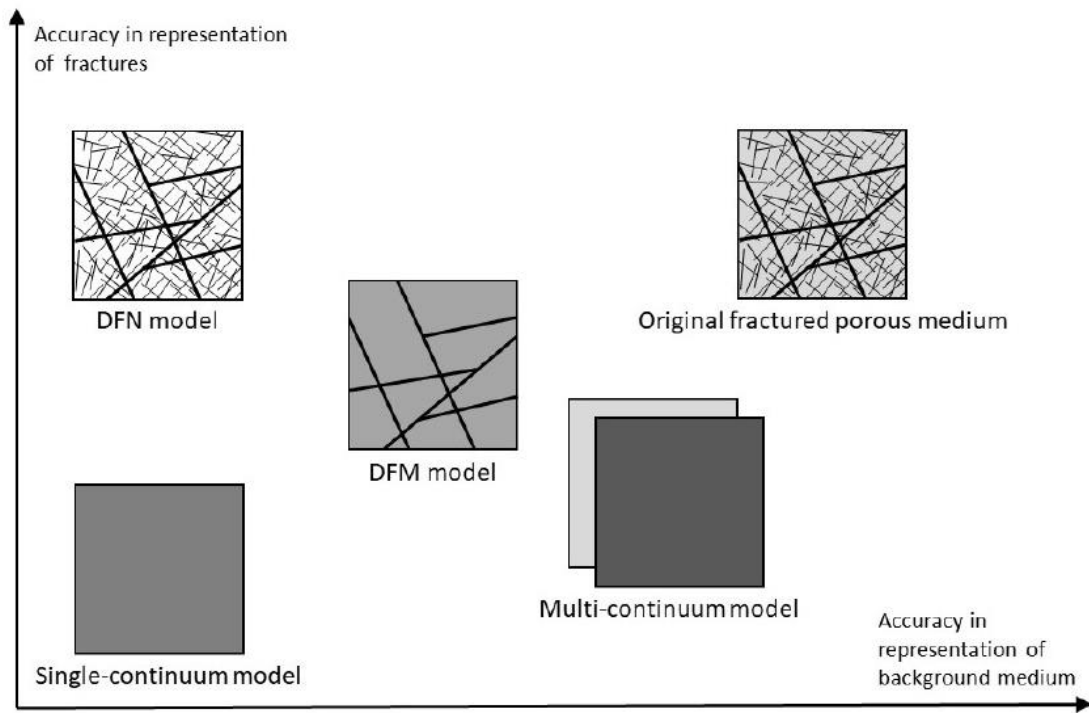


Figure 1.1: Conceptual models for modeling of a fractured porous medium [29].

The single-dimensional model divides the geological structure into rocks and a fractured zone, in which the fractured zone is in the same dimension as the rocks [30]. On the other hand, the multi-dimensional model employed a fracture group with a higher-dimensional rock, e.g., the one-dimensional (1D) fractures with two-dimensional (2D) rocks or the 2D fractures with three-dimensional (3D) rocks. The

fracture group usually indicates the fracture networks [7], [24], [31], [32], or just a single fracture [26]. The fracture networks can well represent the natural fracture with a considerable computation cost. Generally, the conceptual models for the fracture network can be divided into two categories: 1) the parallel plate concept, the one commonly employed in the simulations; 2) the raster-element concept [33]. The limitation of the parallel plate concept is that it cannot take into account the preferential flow path caused by fracture roughness, while the raster-element concept is restricted by the computation capacity. Recently, a new concept, called the partial raster-element concept, has been raised, with which the two concepts are combined, i.e., preferential flow is considered with the acceptable computation cost [7]. A detailed description of the partial raster-element concept will be given in Chapter 3. On the contrary, the primary advantage of a single fracture is the computation cost is low. In this case, the simulation of high heterogeneity of fractures becomes possible. The fracture permeability could vary over each element within the fracture, which makes the 2D plane be a better representative of the natural fracture. An example that the applying single fracture to investigate the effects of fracture heterogeneity on reservoir performances is presented in Chapter 5.

1.1.3. Working fluids

Besides fracture properties, the working fluids also play an essential role in the performance of EGS reservoirs. Unlike the conventional geothermal reservoir in which water is the only possibility, the EGS reservoir has a high diversity of working fluids [34]–[38]. Due to the different fluid properties, the reservoir performances, such as the energy output rate, lifespan, and environmental impact, may vary considerably with working fluids. Currently, water is the primary working fluid for the field experiments in EGS reservoirs. However, since the possibility of employing other fluids was firstly raised by Pruess in 2006 [39], [40], the related studies have been continuously increasing. Supercritical carbon dioxide (scCO₂), due to its physical properties and easy accessibility, becomes the competitive alternative to water in EGS reservoirs [41]–[43]. Former researches indicate that using scCO₂ as working fluid leads to an up to five

times larger heat flow rate than employing H₂O as the working fluid for a given geothermal reservoir [27], [34]. Furthermore, the scCO₂-based reservoirs can maintain a more stable heat production rate and a longer service period compared to H₂O-based reservoirs due to the low injection pressure and later thermal breakthrough time [44]. Additionally, the low injection pressure restricts the possibility of seismicity induced by working fluid injection, which decreases the environmental damage from the operations in EGS reservoirs.

On the other hand, under the background of global warming, which is considered as the result of the over emission of CO₂, using scCO₂ as an EGS reservoir working fluid is believed to benefit in mitigating the continuously increasing temperature. The EGS reservoirs are usually enriched with calcite (CaCO₃), anorthite (CaAl₂Si₂O₈), kaolinite (Al₂Si₂O₅(OH)₄), and other minerals, which react with scCO₂ during the working fluid circulation [45]–[47]. These geochemical reactions benefit the sequestration of scCO₂ underground. Furthermore, the mineral consumptions during geochemical reactions increase the reservoir porosity and permeability, which may enhance the existing preferential flow path or create some new paths. As a result, the production rates of working fluid and energy are promoted for a given injection pressure [48].

The current numerical investigations on scCO₂-based EGS reservoirs are primarily either the single-phase multi-dimensional model, i.e., the working fluid and the fluid which initially saturated the reservoir are both scCO₂, or the multi-phase single-dimensional model, i.e., the fractures and surrounding rocks are regarded as an equivalent continuum. As aforementioned, both the models cannot sufficiently represent the fluid flow, phase displacement, and thermal transfer in fractured porous media. The studies based on the two-phase multi-dimensional model are rare. In this case, a fully coupled thermal-hydraulic (TH) model with a discrete fracture network is established to investigate and compare the performances of EGS reservoirs using scCO₂ and H₂O as working fluid, respectively in chapter 4.

A step further, due to the buoyance force of scCO₂ within H₂O saturated reservoir, the scCO₂ migration is affected by both the buoyance force and preferential flow path. Thus,

the preferential flow path may play a different role on scCO₂-based EGS from H₂O-based EGS. The effects of preferential flow path on the performances of H₂O-based EGS have been widely investigated, but the related research on scCO₂-based EGS is minimal. In this case, Chapter 5 studies the role of preferential flow path played on the performances, i.e., cumulative produced energy and sequestered scCO₂ mass, of scCO₂-based EGS with statistical method.

1.2. Research objective

The main objectives of this thesis are intended to deepen the better understanding of the coupled physical processes in fractured geothermal reservoirs, and provide reliable references and suggestions on designing, developing, and operating the EGS reservoirs.

The main objectives are summarized as follows:

1. Understanding the thermal-hydraulic-mechanical effects of fracture zone number and spacing on the overall pressure at injection and production wells and reservoir temperature distribution.
2. Investigating the effects of 1) the fracture aperture distribution of discrete fracture networks (DFNs) and 2) DFNs densities on the EGS reservoir performance; and providing the suggestions for increasing the reservoir heat production rate.
3. Identifying the ad- and disadvantages of scCO₂ as the reservoir working fluid compared to H₂O regarding the reservoir energy production rate, production temperature, and service period.
4. Determination of the effects of preferential flow path within heterogeneous permeability field on the short-term and long-term reservoir performances, i.e., the cumulative produced energy and sequestered CO₂ mass.

1.3. Thesis structure

This doctoral thesis is structured as a monography and consists of 6 chapters, which contain the overall introduction, the methodology, results of the main research, and the

conclusions.

Chapter 1 gives a general introduction to the research background, motivation, shortage of current research and the primary research objectives, and the structure of the thesis.

Chapter 2 focuses on the thermal-hydraulic-mechanical (THM) effects among fracture zones, in which a dual-porosity single-dimensional THM model is established. The model is validated with analytic solutions and existing published results. The results from the systems of single fracture zone and multi-fracture zone are investigated and compared, and the sensitivity analysis on flow rate is also implemented.

Chapter 3 investigates the effects of fracture aperture distributions and fracture density on the EGS reservoir performances by the Monte Carlo method, in which a discrete fracture model considering the variable aperture fractures is presented. The statistically generated fracture networks with different apertures are applied, where the partial-raster concept is used, i.e., fracture apertures are randomly distributed within the networks, but constant for one single fracture. Based on the comparison between fracture aperture and fracture density, suggestions on promoting reservoir energy performance are provided.

Chapter 4 compares the performance of scCO₂ with H₂O as the EGS reservoir working fluid based on three specific EGS setups: 1) the combined scCO₂-H₂O-EGS; 2) scCO₂-saturated EGS; and 3) H₂O-saturated EGS. The EGS performance is evaluated with fluid production temperature and the heat production rate. In addition, this chapter considers an advanced representation of DFN, which includes the partial-raster concept for the fracture aperture and allows a more realistic representation of the geothermal reservoir.

Chapter 5 studies the influences of preferential flow on the performance of two-phase enhanced geothermal systems with heterogeneous permeability fields. It is assumed that the reservoir is initially saturated with H₂O and the permeability follows gauss distribution with two controlling variables, i.e., standard deviation and correlation. Furthermore, the performance of the reservoir using scCO₂ as working fluid is

compared with the reservoir whose working fluid is H₂O.

Chapter 6 summarizes the conclusions regarding to the primary objectives of the thesis and describes the ongoing and further researches.

1.4. Reference

- [1] IEA, Key World Energy Statistics 2020, IEA, Paris, 2020, <https://www.iea.org/reports/key-world-energy-statistics-2020>.
- [2] IEA, Global Energy Review: CO₂ Emissions in 2021, IEA, Paris, 2022, <https://www.iea.org/reports/global-energy-review-co2-emissions-in-2021-2>.
- [3] G. Hutterer, Geothermal Power Generation in the World 2015-2020 Update Report, Proceedings World Geothermal Congress 2020, Reykjavik, Iceland, April-October 2021.
- [4] S.-M. Lu, “A global review of enhanced geothermal system (EGS),” *Renew. Sustain. Energy Rev.*, vol. 81, pp. 2902–2921, Jan. 2018, doi: 10.1016/j.rser.2017.06.097.
- [5] Armstead, H C.H., and Tester, J W. Heat mining. United States: N. p., 1986. Web..
- [6] D., Brown, The US hot dry rock program-20 years of experience in reservoir testing, World Utilization of Geothermal Energy: an Indigenous, Environmentally Benign Renewable Energy Resource, Proceedings of the World Geothermal Congress, Florence, Italy, May 18-31, 1995
- [7] D. Zhou, A. Tatomir, A. Niemi, C.-F. Tsang, and M. Sauter, “Study of Fracture Aperture Variation in a Fracture Network on Heat Production from an Enhanced Geothermal System (EGS),” *SSRN Electron. J.*, 2021, doi: 10.2139/ssrn.3918922.
- [8] P. Olasolo, M. C. Juárez, M. P. Morales, S. D’Amico, and I. A. Liarte, “Enhanced geothermal systems (EGS): A review,” *Renew. Sustain. Energy Rev.*, vol. 56, pp. 133–144, Apr. 2016, doi: 10.1016/j.rser.2015.11.031.
- [9] C. R. Chamorro, J. L. García-Cuesta, M. E. Mondéjar, and A. Pérez-Madrado, “Enhanced geothermal systems in Europe: An estimation and comparison of the technical and sustainable potentials,” *Energy*, vol. 65, pp. 250–263, Feb. 2014, doi: 10.1016/j.energy.2013.11.078.
- [10] D.W., Brown, D.V., Duchane, G., Heiken, V.T., Hriscu. (2012). Serendipity—A Brief History of Events Leading to the Hot Dry Rock Geothermal Energy Program at Los Alamos. In: Mining the Earth's Heat: Hot Dry Rock Geothermal Energy. Springer Geography. Springer, Berlin, Heidelberg. https://doi.org/10.1007/978-3-540-68910-2_1
- [11] T. Ader *et al.*, “Design and implementation of a traffic light system for deep geothermal well stimulation in Finland,” *J. Seismol.*, vol. 24, no. 5, pp. 991–1014, Oct. 2020, doi: 10.1007/s10950-019-09853-y.
- [12] J. Albaric *et al.*, “Monitoring of induced seismicity during the first geothermal reservoir stimulation at Paralana, Australia,” *Geothermics*, vol. 52, pp. 120–131, Oct. 2014, doi: 10.1016/j.geothermics.2013.10.013.

- [13] T. T. Cladouhos, S. Petty, M. W. Swyer, M. E. Uddenberg, K. Grasso, and Y. Nordin, “Results from Newberry Volcano EGS Demonstration, 2010–2014,” *Geothermics*, vol. 63, pp. 44–61, Sep. 2016, doi: 10.1016/j.geothermics.2015.08.009.
- [14] H. Ito, “Inferred role of natural fractures, veins, and breccias in development of the artificial geothermal reservoir at the Ogachi Hot Dry Rock site, Japan: ROLE OF NATURAL FRACTURES IN HDR RESERVOIR,” *J. Geophys. Res. Solid Earth*, vol. 108, no. B9, Sep. 2003, doi: 10.1029/2001JB001671.
- [15] K.-H. Kim, J.-H. Ree, Y. Kim, S. Kim, S. Y. Kang, and W. Seo, “Assessing whether the 2017 M_w 5.4 Pohang earthquake in South Korea was an induced event,” *Science*, vol. 360, no. 6392, pp. 1007–1009, Jun. 2018, doi: 10.1126/science.aat6081.
- [16] Z. Lei *et al.*, “Exploratory research into the enhanced geothermal system power generation project: The Qiabuqia geothermal field, Northwest China,” *Renew. Energy*, vol. 139, pp. 52–70, Aug. 2019, doi: 10.1016/j.renene.2019.01.088.
- [17] I. Stober, “Depth- and pressure-dependent permeability in the upper continental crust: data from the Urach 3 geothermal borehole, southwest Germany,” *Hydrogeol. J.*, vol. 19, no. 3, pp. 685–699, May 2011, doi: 10.1007/s10040-011-0704-7.
- [18] G. Zimmermann, I. Moeck, and G. Blöcher, “Cyclic waterfrac stimulation to develop an Enhanced Geothermal System (EGS)—Conceptual design and experimental results,” *Geothermics*, vol. 39, no. 1, pp. 59–69, Mar. 2010, doi: 10.1016/j.geothermics.2009.10.003.
- [19] Heinz-Gerd Holl, “What did we learn about EGS in the Cooper Basin?,” 2015, doi: 10.13140/RG.2.2.33547.49443.
- [20] Massachusetts Institute of Technology, Ed., *The future of geothermal energy: impact of enhanced geothermal systems (EGS) on the United States in the 21st century: an assessment*. Cambridge, Mass.: Massachusetts Institute of Technology, 2006.
- [21] C. J. Bromley and M. A. Mongillo, “Geothermal Energy from Fractured Reservoirs - Dealing with Induced Seismicity -,” p. 7.
- [22] M. Baer *et al.*, “Earthquakes in Switzerland and surrounding regions during 2006,” *Swiss J. Geosci.*, vol. 100, no. 3, pp. 517–528, Dec. 2007, doi: 10.1007/s00015-007-1242-0.
- [23] P. Olasolo, M. C. Juárez, J. Olasolo, M. P. Morales, and D. Valdani, “Economic analysis of Enhanced Geothermal Systems (EGS). A review of software packages for estimating and simulating costs,” *Appl. Therm. Eng.*, vol. 104, pp. 647–658, Jul. 2016, doi: 10.1016/j.applthermaleng.2016.05.073.
- [24] Z. Sun, “Numerical simulation of the heat extraction in EGS with thermal-hydraulic-mechanical coupling method based on discrete fractures model,” *Energy*, vol. 120, pp. 20–33, 2017, doi: <https://doi.org/10.1016/j.energy.2016.10.046>.
- [25] F. Gong *et al.*, “Evaluation of geothermal energy extraction in Enhanced Geothermal System (EGS) with multiple fracturing horizontal wells (MFHW),”

- Renew. Energy*, vol. 151, pp. 1339–1351, May 2020, doi: 10.1016/j.renene.2019.11.134.
- [26] B. Guo, P. Fu, Y. Hao, C. A. Peters, and C. R. Carrigan, “Thermal drawdown-induced flow channeling in a single fracture in EGS,” *Geothermics*, vol. 61, pp. 46–62, May 2016, doi: 10.1016/j.geothermics.2016.01.004.
- [27] A. Borgia, K. Pruess, T. J. Kneafsey, C. M. Oldenburg, and L. Pan, “Simulation of CO₂-EGS in a Fractured Reservoir with Salt Precipitation,” *Energy Procedia*, vol. 37, pp. 6617–6624, 2013, doi: 10.1016/j.egypro.2013.06.594.
- [28] J. Lee, S.-U. Choi, and W. Cho, “A comparative study of dual-porosity model and discrete fracture network model,” *KSCE J. Civ. Eng.*, vol. 3, no. 2, pp. 171–180, Jun. 1999, doi: 10.1007/BF02829057.
- [29] I. Berre, F. Doster, and E. Keilegavlen, “Flow in Fractured Porous Media: A Review of Conceptual Models and Discretization Approaches,” *Transp. Porous Media*, vol. 130, no. 1, pp. 215–236, Oct. 2019, doi: 10.1007/s11242-018-1171-6.
- [30] D. Zhou, A. Tatomir, and M. Sauter, “Thermo-hydro-mechanical modelling study of heat extraction and flow processes in enhanced geothermal systems,” *Adv. Geosci.*, vol. 54, pp. 229–240, Jun. 2021, doi: 10.5194/adgeo-54-229-2021.
- [31] J. Gong and W. R. Rossen, “Modeling Flow in Naturally Fractured Reservoirs: Effect of Fracture Aperture Distribution on Critical Sub-Network for Flow,” presented at the DFNE 2014: Proceedings of the 1st International Conference on Discrete Fracture Network Engineering, Vancouver, Canada, Oct. 2014.
- [32] A. Frampton, J. D. Hyman, and L. Zou, “Advective Transport in Discrete Fracture Networks With Connected and Disconnected Textures Representing Internal Aperture Variability,” *Water Resour. Res.*, vol. 55, no. 7, pp. 5487–5501, Jul. 2019, doi: 10.1029/2018WR024322.
- [33] Anongnart Assteerawatt, *Flow and transport modelling of fractured aquifers based on a geostatistical approach*. 2008. Accessed: Jun. 17, 2021. [Online]. Available: <https://nbn-resolving.org/urn:nbn:de:bsz:93-opus-36392>
- [34] A. Borgia *et al.*, “Simulations of CO₂ injection into fractures and faults for improving their geophysical characterization at EGS sites,” *Geothermics*, vol. 69, pp. 189–201, Sep. 2017, doi: 10.1016/j.geothermics.2017.05.002.
- [35] G. Cui, S. Ren, B. Dou, and F. Ning, “Geothermal energy exploitation from depleted high-temperature gas reservoirs by recycling CO₂: The superiority and existing problems,” *Geosci. Front.*, p. 101078, Oct. 2020, doi: 10.1016/j.gsf.2020.08.014.
- [36] T. R. Elliot, T. A. Buscheck, and M. Celia, “Active CO₂ reservoir management for sustainable geothermal energy extraction and reduced leakage,” *Greenh. Gases Sci. Technol.*, vol. 3, no. 1, pp. 50–65, Feb. 2013, doi: 10.1002/ghg.1328.
- [37] J. Li, “Numerical investigations of CO₂ and N₂ miscible flow as the working fluid in enhanced geothermal systems,” *Energy*, vol. 206, no. 1, p. 33, Sep. 2020, doi: <https://doi.org/10.1016/j.energy.2020.118062>.
- [38] M. Huang, Y. Jiao, J. Luo, C. Yan, L. Wu, and P. Guan, “Numerical investigation on heat extraction performance of an enhanced geothermal system with supercritical N₂O as working fluid,” *Appl. Therm. Eng.*, vol. 176, p. 115436, Jul.

- 2020, doi: 10.1016/j.applthermaleng.2020.115436.
- [39] K. Pruess, “Enhanced geothermal systems (EGS) using CO₂ as working fluid—A novel approach for generating renewable energy with simultaneous sequestration of carbon,” *Geothermics*, vol. 35, no. 4, pp. 351–367, Aug. 2006, doi: 10.1016/j.geothermics.2006.08.002.
- [40] K. Pruess, “On production behavior of enhanced geothermal systems with CO₂ as working fluid,” *Energy Convers. Manag.*, vol. 49, no. 6, pp. 1446–1454, Jun. 2008, doi: 10.1016/j.enconman.2007.12.029.
- [41] T. Guo, F. Gong, X. Wang, Q. Lin, Z. Qu, and W. Zhang, “Performance of enhanced geothermal system (EGS) in fractured geothermal reservoirs with CO₂ as working fluid,” *Appl. Therm. Eng.*, vol. 152, pp. 215–230, Apr. 2019, doi: 10.1016/j.applthermaleng.2019.02.024.
- [42] O. Kolditz *et al.*, “A systematic benchmarking approach for geologic CO₂ injection and storage,” *Environ. Earth Sci.*, vol. 67, no. 2, pp. 613–632, Sep. 2012, doi: 10.1007/s12665-012-1656-5.
- [43] M. R. Fleming, B. Adams, and M. O. Saar, “Using Sequestered CO₂ as Geothermal Working Fluid to Generate Electricity and Store Energy,” 2020, doi: 10.3929/ETHZ-B-000449690.
- [44] J. Liao *et al.*, “Field scale numerical modeling of heat extraction in geothermal reservoir based on fracture network creation with supercritical CO₂ as working fluid,” *Environ. Earth Sci.*, vol. 79, no. 12, p. 291, Jun. 2020, doi: 10.1007/s12665-020-09001-7.
- [45] R. Xu, L. Zhang, F. Zhang, and P. Jiang, “A review on heat transfer and energy conversion in the enhanced geothermal systems with water/CO₂ as working fluid,” *Int J Energy Res*, p. 20, 2015.
- [46] G. Cui, S. Ren, Z. Rui, J. Ezekiel, L. Zhang, and H. Wang, “The influence of complicated fluid-rock interactions on the geothermal exploitation in the CO₂ plume geothermal system,” *Appl. Energy*, vol. 227, pp. 49–63, Oct. 2018, doi: 10.1016/j.apenergy.2017.10.114.
- [47] A. M. Norouzi, M. Babaei, W. S. Han, K.-Y. Kim, and V. Niasar, “CO₂-plume geothermal processes: A parametric study of salt precipitation influenced by capillary-driven backflow,” *Chem. Eng. J.*, vol. 425, p. 130031, Dec. 2021, doi: 10.1016/j.cej.2021.130031.
- [48] A. Kumar, A. Datta-Gupta, R. Shekhar, and R. L. Gibson, “Modeling Time Lapse Seismic Monitoring of CO₂ Sequestration in Hydrocarbon Reservoirs Including Compositional and Geochemical Effects,” *Pet. Sci. Technol.*, vol. 26, no. 7–8, pp. 887–911, Apr. 2008, doi: 10.1080/10916460701825505.

Chapter 2.

Thermo-hydro-mechanical modelling study of heat extraction and flow processes in enhanced geothermal systems

Dejian Zhou¹, Alexandru Tatomir^{2,1}, and Martin Sauter¹

¹Dept. of Applied Geology, University of Göttingen, Göttingen, 37077, Germany,

²Dept. of Earth Sciences, Geocentrum, Uppsala University, Uppsala, 75236, Sweden

Citation:

Zhou, D., Tatomir, A., and Sauter, M.: Thermo-hydro-mechanical modelling study of heat extraction and flow processes in enhanced geothermal systems, *Adv. Geosci.*, 54, 229–240, <https://doi.org/10.5194/adgeo-54-229-2021>, 2021.

Abstract. Enhanced Geothermal Systems (EGS) are widely used in the development and application of geothermal energy production. They usually consist of two deep boreholes (well doublet) circulation systems, with hot water being abstracted, passed through a heat exchanger, and reinjected into the geothermal reservoir. Recently, simple analytical solutions have been proposed to estimate water pressure at the abstraction borehole. Nevertheless, these methods do not consider the influence of complex geometrical fracture patterns and the effects of the coupled thermal and mechanical processes. In this study, we implemented a coupled thermo-hydro-mechanical (THM) model to simulate the processes of heat extraction, reservoir deformation, and groundwater flow in the fractured rock reservoir. The THM model is validated with analytical solutions and existing published results. The results from the systems of single fracture zone and multi-fracture zones are investigated and compared. It shows that the growth of the number and spacing of fracture zones can effectively decrease the pore pressure difference between injection and abstraction wells; it also increases the production temperature at the abstraction, the service life-spans, and heat production rate of the geothermal reservoirs. Furthermore, the sensitivity analysis on the flow rate is also implemented. It is observed that a larger flow rate leads to a higher abstraction temperature and heat production rate at the end of the simulation, but the pressure difference may become lower.

2.1. Introduction

The Increasing development of geothermal energy has become a central issue globally for its low-carbon generation and environmental friendliness (Sun et al., 2018). However, the exploitation of geothermal energy is widely restricted by reservoir structure and properties. Nearly 98% of geothermal energy is stored within the Hot Dry Rocks (HDRs) (Armstead et al., 1995), whose permeability and porosity are very low. Thus, the low permeabilities being the main obstacle for successful exploitation of the heat resources.

Generally, the HDRs are located 3-10km beneath the ground level, with temperatures

ranging between 150 to 650°C (Brown et al., 1995). The Enhanced Geothermal System (EGS) was developed to overcome the low permeability of HDR systems (Olasolo et al., 2015). An EGS is a man-made reservoir created in the subsurface where hot rocks are available, but they are insufficiently permeable for the high flow rate circulation to be economical. In EGS, the cold fracturing fluid is injected into the subsurface to increase the permeability by dilating pre-existing fractures or creating new ones. The increased permeability allows the fluid underground to circulate through the newly created fracture zones. The hot fluid is abstracted from the abstraction well; then the cold fluid is re-injected into the subsurface to form the circulation. Two main criteria need to be addressed when designing an EGS (Kaya et al., 2010; Rivera et al., 2015; Figueiredo et al., 2020): 1) *temperature at the abstraction well*: if the temperature decreases quickly during the operation, the lifetime of the EGS will be much restricted; 2) *the pore pressure difference between wells of injection and abstraction*; if the pressure difference is too large, the EGS will not be cost-effective, i.e., the cost of injection and abstraction will be too high. Therefore, these two criteria are investigated in our study.

Recently, a mathematical model capable of handling the thermal, hydraulic, and mechanical (THM) coupled processes was developed and implemented within different numerical simulators for the investigation of the performance of the geothermal reservoirs in EGS (e.g., Ogata et al., 2018; Pandey et al., 2018; Danko et al., 2012; Li et al., 2016). The THM numerical model can simulate the migration of fluid, thermal transfer, and matrix deformation in the fractured underground structures and become the suitable approach for investigating the multi-physical processes in EGS. In EGS, usually several artificially fracture zones are created. Usually, these fractures are oriented roughly parallel to each other (Lei et al., 2019). To handle the geometrical complexity of the fracture systems and decrease computational effort, some studies focus on one single fracture zone (e.g., Figueiredo et al., 2020; Knarud et al., 2015). However, this kind of operation ignores the influence from neighbouring fractures and/or fracture zones. Therefore, the heat production rates are likely to be under-or

over-estimated.

The main objective of this study is to apply and test a THM numerical model capable of simulating the coupled THM processes occurring in an EGS. The mathematic model is firstly validated by the analytical solutions, then the THM model consisting of parallel fracture zones is validated with the model proposed by Figueiredo et al. (2020). The model assumes that fractures were already created or re-opened within the fracture zone. Commonly, more fracture zones are present in an EGS. Even though the rock permeability is extremely low and the fracture zones in the EGS are not hydraulically connected, they can influence each other through the stress distribution. Therefore, in this study, we investigate the THM effects induced by the fracture zone number and spacing on the overall pressure and temperature distributions at the injection and extraction wells by comparing the results successively among several sets of parallel fracture zones. Furthermore, a sensitivity analysis on the flow rate is also implemented to investigate the role of flow rate in the heat production process in EGS.

2.2. Mathematical model of the THM coupled processes in the EGS

The mathematical model describing the coupled THM processes involved in EGS is similar to those described by Sun et al. (2018) and Yao et al. (2018).

Darcy's law describes the fluid flow in the subsurface porous system:

$$u_w = -\frac{K}{\mu}(\nabla p - \rho \mathbf{g}) \quad (1)$$

in which, \mathbf{K} is the permeability tensor of the porous media which is assumed to be homogenous and isotropic,

μ is the dynamic viscosity of water. With the mass variation of water being considered:

$$\frac{\partial \rho \phi}{\partial t} - \nabla \cdot \rho \frac{K}{\mu}(\nabla p - \rho \mathbf{g}) + Q = 0 \quad (2)$$

$$\frac{\partial \rho \phi}{\partial t} = \rho S \frac{\partial p}{\partial t} \quad (3)$$

In which S is storage term, here:

$$S = \phi X_f + (1 - \phi) X_m \quad (4)$$

Where ϕ is the initial porosity assumed to be homogeneously distributed, X_f and X_m

are the compressibility of water and surrounding matrix respectively.

Deformation is assumed to be elastic. The force balance equation is given with:

$$\nabla\sigma + F_v = 0 \quad (5)$$

with F_v is the external force, mainly gravity, σ is the stress tensor acting on the matrix. According to previous research (Rutqvist et al., 2002; 2013), the stress-induced mechanical porosity ϕ_{eff} can be expressed by stationary initial porosity ϕ and the volumetric strain ε_v :

$$\phi_{eff} = 1 - (1 - \phi) \exp(-\varepsilon_v) \quad (6)$$

with the volumetric strain being the sum of the axial strain, according to Hook's law and theory of poroelasticity:

$$\varepsilon_{ii} = \frac{1}{E} [\sigma_{ii}' - \nu(\sigma_{jj}' + \sigma_{kk}')] \quad i, j, k = x, y, z \quad (7)$$

$$\sigma_{ii}' = \sigma_{ii} - \alpha_b(p - p_{ref}) \quad (8)$$

where E is the elastic modulus, ν is the Poisson's ratio, σ_{ii}' the effective stress in the porous medium, σ_{ii} is the external stress acting on the matrix, α_b is the biot-coefficient, p is the pore pressure and p_{ref} is the stationary reference pressure. To obtain the effective permeability of surrounding rocks, an empirical relationship between the permeability and porosity has been generally applied (Pashin et al., 1998; Pan et al., 2007; Li et al., 2016; Rutqvist et al., 2002):

$$K_{eff} = K \cdot \exp\left(\frac{\phi_{eff}}{\phi}\right)^n \quad (9)$$

The power-law coefficient n varies with different geological material and structure, usually between 3 to 25 (Rutqvist et al., 2013), in which the value 15 is widely applied in the researches (Rutqvist et al., 2002; 2013; Figueiredo et al., 2020).

In the non-isothermal model, the influence of temperature variations on the strain is also considered, the influence mainly results from thermal expansion and contraction:

$$\varepsilon_{th} = \alpha(T) \cdot (T - T_{ref}) \quad (10)$$

in which ε_{th} is the strain caused by temperature variations, $\alpha(T)$ is the coefficient of thermal expansion, in general, the direction of thermal expansion or contraction depends on the property of the material. Here, all materials are assumed to be

homogeneous; thus $\alpha(T)$ is isotropic. $T - T_{ref}$ is the temperature changes during the non-isothermal injection and abstraction of water. The temperature distribution and thermal transfer is described by the energy conservation equation:

$$(\rho C_{Pw})_{eff} \frac{\partial T}{\partial t} - \rho C_{Pw} u_w \nabla T - \nabla \cdot (k_{eff} \nabla T) + Q = 0 \quad (11)$$

in which, C_p is the heat capacity of water, k is the thermal conductivity, u_w is Darcy velocity, Q is the thermal source and sink, the subscript $_{eff}$ stands for an average value of water and surrounding rocks:

$$(\rho C_{Pw})_{eff} = \phi \rho_w C_{Pw} + (1 - \phi) \rho_m C_{Pm} \quad (12)$$

$$k_{eff} = \phi k_w + (1 - \phi) k_m + k_{disp} \quad (13)$$

where ρ_w , ρ_m , C_{Pw} , C_{Pm} , k_w and k_m are density, heat capacity and thermal conductivity of water and surrounding rocks respectively; k_{disp} is the coefficient of thermal dispersion

2.3. Numerical simulation of the heat extraction

2.3.1. Simulation strategy

The numerical simulator COMSOL Multiphysics is employed to solve the complex coupled partial differential equations, which uses the finite element method for space discretization when solving the system of partial differential equations describing the coupled THM processes. The production strategies for EGS are presented in **Figure 2.1**. Four scenarios have been raised to implement the influence of the fracture structures on the performance of geothermal reservoirs. The blue part presents the fracture zones in which the cold water is injected and hot water is abstracted. Scenario 1 has one fracture zone located in the middle (250m above the lower boundary) of the surrounding rocks; scenario 2 and 3 have two parallel fracture zones, but the zone spacings are different; Scenario 4 has three parallel fracture zones. The total injection and abstraction rates are the same for the four scenarios, i.e., 12L/s (Figueiredo et al., 2020). The rates are assumed to be distributed evenly for the scenarios with multi fracture zones, which means for the scenario 2 and 3, the rate is 6 L/s and the value is 4 L/s for the scenario 4. The heating processes within the injection and abstraction tubes and the preferentially

flow within the fracture zone is ignored.

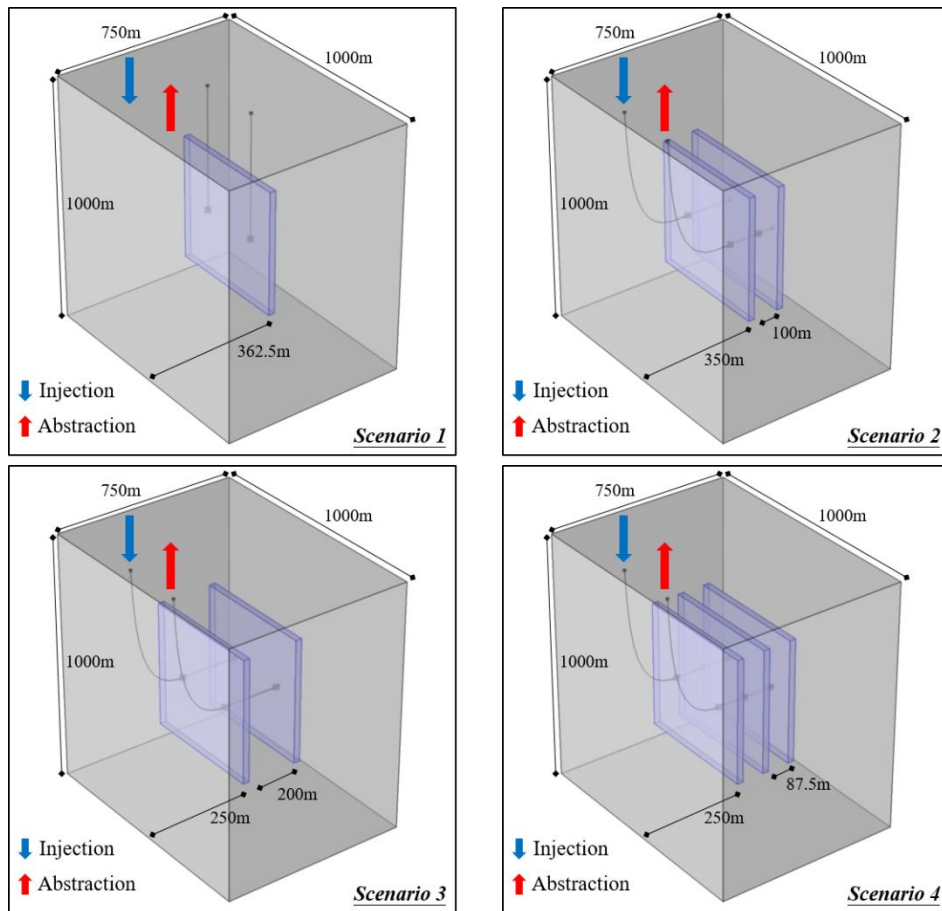


Figure 2.1. Geometry and scenarios for the numerical simulation (Scenario 1: single fracture zone; Scenario 2: two parallel fracture zones with tight spacing; Scenario 3: two parallel fracture zones with loose spacing; Scenario 4: three parallel fracture zones).

2.3.2. Geometry and boundary conditions

The simulated domain size is 1000m by 1000m by 750m, and the size of the fracture zones is 500m by 500m by 25m. The top of the domain is located 6000m below ground level. The x-coordinate axis is parallel to the fracture direction and the z-axis is vertical. The abstraction and injection wells are symmetrical to the centre of the modelling domain. The spacing between the two wells is 250m.

Because of the low permeability of the surrounding rock matrix, it is assumed that water

will not enter the rock material, and all outside model boundaries are assumed tight for fluid flow. A static temperature distribution linearly increasing from 132 °C at the top boundary with a constant thermal gradient of 18 °C/km is assigned (Figueiredo et al., 2020). This temperature gradient has been observed in several sites in Sweden (Ahlbom et al., 1995). It is also assumed that the top and bottom boundaries are at large distances from the fracture zones, and the temperature at the two boundaries is set constant to the initial temperature. The normal displacements are set to be zero for all six boundaries. The initial pressure distribution in the system results from a hydrostatic pressure gradient (9.81MPa/km) and an atmospheric pressure of 0.1 MPa at the surface. This results in the pressure of 63 MPa at the top and 73.4 MPa at the bottom of the domain. The vertical stress distribution is calculated from an overburden density of 2700 kg/m³ and the horizontal stress is set equal to the vertical stress. **Table 2.1** presents the other parameters used in the model. Coldwater is injected into the injection borehole with a temperature of 47 °C. After being heated by the surrounding rocks, the thermal water is abstracted at the abstraction borehole located 250m away from the injection borehole. The total production time is 30 years.

Table 2.1. Parameters used in models

Parameters	Fracture zone	Surrounding rocks
Porosity [-]	0.02	0.02
Permeability [m ²]	1e-14	1e-18
Elastic modulus [GPa]	10	50
Poisson's ratio [-]	0.2	0.2
Rocks density [kg/m ³]	2700	2700
Specific heat capacity of rock [J/(kg*K)]	790	790
Thermal conductivity [W/(m*K)]	2.9	2.9
Thermal expansion coefficient [1/K]	2.5e-4	2.5e-4

2.3.3. Methodology to estimate the heat production performance

In this work, heat production rate (W) and the total produced energy (E) are employed for the judgment of the heat production performance of the aforementioned 4 scenarios. The formulas for W and E are as following:

$$W(t) = \sum_1^n W(t) = \sum_1^n Q(t) \cdot Cp_w \cdot (T_{out}(t) - T_{in}) \quad (14)$$

where n is the number of fracture zones, $Q(t)$ is the production rate, Cp_w is the water capacity and $T_{out}(t)$ and T_{in} are the production temperature and injection temperature respectively.

With the value of total simulation time t_s , the total produced energy can be described:

$$E = \int_0^{t_s} W(t) dt = \int_0^{t_s} \sum_1^n Q(t) \cdot Cp_w \cdot (T_{out}(t) - T_{in}) dt \quad (15)$$

2.4. Model validation and verification

The validation of the THM model is necessary before its further application. The two-dimensional analytical solutions considering fluid flow in single fracture zone is firstly employed to validate our model.

Afterward, the THM model is applied to a realistic three-dimensional EGS system for which no analytical solutions are available, and it is compared with published literature data, i.e., Figueiredo et al., (2020). The hydro-mechanical coupled model, without including the thermal coupling, has been used to perform a verification benchmark with the academic simulator DuMuX (Zhou et al., 2020).

2.4.1 Two-dimensional validation of the coupled thermal- hydraulic model

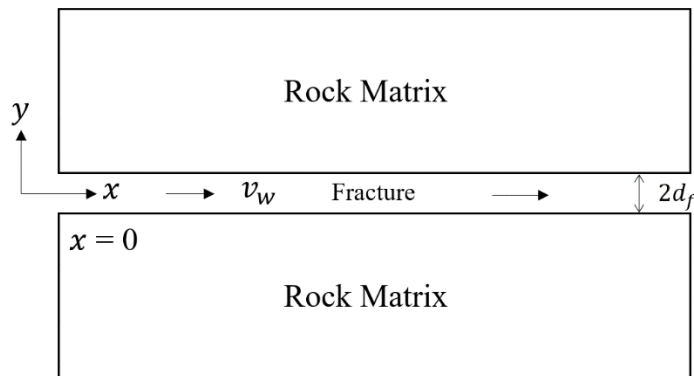


Figure 2.2. Geometry of the single fracture TH model

For the validation of the thermal-hydraulic coupling, the analytical solution proposed by Lauwerier et al. (1955) and Barends et al. (2010) is employed. This solution describes the temperature variation caused by the heat convection and conduction within a single fracture with a given aperture. As presented in **Figure 2.2**, the single fracture is located in the middle of the geometry, surrounded by rock matrices. The thickness of the rock matrices is assumed to be infinite. Heat is transferred by thermal conduction in the rock matrix while heat convection dominates within the fracture. During the heat abstraction, water is injected into the fracture with a constant flow velocity v_f and temperature T_{in} . The analytical solution can be described as following:

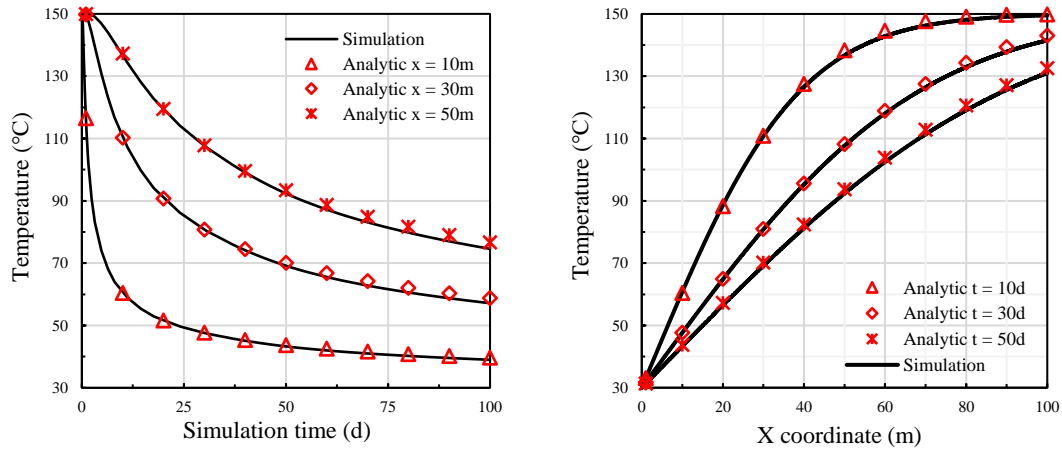
$$T_f = T_0 + (T_{in} + T_0) \operatorname{erfc} \left(\frac{\lambda_s x / (\rho_w C p_w d_f)}{2 \sqrt{v_w (v_w t - x) \lambda_s / (\rho_s C p_s)}} \right) U \left(t - \frac{x}{v_w} \right) \quad (16)$$

where T_0 is the initial temperature of the system, λ_s is the thermal conductivity of the matrix rocks, ρ_w , ρ_s , $C p_w$ and $C p_s$ are the density and heat capacities of water and rock matrix respectively, d_f is the fracture aperture, ‘erfc()’ is the residual error function and ‘U()’ is the unit step function. The detailed value of the parameters for the analytical solution and numerical simulation are presented in **Table 2.2**

Table 2.2. Parameters for single fracture model

Parameters	Value
T_0 (K)	150
T_{in} (K)	30
λ_s (W/m/K)	3
ρ_w (kg/m ³)	1000
ρ_s (kg/m ³)	2700
d_f (mm)	0.1
C_f (J/kg/K)	4200
C_s (J/kg/K)	1000
v_w (m/s)	0.001

The comparisons of numerical simulation with the analytical solution are presented in **Figure 2.3**. **Figure 2.3(a)** illustrates the temperature variation over time at different positions ($x = 10\text{m}$, 30m and 50m). Spatial temperature distribution at different time points ($t = 10\text{d}$, 30d and 50d) is illustrated in **Figure 2.3(b)**.



(a) Temperature evolution over time

(b) Temperature distribution at different potions

Figure 2.3. Comparison between analytical solution and numerical simulation

2.4.2. Two-dimensional case for the thermal- hydraulic- mechanical couplings

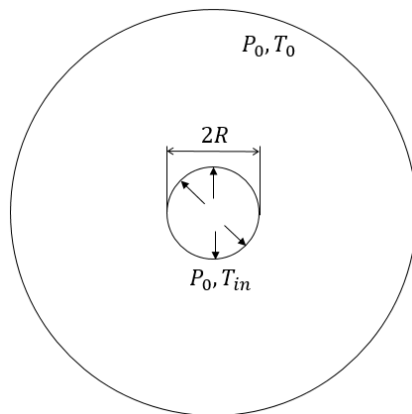
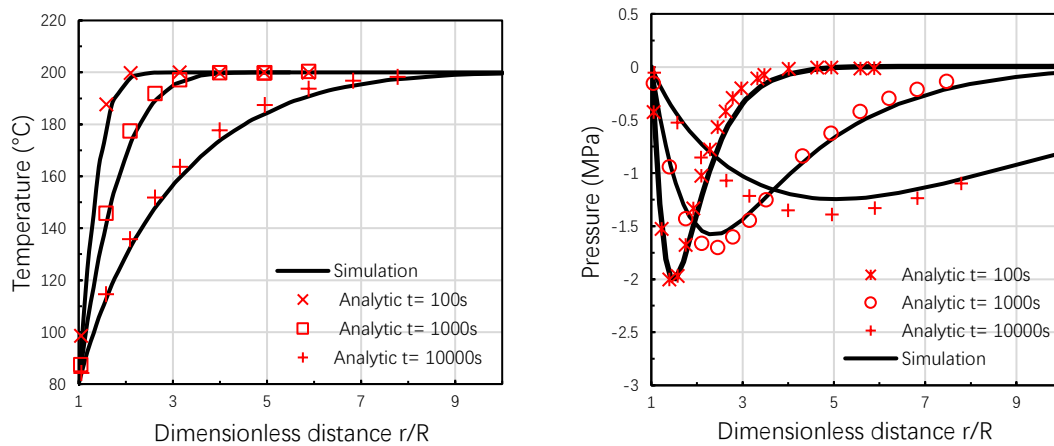


Figure 2.4. Geometry of the thermal consolidation THM model

In this case, the variations of pressure and temperature resulting from the thermal consolidation obtained with the numerical model are compared with the analytical solution. The thermal consolidation problem is a typical problem involving coupled THM effects, i.e., temperature variation, pressure dissipation, and mechanical deformation (Guo et al., 2020), which is the same as the THM coupling effect within

the fractured porous material underground. The analytical solution is proposed by Ghassemi et al. (2004). The geometry of the validation model is presented in **Figure 2.4**. A wellbore with radius $R = 0.1\text{m}$ is located in the middle of the reservoir with an initial temperature of 200°C . The reservoir is assumed to be infinite and fully saturated with water initially. At the beginning of the simulation, the wellbore rapidly is cooled and maintained at 80°C , and the simulation lasts $1 \times 10^4\text{s}$. The other parameters are the same as Ghassemi et al. (2004). **Figure 2.5** presents the comparison results. **Figure 2.5(a)** and **(b)** illustrate the distributions of temperature and pore pressure at different time points. The simulation results have an excellent agreement with the results from the analytical solution for both the cases, which indicates the accuracy and feasibility of the numerical model and its implementation.



(a) Temperature distribution at different time points (b) Pressure distribution at different portions

Figure 2.5. Comparison between analytical solution and numerical simulation

2.4.3. Mesh sensitivity analysis

Scenario 1 is selected for performing a sensitivity analysis with respect to the mesh size. The results for the sensitivity analysis for the mesh and boundaries are presented in **Figure 2.6(a)**. For our numerical model, the mesh of the fracture zone is done with cubical elements and for the surrounding rock matrix, tetrahedral elements. The elements are uniformly distributed within the whole domain. It is observed that the pore

pressure difference between injection and abstraction wells varies with various finite element grids. The pore pressure difference is 6.87 MPa when the number of elements is 12702. With the increase of element number, the pressure difference decreases until the mesh number reaches 15322. From the 15322 elements, the pressure difference remains approximately constant. Therefore, in this paper, a grid with 15322 elements is selected.

Figueiredo et al., (2020) study focused on the EGS performance containing a single fracture zone. The authors did investigate the influence of fracture proximity to the simulation domain boundary. Since the distances between the fracture zone and domain boundaries vary between the different scenarios, a sensitivity analysis regarding the distance is performed (**Figure 2.6(b)**). As expected, the closer to the boundary, the higher the influence is observed, with a high difference between results. The pressure differences increase with increasing distance, and they become smaller (<0.01 MPa) when the distance equals 250m. Thus, the distance of 250m is further used in this work.

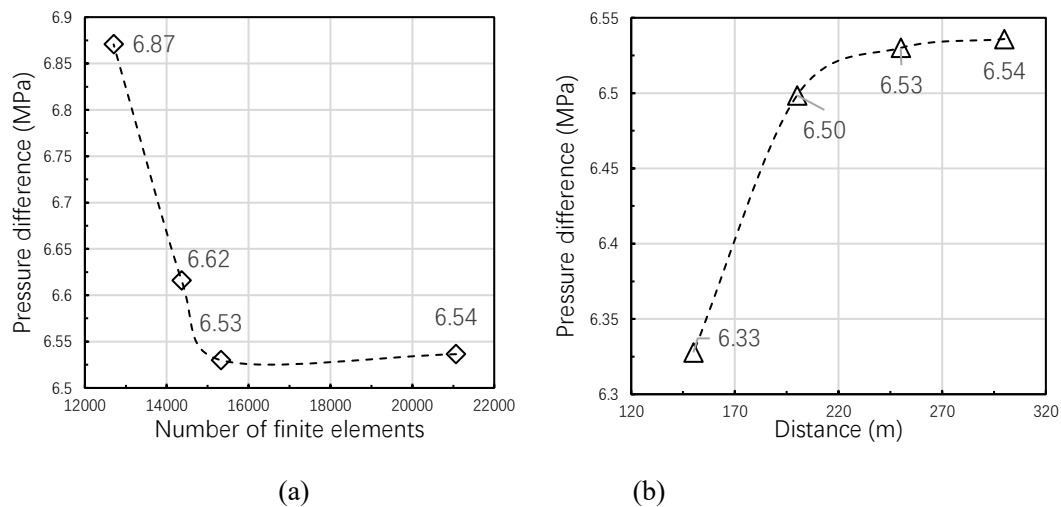


Figure 2.6. (a) Sensitivity analysis with respect to finite element mesh and (b) Sensitivity analysis with respect to distance between fracture zone and domain boundary

2.4.4. Validation and verification of the three-dimensional numerical model

The THM coupled processes are nonlinear and very complex; the validations based

only on the analytical solutions are insufficient. The comparison with the published THM model is necessary and the agreement between different simulators enhances the confidence for our numerical model. This is the purpose of performing the benchmarks (Zhou et al., 2020).

The results obtained with our THM model are compared with Figueiredo et al. (2020) model. The simulated domain size and the parameters employed for our validation model are set to be the same as Figueiredo et al. (2020), i.e., 2000m × 2000m × 110m with a fractured zone of 1000m × 1000m × 10m located in the middle part. The detailed parameters are presented in **Table 2.1**. The finite element mesh setting is the same as the mesh sensitivity analysis, and there are altogether 17876 elements generated in the validation model.

Figure 2.7 presents the pore pressure difference between injection and abstraction wells plotted versus time for the two numerical simulators. It is observed that the results are in very good agreement. The pore pressure difference reaches a peak after ten days of injection, where it remains stable and starts decreasing after approximately 1000 days in both models. The good agreement of the results indicates the THM model is reliable.

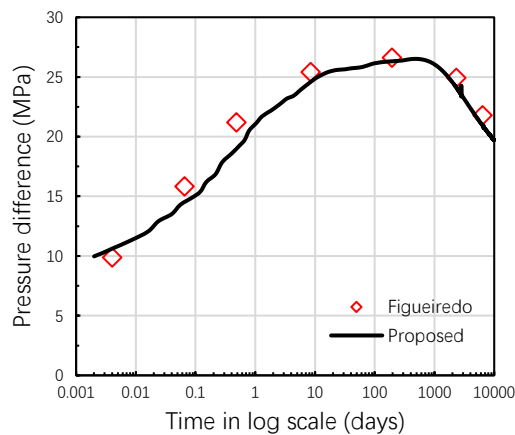


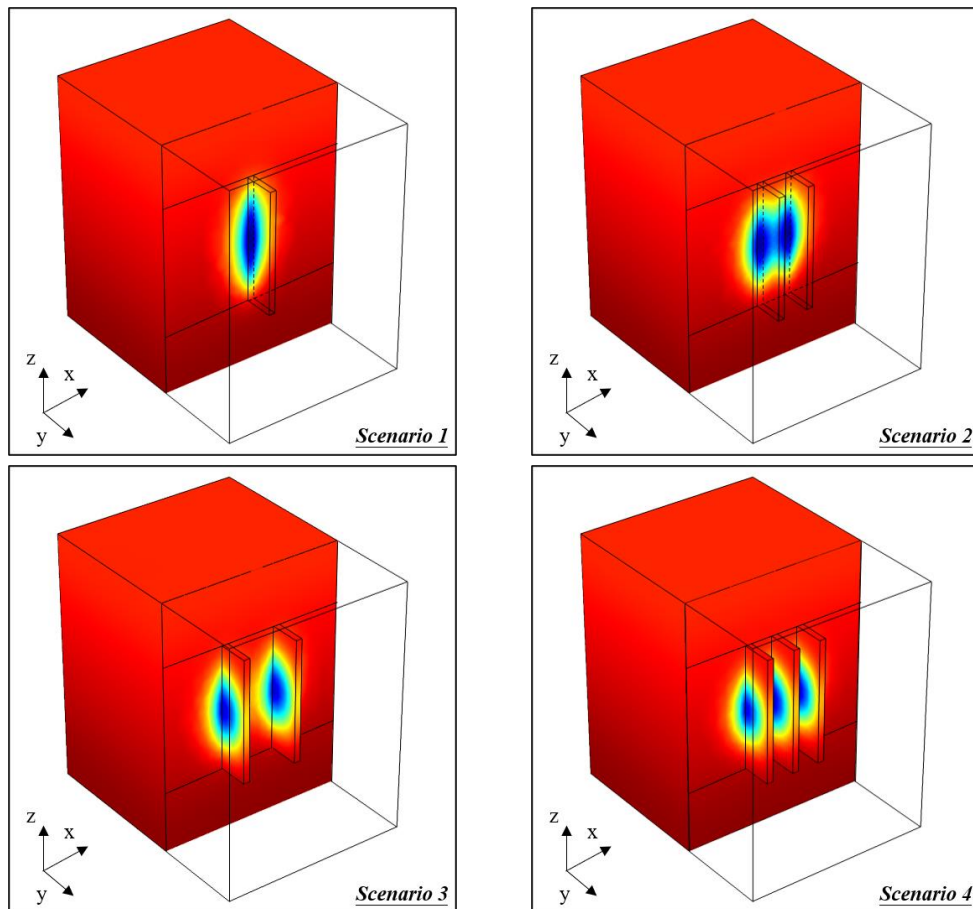
Figure 2.7: Pore pressure difference with time for the two numerical simulators, i.e. current THM model implemented in COMSOL Multiphysics and Figueiredo et al (2020) using TOUGH-FLAC

2.5. Simulation results

Having the model verified with analytical solutions and published results, we studied

the effect of different reservoir characteristics, e.g., single fracture zone compared to the complex (multi-fracture) system on heat production.

Figure 2.8 presents the temperature distribution in the 30th year for the four scenarios. Besides the fracture zones, a flat perpendicular to the fracture zones is also applied to present the heat distribution among the rock matrix. The y coordinate of the perpendicular plane is the same as the value of the injection well. Obviously, the low-temperature zones mainly exist within the fracture zones, and the decrease of temperature is comparably lower in the surrounding rock matrix than that in fracture zones. This is because, within fracture zones, the heat is transferred by both thermal conduction and convection, while due to the lower permeability of the rock matrix, only thermal conduction works within the rock matrix. Additionally, with the increase of the fracture zone number, the vertical extent of the low-temperature zones decreases, but the horizontal extent increases, indicating the connection and influence from the neighboring fractures are enhanced.



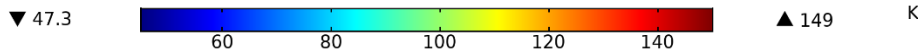


Figure 2.8. Temperature distribution at 30th year for 4 scenarios.

Figure 2.9(a) and (b) presents the comparison of the pore pressure difference between injection and abstraction wells and the abstraction temperature among different scenarios, respectively. It is observed that the pressure difference and production temperature vary with the number, spacing, and location of fracture zones. Scenario 2 and 3 are applied for the investigation of the fracture zone spacing and scenario 4 is used for the fracture zone location. Since the domain is symmetric for scenarios 2, 3, and 4, only the results from one (the one closer to origin) side of the fracture zones are presented here.

As illustrated in **Figure 2.9(a)**, the overall tendencies for all the scenarios are the same, but the discrepancies are apparent. By comparing scenario 1 with scenario 2, 3 and 4, it can be obtained that the multi-fracture system can decrease the pore pressure difference due to the lower injection and abstraction rate. Comparing scenario 2 and 3, the fracture zone spacing has a noticeable influence on the pore pressure difference. The final values are 4.93 MPa and 6.06 MPa, respectively. This indicates the decrease in the distance between the fracture zones can effectively decrease the pore pressure difference. Furthermore, for the three parallel fracture zone system, it is obtained that the middle fracture zone has a comparably lower pressure difference (3.57MPa) than that (4.23 MPa) of the side fracture zone.

The temperature evolutions are presented in **Figure 2.9(b)**. It is observed that during the initial period of the simulation (approx. 500 d), the discrepancies among the scenarios are minimal. This is because, at the beginning of the injection, the energy supply from the near rock matrix is sufficient. The production temperature from scenario 1 firstly decreases at about 500 days. After 2000 d, the production temperatures start to diverge depending on the different fracture zone spacings and their locations. By comparing scenarios 2 with 3, the lower spacing results in a lower temperature at abstraction well. This is because in scenario 2, when the energy stored in the rock matrix

between the two fracture zones is consumed, i.e., the temperature of the rock matrix tends to be the same as the cold water; the rock matrix between two fracture zones can still provide the energy for heating the cold water in scenario 3. Therefore, from this time, the abstraction temperature of scenario 2 begins to be lower than that of scenario 3. The same reason can explain the discrepancy for scenario 4; the middle fracture zone obtains less energy from the surrounding rock matrix, resulting in a higher drop of the temperature at abstraction well. Furthermore, the multi- fracture zone system extends the life-span of the geothermal reservoirs. Provided that the reservoir life-span is the period before the abstraction temperature is lower than 120°C (Guo et al., 2016), the approximately life-span of scenario 1 is the shortest while the life-span of scenario 4 is the longest.

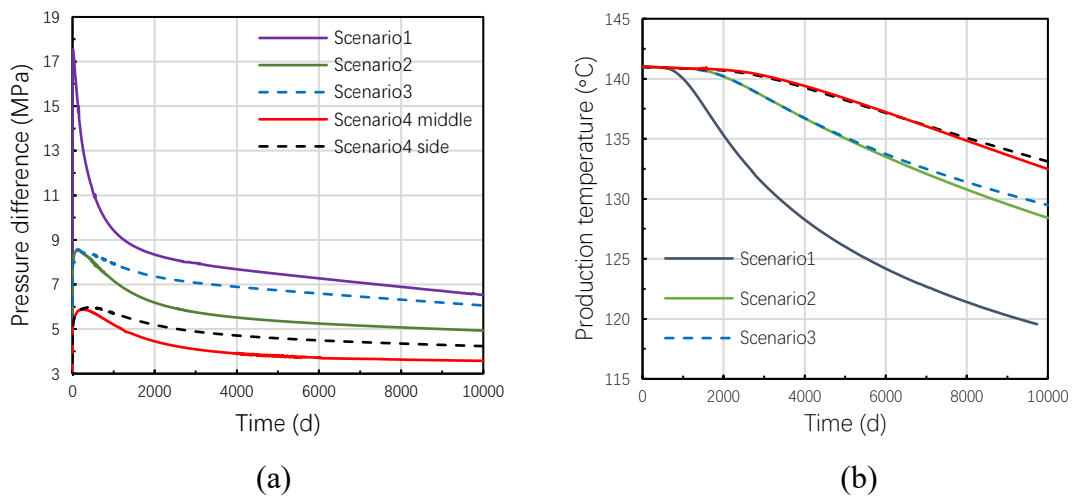


Figure 2.9. (a) Pressure evolution over time and (b) Temperature evolution over time for the four modelling scenarios (the middle and side for scenario 4 indicate the fracture zones located in the middle part and the side parts, respectively).

Figure 2.10 presents the heat production rates over time for the four scenarios. It can be observed that for all the four scenarios, as time passes, the production rates begin to drop from the initial value of 4637 KW. The tendencies of the production rates are all similar with the production temperature at abstraction. For scenario 1, the production rate begins to decrease after approximately 1000 days and drops to 3544 KW at the end of the simulation (10000 days). For the scenario 2 and 3, the breakthrough time is

slightly later, at approximately 1900 days, the drop starts and finally the production reached 4002 kW and 4055 kW respectively. The discrepancy of the production rate for the two scenarios results from the different fracture spacing between the neighbouring fracture zones. For scenario 4, the time for the breakthrough is the latest, at approximately 2400 days. After the breakthrough, the production rate gently decreases to 4225 kW at the end of the simulation.

By comparing the four scenarios, it is observed that the number of the fracture zones is of much higher importance for the performance of the heat production in EGS. With the number increasing from 1 to 3, the final production rates increase from 3544 kW to 4225 kW; the amplitude reaches to nearly 19.2%. Thus, it can be obtained that the multi-fracture zone system can improve the reservoir heat production rate.

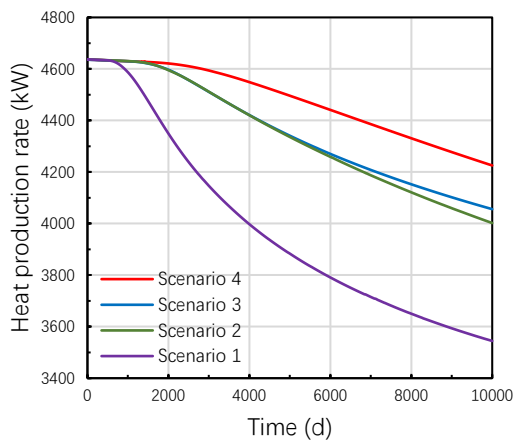


Figure 2.10. Reservoir heat production rates variation with time for the four modelling scenarios.

Table 2.3. Cumulative produced energy for 4 scenarios at 30th year.

Scenario	1	2	3	4
Breakthrough time (day)	1000	1900	1900	2400
Average produced energy (kW)	4.0×10^3	4.35×10^3	4.37×10^3	4.48×10^3

Additionally, the breakthrough time and the cumulatively produced energies of the four scenarios at the 30th year are presented in **Table 2.3**. The breakthrough time is

proportional to the number of the fracture zone, which indicates the energy production of multi- fracture zone reservoir is more stable and enduring than the single- fracture zone reservoir. It is also observed that after the 30-year service time, the variations for different scenarios are noticeable; the maximum discrepancy is 12% from scenario 1 and 4. Thus, it can be concluded that the multi- fracture zone system provides a more stable and robust energy output.

The performance of the geothermal reservoirs for different flow rates is presented in **Figure 2.11**. Scenario 2 is employed for the investigation. It is found that the pressure difference has an initial shoot-up and a subsequent decrease as the simulation progresses. Additionally, the shoot-up and steep reduction are related to the flow rate because of the mechanical response of the fracture zone- matrix system. In the injection well, by injecting the working fluid, the overpressure becomes positive, which leads to an increase of permeability and then a reduction of the overpressure and the same for abstraction well. Meanwhile, the larger flow rate leads to a larger hydro-mechanical effect (a more considerable increase of permeability). Therefore, the subsequent steeper reduction in the pressure difference between the two wells is more evident for the larger flow rate. **Figure 2.11(b)** illustrates the evaluation of outlet temperature over time. It is obvious that the outlet temperature and breakthrough time have an inverse relationship with the flow rate, the larger the flow rate is; the higher and later the outlet temperature and breakthrough time are.

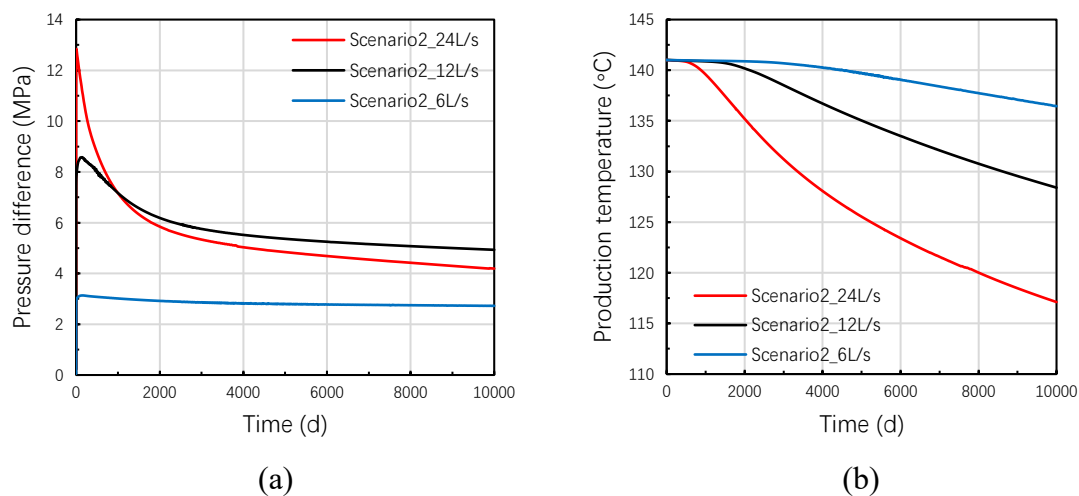


Figure 2.11. Evolution of (a) pressure difference and (b) temperature at the production well for different flow rates (Scenario 2).

Figure 2.12 presents energy production rates and their evolution over time for three flow rates (6, 12, and 24 l/s). It is found that the lowest flow rate has the most stable energy production rate. On the other hand, the largest flow rate results in a higher production rate at the initial injection period, which later decreases slowly. The average energy production rates over the whole simulation time are 7929 kW, 4354 kW, and 2278 kW when the flow rates are 24L/s, 12L/s, and 6L/s, respectively. It shows that the efficiency of reservoir energy production is not strictly proportional to the flow rate, e.g., from 6L/s to 24L/s, the flow rate increases 300%, but the average energy production rate only increases 248%. Thus, the determination of flow rate is of importance to reach the equilibrium of the performances of energy production and economics.

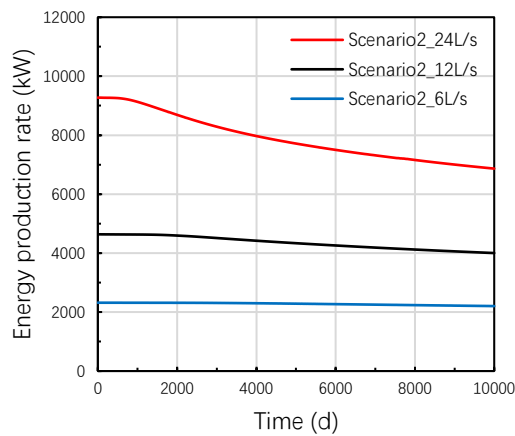


Figure 2.12. Evolution of energy production with time for three flow rates (Scenario 2).

2.6. Conclusion

A thermo-hydro-mechanical (THM) model for studying the cold-water injection in EGS was implemented in a commercial finite element software and here presented. Model validation and verification were conducted by comparing the model results with two

analytical solutions for a two-dimensional idealized domain and the comparison with Figueiredo et al., 2020 THM model in a three-dimensional EGS problem. The very good agreements among the results are a good indicator of the reliability of the numerical model to represent the coupled THM processes characteristic for EGS.

Based on the single fracture zone system raised by Figueiredo et al., 2020, in this study, a sensitivity study is implemented to remove the interference from the mesh setting and the narrow distance between the fracture zone and boundaries which strongly affects the results of the numerical simulation. The influences of the multi-fracture zones and their properties on the EGS reservoir performance are also investigated. In this sense, four scenarios were proposed where the fluid flows through a single-fracture, two- and three- parallel vertical fracture zones. The pressure difference between injection and abstraction wells, heat production rate, and average produced energy are calculated and compared. These are important factors mainly for the assessment of the economics of the geothermal production plant. Above all, the following conclusions can be drawn:

1. From Figure 2.9(a) and (b), it can be obtained that the temperature at the abstraction well is affected by the fracture zone spacing and its location, but only in a limited way, i.e., a lower spacing results in a lower production temperature; the abstraction temperature of middle fracture zone is lower than that of the side fracture zones. However, during the first period (approx. 2000 days), there is almost no difference in temperatures. On the other hand, the spacing and the locations of the fracture zones strongly influence the pore pressure differences.
2. By comparing the production temperatures among the 4 scenarios in Figure 2.9(b), it is observed that the multi- fracture zone system can effectively extend the service life-span of the EGS compared with the single fracture system. The heat production rate and average produced energy are proportional to the number of fracture zones. The highest average energy production rate is obtained with scenario 4, the three-parallel fracture zone system, i.e., 4.48×10^3 kW over 30 years. Additionally, by comparing the results from scenario 2 and 3 in Figure 2.10, the conclusion that a larger spacing between the neighbouring fracture zones leads to a higher heat

production rate can be obtained.

3. The numerical sensitivity analysis concerning the operational flow rates of the EGS reservoir (Fig. 2.11) showed that a larger flow rate results in higher initial pressure difference values, which are subsequently followed by a steeper reduction. Due to the hydro- mechanical effects, the pressure difference from the larger flow rate (24L/s) can be lower than that from the lower flow rate (12L/s). The final outlet temperature and the breakthrough time have an inversely proportional relationship with the flow rate.
4. The relationship between flow rate and average energy production rate is not linear (Fig. 2.12). Higher energy production rates are obtained at higher flow rates but are declining faster than those at lower flow rates.

2.7. Data availability

Some or all data, models, or code generated or used during the study are available in a repository or online in accordance with funder data retention policies (Provide full citations that include URLs or DOIs.)

2.8. Author contribution

Dejian Zhou: Conceptualization; Investigation; Methodology; Software; Validation; Writing – original draft preparation

Alexandru Tatomir: Conceptualization; Methodology; Supervision; Writing – review & editing

Martin Sauter: Supervision

2.9. Competing interests

The authors declare that they have no conflict of interest.

2.10. Acknowledgements

The support provided by China Scholarship Council is acknowledged.

2.11. References

- Armstead, H. C. H., and Tester, J. W.: Heat Mining, E. & F. N. Spon, London and New York, pp. 55–58, 1987
- Barends F. Complete solution for transient heat transport in porous media, following Lauwerier//SPE annual technical conference and exhibition. Society of Petroleum Engineers; 2010.
- Brown, D. The US hot dry rock program-20 years of experience in reservoir testing. In Proceedings of the World Geothermal Congress, Florence, Italy; pp. 2607–2611, 18–31 May 1995
- Danko, G.; Bahrami, D. A New T-H-M-C Model Development for Discrete-Fracture EGS Studies. GRC Trans. 399 2012, 36, 10.
- Figueiredo, B., Tsang, C., Niemi, A. (2020). The Influence of Coupled Thermomechanical Processes on the Pressure and Temperature due to Cold Water Injection into Multiple Fracture Zones in Deep Rock Formation Geofluids 2020(), 1-14. <https://dx.doi.org/10.1155/2020/8947258>. 2020.
- Ghassemi A, Zhang Q. A transient fictitious stress boundary element method for poro-thermoselastic media. Eng Anal Boundary Elem 2004;28:1363–73, 2004.
- Guo, B., Fu, P., Hao, Y., Peters, C., Carrigan, C. (2016). Thermal drawdown-induced flow channeling in a single fracture in EGS Geothermics 61(), 46-62. <https://dx.doi.org/10.1016/j.geothermics.2016.01.004>, 2016.
- H.A. Lauwerier, The transport of heat in an oil layer caused by the injection of hot fluid, Appl. Sci. Res. Sect. A. 5 (1955) 145e150, <https://doi.org/10.1007/BF03184614>, 1955.
- Guo, T., et al., A coupled thermal-hydraulic-mechanical modeling and evaluation of geothermal extraction in the enhanced geothermal system based on analytic hierarchy process and fuzzy comprehensive evaluation Applied Energy, <https://doi.org/10.1016/j.apenergy.2019.113981>, 2019.
- K. Ahlbom, O. Olsson, and S. Sehlstedt, “Temperature conditions in the SKB study sites,” SKB Technical Report 95-15, 1995.
- Kaya, E.; Zarrouk, S.J.; O’Sullivan, M.J. Reinjection in geothermal fields: A review of worldwide experience. Renew. Sustain. Energy Rev. 2011, 15, 47–68, doi:10.1016/j.rser.2010.07.032, 2011.
- Knarud, J., Geving, S. (2015). Implementation and Benchmarking of a 3D Hygrothermal Model in the COMSOL Multiphysics Software Energy Proceedia 78(), 3440-3445. <https://dx.doi.org/10.1016/j.egypro.2015.12.327>, 2015.
- Li, S., Fan, C., Han, J., Luo, M., Yang, Z., Bi, H. (2016). A fully coupled thermal-hydraulic-mechanical model with two-phase flow for coalbed methane extraction

- Journal of Natural Gas Science and Engineering. 33(), 324-336. <https://dx.doi.org/10.1016/j.jngse.2016.05.032>, 2016.
- Lei, Z., Zhang, Y., Zhang, S., Fu, L., Hu, Z., Yu, Z., Li, L., Zhou, J. Electricity generation from an three-horizontal-well enhanced geothermal system in the Qiabuqia geothermal field, China: Slickwater fracturing treatments for different reservoir scenarios *Renewable Energy* 145(), 65-83. <https://dx.doi.org/10.1016/j.renene.2019.06.024>, 2019.
- Massachusetts Institute of Technology. *The Future of Geothermal Energy: Impact of Enhanced Geothermal Systems (EGS) on the United States in the 21st Century*; MIT: Cambridge, MA, USA, 2006.
- Ogata, S.; Yasuhara, H.; Kinoshita, N.; Cheon, D.-S.; Kishida, K. Modeling of coupled thermal-hydraulic- mechanical-chemical processes for predicting the evolution in permeability and reactive transport behavior within single rock fractures. *Int. J. Rock Mech. Min. Sci.* 2018, 107, 271–281, doi:10.1016/j.ijrmms.2018.04.015, 2018.
- Olasolo, P., Juárez, M. C., Morales, M. P., D'Amico, S., & Liarte, I. A. (2016). Enhanced geothermal systems (EGS): A review. *Renewable and Sustainable Energy Reviews*, 56, 133–144. doi:10.1016/j.rser.2015.11.031, 2015.
- Pan, Z., Connell, L.D., 2007. A theoretical model for gas adsorption induced coal swelling. *Int. J. Coal Geol.* 69(4), 243–252.
- Pandey, S.N.; Vishal, V.; Chaudhuri, A. Geothermal reservoir modeling in a coupled thermo-hydro- mechanical-chemical approach: A review. *Earth-Sci. Rev.* 2018, 185, 1157–1169, doi:10.1016/j.earscirev.2018.09.004, 2018.
- Pashin, J., 1998. Stratigraphy and structure of coalbed methane reservoirs in the United States: an overview. *Int. J. Coal Geol.* 35(1), 209-240, 1998.
- Rivera Diaz, A.; Kaya, E.; Zarrouk, S.J. Reinjection in geothermal fields – A worldwide review update. *Renew. Sustain. Energy Rev.* 2016, 53, 105–162, doi:10.1016/j.rser.2015.07.151, 2015.
- Rutqvist, J., Tsang, C. (2002). A study of caprock hydromechanical changes associated with CO₂-injection into a brine formation *Environmental Geology* 42(2-3), 296-305. <https://dx.doi.org/10.1007/s00254-001-0499-2>, 2002.
- Rutqvist, J., Rinaldi, A., Cappa, F., Moridis, G. (2013). Modeling of fault reactivation and induced seismicity during hydraulic fracturing of shale-gas reservoirs *Journal of Petroleum Science and Engineering* 107(), 31-44. <https://dx.doi.org/10.1016/j.petrol.2013.04.023>, 2013.
- Sun, Z.; Xin, Y.; Yao, J.; Zhang, K.; Zhuang, L.; Zhu, X.; Wang, T.; Jiang, C. Numerical Investigation on the Heat Extraction Capacity of Dual Horizontal Wells in Enhanced Geothermal Systems Based on the 3-D 421 THM Model. *Energies* 2018, 11, 280, doi:10.3390/en11020280, 2018.
- Yao, J.; Zhang, X.; Sun, Z.; Huang, Z.; Liu, J.; Li, Y.; Xin, Y.; Yan, X.; Liu, W. Numerical simulation of the heat extraction in 3D-EGS with thermal-hydraulic-mechanical coupling method based on discrete fractures model. *Geothermics* 2018, 74, 19–34, doi:10.1016/j.geothermics.2017.12.005, 2017.
- Zhou D, Tatomir A, Tomac I, Sauter M (2020) Verification benchmark for a single-

phase flow hydro - mechanical model comparison between COMSOL Multiphysics and DuMuX. E3S Web Conf 205:02002. <https://doi.org/10.1051/e3sconf/202020502002>, 2020.

Chapter 3.

Study on the influence of randomly distributed fracture aperture in a fracture network on heat production from an enhanced geothermal system (EGS)

Dejian Zhou¹, Alexandru Tatomir^{2,1}, Auli Niemi², Chin-Fu Tsang², Martin Sauter¹

¹Department of Applied Geology, Geoscience Center Göttingen, University of Göttingen, Germany

²Department of Earth Sciences, Geocentrum, Uppsala University, Uppsala

Citation:

Dejian Zhou, Alexandru Tatomir, Auli Niemi, Chin-Fu Tsang, Martin Sauter, Study on the influence of randomly distributed fracture aperture in a fracture network on heat production from an enhanced geothermal system (EGS), *Energy*, Volume 250, 2022, 123781, ISSN 0360-5442, <https://doi.org/10.1016/j.energy.2022.123781>.

Abstract

In the attempt to reduce the CO₂ emissions to the atmosphere and therefore the dependence on fossil fuels, geothermal energy has started to receive increased scientific interest. With the development of the Enhanced Geothermal System (EGS) technology, extensive geothermal energy applications have become feasible. However, enhanced geothermal reservoirs are usually situated several kilometers below the ground, which makes their experimental investigation challenging. Therefore, numerical models capable of simulating thermohydraulic (TH) effects are an essential additional tool for analyzing geothermal reservoir efficiency. To simulate fluid migration and heat propagation within a fractured geothermal reservoir in EGS, discrete fracture models (DFMs) of the TH processes are widely used. However, the variability of aperture size from one fracture to another is typically ignored in these models. In this work, a discrete fracture model considering variable aperture fractures is presented and used to investigate the performance of a geothermal reservoir in EGS. The outlet temperature and energy production rate are used as the evaluation criteria. Statistically generated fracture networks with different apertures were applied. The fractures are represented as lower-dimensional elements. The fracture apertures are randomly distributed within the networks, but constant for one single fracture. The simulation results show that the coefficient of variation of the DFN apertures strongly affects the performance of the geothermal reservoir. The heat production rate and outlet temperature can be divided into three stages based on the value of coefficient of variation of fracture apertures. The higher variability results in the low heat production rate but high outlet temperature. The investigation on fracture density in turn indicates that the average heat production rate is proportional to the fracture density. However, the effect of fracture density is reduced with an increase of coefficient of variation. Furthermore, the comparison between fracture aperture and fracture density shows that, the increase in mean fracture aperture leads to a higher increase in average heat production rate than an increase in fracture density.

3.1. Introduction

Geothermal energy is gradually becoming a viable energy source that has the potential to play an important role in decarbonizing the power generation. The geothermal energy is widely distributed across the world [1]. According to the theoretical calculations, the amount of geothermal energy stored in the underground structure above the depth of 10 km is approximately 1.3×10^{27} J [2]. Provided that the total annual energy consumption world-wide is 4.07×10^{20} J [3], the current geothermal energy could theoretically satisfy the human energy demand for more than 200 million years [4].

The traditional applications of geothermal energy are based on the natural hot wet rock (HWR). However, such HWR conditions are rare [5]. Most of the geothermal energy is stored 3- 10km beneath the ground level within hot dry rocks (HDR) with temperature ranging between 150°C and 650°C [6]. The low permeabilities of the HDR reservoirs are the main obstacle for the successful exploitation of the geothermal energy. Thus, the application of geothermal energy is still challenging and requires further development.

A new technology has been developed to overcome the restriction of HDR reservoirs. It forms a so-called enhanced geothermal system (EGS) in underground structures [7]. The EGS is like a man-made reservoir, which is created in the subsurface where hot rocks are available, but they are insufficiently permeable for the high flow rate circulation required in order to the reservoir to be economical. The most common approach for creating an EGS reservoir is by the injection of cold fracturing fluid into the subsurface to increase the permeability by the generation of the new fractures or the re-opening of pre-existing fractures. Then, the extraction of geothermal energy is achieved by the circulation of a fluid, e.g., water. The fluid which has a temperature lower than the rock of the geothermal reservoir is circulated through the fractured system, where it heats up and is extracted at another well [8].

Field experiments at depths of several kilometers are expensive and challenging to conduct. thus, numerical modelling provides an additional tool for studying and

understanding the performance of geothermal reservoirs. Many researchers have made their contribution on the development of the numerical modelling to simulate the application of geothermal energy within the EGS [9]–[14]. These models focus on the effect of the coupled multi- physical processes on fluid migration, thermal transfer, and rock matrix deformation in the fractured underground structures. For example, Sun et al. [9] developed a thermal-hydro-mechanical (THM) coupled model consisting of discrete fracture networks and surrounding rock matrix blocks. Their study shows that the THM coupled processes are very important for the investigation of the performance of the EGS. Gong et al. [10] proposed a three-dimensional (3D) thermo-hydraulic (TH) model with multiple fracturing horizontal wells to evaluate the efficiency of the heat extraction in EGS. The presence of multiple fractures significantly increases the fluid flow and heat exchange area which enhances the heat recovery ability. Guo et al. [11] considered the THM coupled processes on the heterogeneity of fracture aperture and studied the influence of aperture heterogeneity on the flow behavior of fluid within a single fracture system. Cao et al. [12] considered also the conservation of fluid momentum, into their numerical model. The 3D THM coupled model was developed based on the local thermal equilibrium concept and applied for the study of THM coupled processes on the heat transfer in EGS. Considering the obviously lower porosity of rock matrix compared with fractures, Xu et al. [13] simplified the equation of energy conservation by replacing the term heat conduction with a self- deduced term, which can be treated as a heat sink. Zhou et al., [14] built a 3D THM model to investigate the performance of geothermal reservoir with parallel fracture zones. It is found that a larger number of fracture zone leads to a higher heat production rate and longer lifespan of the geothermal reservoirs than that with lower number of fracture zone.

As for the selection of working fluid in EGS, besides the water, some other fluids such as supercritical (sc)CO₂ and (sc)N₂O have also attracted the attention of researchers [15]. Guo et al. [16] compared the performance of EGS using water and scCO₂ as working fluids. They present a 3D THM coupled model incorporating the discrete

fracture network model. Due to the low viscosity of scCO₂, the heat production efficiency is improved with the scCO₂ as the working fluid compared with water. A similar comparison was also made by Li et al. [17], where a 2D THM model with a discrete fracture network has been developed for the comparison of water with scCO₂. It was found that the scCO₂ as the working fluid can lead to a faster pressure change due to its physical properties. However, Cao et al.[12] found that with water as the working fluid, the heat production efficiency was higher. Borgia [18] proposed a two-phase flow dual-porosity continuum numerical model to simulate the fluid migration and phase displacement in EGS. When the geothermal reservoir was fully saturated with one phase (water or scCO₂), the heat production efficiency was obviously higher than when both fluid phases are present. Additionally, the efficiency was higher when scCO₂ became the only phase that fully saturated the reservoir. A novel working fluid, scN₂O, was proposed recently. Huang et al. [19] employed the scN₂O as the working fluid and developed a 3D TH model to study the performance of the reservoir using scN₂O in the application of geothermal energy in EGS. It was found that employing scN₂O in EGS had many advantages, such as the higher output and a longer service time of the EGS reservoir. Based on an open-source simulator and research code, DuMu^X [20], Glaeser et al. [21] investigated the migration of scCO₂ in two phase model with discrete fracture networks. Tatomir et al. [22], [23] developed a new method called Multiple Interacting Continua (MINC) Method for the two phase flow in discrete fracture model, which can effectively reduce the computational cost.

The structure of the geothermal reservoir is another vital factor for the simulation of fluid flow and heat transfer in EGS. Ma et al. [24] developed a 2D TH model with a leaf-like bifurcated fracture network to study the effect of the structure and properties of fracture networks on the heat extraction performance in EGS. Pandey et al [25] studied the influence of fracture alteration on the heat production through the single fracture THM model. A similar single fracture layer THM model was also proposed by Guo et al. [16]. They developed a 3D THM model with a 2D fracture layer to study the heterogeneity of the fractures on the heat production efficiency and the service life of

EGS. Huang et al. [26] developed an equivalent continuum 3D TH model considering the heterogeneous permeability and porosity. Li et al. [17] developed a 3D rough-walled discrete fracture model integrating the THM coupled processes to simulate the mass and heat transfer in a geothermal reservoir. They focus on the study of the influence of fracture roughness on the performance of EGS.

Although many studies have been conducted for the investigation of THM processes in EGS, only a few consider the effect of the variability of fracture apertures and related properties of the DFNs. This knowledge gap still needs to be addressed. In this paper, a coupled TH model with discrete fracture network is developed. Fracture networks with varying apertures are employed to investigate the influence of aperture distribution on heat production of the geothermal reservoirs. The discrete fracture network (DFN) is generated based on the properties of crystalline rocks to present the complexity of the natural underground structure of an EGS reservoir. The so-called partial raster-element concept and probability density function (PDF) are employed to describe the distribution of fracture apertures. Fracture density is applied to present the connectivity and conductivity of the generated DFNs. Different DFNs are generated to investigate the effect of DFN density and aperture distribution on the heat production performance in the EGS.

3.2. Thermo- hydraulic coupled numerical model

In the following part, a thermal- hydraulic coupled numerical model is presented for simulating the processes of the movement of fluid and transfer of heat in a fracture network. The following assumptions are made for the formulation of the mathematical model:

- (i) The simulated reservoir consists of the discrete fracture network (DFN) and surrounding rock matrix. The rock matrix is described by the continuum porous media. The physical properties of the rock matrix are uniform and isotropic.
- (ii) The fractures are represented as lower-dimensional entities, i.e., the rock matrix is 2D while the DFN is 1D. Fracture aperture varies between different fractures but it is

constant within an individual sub- fracture.

(iii) The fractured porous EGS reservoir is fully saturated with the working fluid (in our case water) before the simulation starts.

(iv) The working fluid is water, and the water in the reservoir does not vaporize and can be considered as liquid during the whole simulation.

(v) The heat transfer between the discrete fracture network and rock matrix is achieved by the processes of heat convection and conduction.

(vi) The small displacement caused by the variations of pore pressure and temperature is ignored, and the permeability and porosity are kept constant during the simulation both in the fracture and matrix domains.

(vii) The fractures are already created or re-opened before the simulation starts and no new fractures are created during the simulation.

3.2.1. Governing equations

Based on the aforementioned assumptions, the governing equations for the fractured porous geothermal system can be concluded as following.

The fluid flow in the rock matrix can be described by the mass conservation equation:

$$\frac{\partial(\rho_w \phi_m)}{\partial t} + \nabla \cdot (\rho_w \mathbf{v}_m) + Q_m = 0 \quad (1)$$

where ρ_w is the density of water, ϕ_m is the porosity of rock matrix, t is the simulation time, Q_m is the source and sink in the rock matrix and v_m is the flow velocity in the rock matrix. According to the assumption, the movement of the fluid can be described by Darcy's law:

$$\mathbf{v}_m = -\bar{\mathbf{K}}_m \frac{1}{\mu_w} \nabla \cdot (p_w + \rho_w \mathbf{g}) \quad (2)$$

where $\bar{\mathbf{K}}_m$ is the intrinsic permeability tensor of rock matrix which is assumed to be isotropic in this work, μ_w is the water viscosity, p_w is the pore pressure and the \mathbf{g} is the gravitational acceleration.

The governing equation for the flow in the DFN is different than that of the rock matrix, and can be described as follows:

$$d_f \frac{\partial(\rho_w \phi_f)}{\partial t} + \nabla \cdot (\rho_w \mathbf{v}_f d_f) + Q_f = 0 \quad (3)$$

where ϕ_f is the porosity of the fracture, Q_f is the source or sink term in the fracture, \mathbf{v}_f is the flow velocity within the fractures, which can also be described by the Darcy's law:

$$\mathbf{v}_f = -\bar{\bar{\mathbf{K}}}_f \frac{1}{\mu_w} \nabla \cdot (p_w + \rho_w \mathbf{g}) \quad (4)$$

where the $\bar{\bar{\mathbf{K}}}_f$ is the intrinsic permeability of each fracture in the discrete fracture network which follows the cubic law as follows:

$$\bar{\bar{\mathbf{K}}}_f = \frac{(d_f)^2}{12f} \quad (5)$$

where d_f is the fracture aperture, f is the fracture roughness which is set to be 1 for all the fractures

In geothermal reservoirs, the transfer of heat through the DFN is achieved by heat convection while conduction is the main process for heat transfer between the DFN and the rock matrix. In this work, the theory of local thermal equilibrium is introduced, which assumes that in the unit computational element, the thermal properties of fluid, fracture, and rock matrix are the same and can be represented by the effective values. The effective heat capacity and thermal conductivity are the weighted average of the values from water and surrounding rocks respectively [27].

$$(\rho C_p)_{\text{eff}} = \phi(\rho_w C_{pw}) + (1 - \phi)(\rho_m C_{pm}) \quad (6)$$

$$\lambda_{\text{eff}} = \phi \lambda_w + (1 - \phi) \lambda_m \quad (7)$$

where ϕ is porosity, $(\rho C_p)_{\text{eff}}$ is the effective heat capacity, C_{pw} and C_{pm} are the heat capacity of water and surrounding rock respective, ρ_m is the rock density, λ_{eff} is the effective thermal conductivity, λ_w and λ_m are the thermal conductivities of water and surrounding rocks respectively. Based on the law of energy conservation the heat transfer in the rock matrix can be described as following:

$$(\rho C_p)_{\text{eff}} \frac{\partial T}{\partial t} + C_{pw} \mathbf{v}_m \nabla T - \nabla \cdot (\lambda_{\text{eff}} \nabla T) + q_{h,m} = 0 \quad (8)$$

where T is the temperature, $q_{h,m}$ is the source and sink of heat in the rock matrix. Similarly, the energy conservational equation for the DFN can be described as

following:

$$d_f(\rho C_p)_{\text{eff}} \frac{\partial T}{\partial t} + d_f C_{pw} \mathbf{v}_f \nabla T - \nabla \cdot (d_f \lambda_{\text{eff}} \nabla T) + q_{h,f} = 0 \quad (9)$$

During the migration of cold working fluid, the variation of temperature can cause the change of fluid properties, which are affecting the flow velocity and pore pressure. Inversely, the change on flow velocity and pore pressure can also influence the heat transfer process. Therefore, the relationships between the properties of working fluid and temperature are very important.

The physical properties of the working fluid, i.e., water, such as the density, ρ_w (kg/s), viscosity, μ_w (Pa · s), heat capacity, C_{pw} (J/kg/K), and thermal conductivity, λ_w (W/m/K), are the functions of temperature, T(K). Since the range of reservoir pressure is limited, i.e., 62.4 MPa to 64.8 MPa, the influence of pressure on water properties is ignored. The relations can be described as following [16]:

$$\rho_w = 838.5 + 1.4T - 3 \times 10^{-3}T^2 + 3.7 \times 10^{-7}T^3 \quad (10)$$

$$\begin{aligned} \mu_w = & 1.38 - 0.02T - 1.36 \times 10^{-4}T^2 - 4.66 \times 10^{-7}T^3 + 8.9 \times 10^{-10}T^4 \\ & + 9.08 \times 10^{-13}T^5 + 3.85 \times 10^{-16}T^6, T \in [273.15, 413.15] \end{aligned} \quad (11)$$

$$\mu_w = 0.004 - 2.1 \times 10^{-5}T - 3.9 \times 10^{-8}T^2 - 2.4 \times 10^{-11}T^3, T \in [413.15, 553.15] \quad (12)$$

$$C_{pw} = 12010 - 80T + 0.3T^2 - 5.4 \times 10^{-4}T^3 + 3.6 \times 10^{-7}T^4 \quad (13)$$

$$\lambda_w = -0.87 + 0.009T - 1.6 \times 10^{-5}T^2 + 7.9 \times 10^{-9}T^3 \quad (14)$$

3.2.2. Model verification

The verification of the accuracy of the developed TH model is necessary before its further application. For this, the analytic solution proposed by Lauwerier et al. [28] and Barends et al. [29] is applied. This solution describes the temperature variation within a single fracture with a given aperture. As illustrated in **Figure 1**, the 2D fracture located in the middle of the domain is represented by a lower- dimensional (1D) fracture. The distance between the two fracture walls, i.e., fracture aperture, is $2d_f$. The thickness of the rock matrix is assumed to be infinite. The heat convection is ignored within the rock matrix. Water is injected into the fracture with a constant flow velocity \mathbf{v}_f and

temperature T_{in} from the left side. The analytic solution can be described as following:

$$T_f = T_0 + (T_{in} + T_0) \operatorname{erfc} \left(\frac{\lambda_m x / (\rho_w C_{pw} d_f)}{2 \sqrt{v_w (v_w t - x) \lambda_m / (\rho_m C_{pm})}} \right) U \left(t - \frac{x}{v_w} \right) \quad (15)$$

where T_0 is the initial temperature of the system, λ_m is the thermal conductivity of the matrix rocks, ρ_w , ρ_m , C_w and C_m are the density and heat capacities of water and matrix rock respectively, d_f is the fracture aperture, ‘erfc()’ is the complementary error function and ‘U()’ is the unit step function. The values of the parameters for the analytic solution and numerical simulation are presented in **Table 3.1**

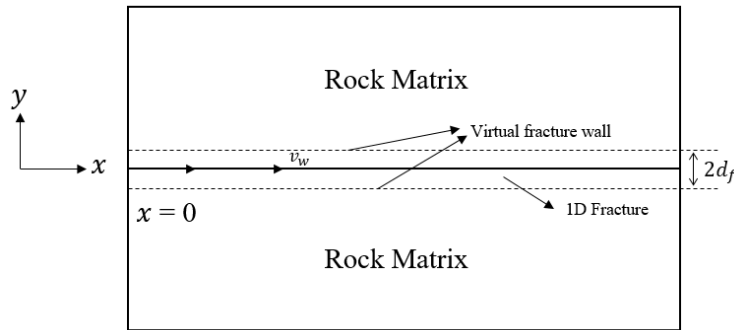


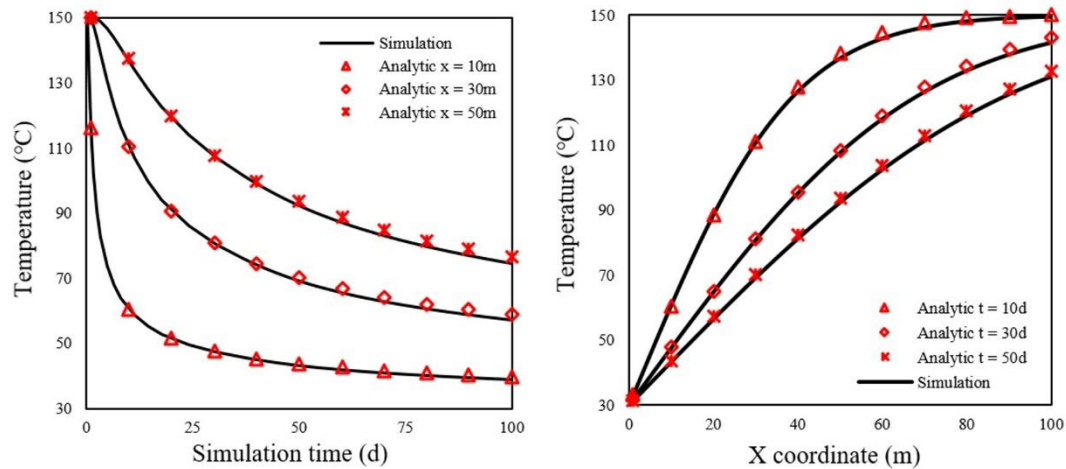
Figure 3.1. Geometrical representation of the lower-dimensional fracture model used for validation, with the position of the fracture walls forming the aperture, $2d_f$, in an equal-dimensional model

Table 3.1. Parameters for the single fracture TH model validation

Parameters	Value
T_0 (°C)	150
T_{in} (°CK)	30
λ_m (W/m/K)	3
ρ_w (kg/m ³)	1000
ρ_m (kg/m ³)	2700
d_f (mm)	0.1

C_f	(J/kg/K)	4200
C_s	(J/kg/K)	1000
v_w	(m/s)	0.001

The comparisons between the numerical model and the analytical solution are presented in **Figure 3.2**. **Figure 3.2(a)** illustrates the temperature variation over injection time at different positions within the fracture ($x = 10\text{m}$, 30m and 50m). Temperature distribution at different times ($t = 10\text{d}$, 30d , and 50d) is illustrated in **Figure 3.2(b)**. The good agreement between the analytical solution and numerical simulation results is an indication that the numerical model is accurate. The small discrepancies may result from the assumptions that the infinite thickness and length of the geometry in the analytic solution while the geometry of simulated domain is $100\text{m} \times 10\text{m}$ (Length \times thickness).



(a) Temperature evolution over time (b) Temperature distribution at different potions

Figure 3.2. Comparison between the analytical solution and the numerical simulation

3.3. Generation of discrete fracture networks

3.3.1. Fracture configuration

The performances of geothermal reservoirs are highly related to the properties of DFNs

due to higher permeabilities. Thus, the generation of DFNs is very important and the generated DFNs should represent the natural geological structures as well as possible. Generally, the EGS are applied in crystalline rocks. We conducted a literature review of the DFN parameters of crystalline rocks, summarizing works performed over several decades [30]–[32]. For example, the fracture orientations can be well presented by approximately 10° and 80°[33], and the fracture trace length can be described by the distributions of exponential, log-normal, and power-law [34]. In this work, the power-law distribution is employed for the fracture trace lengths.

$$f(x) = \frac{a-1}{x_{min}} \left(\frac{x_{min}}{x}\right)^a \quad (16)$$

where x is fracture length, x_{min} is the lowest fracture length, a is the power law exponent, which usually ranges between 1.5 and 3.5, in this work, $a = 2$ is selected.

3.3.2. Methodology

In this section, the generation of DFNs is presented. The left and right boundaries are set to be the injection and production boundaries while the top and bottom boundaries are closed for fluid flow. The detailed steps are summarized in **Figure 3.3(a)** to **(d)**. **Figure 3.3(a)** illustrates the original generated fracture network. Altogether 165 fractures are generated. In **Figure 3.3(b)**, the fractures presented in red are isolated fractures. They are not connected with the left hand-side (i.e., injection) or right (i.e., abstraction) boundaries and are not contributing to the fluid flow and heat transfer. Similarly, the fractures represented with red lines in **Figure 3.3(c)** are connected only to one boundary, resulting in the dead ends for the flow pathways, in which the heat cannot be effectively transferred. Thus, these kinds of fractures can be eliminated, as they do not influence the result. **Figure 3.3(d)** shows the final generated DFN, the fractures left are called backbone fractures, which form the main flow pathway for the transportation of the working fluid and heat. The fracture density is calculated based on the generated backbone DFNs. In this work, the fracture density (ρ_{21}) is defined as the ratio of the total fracture length to the domain area [35].

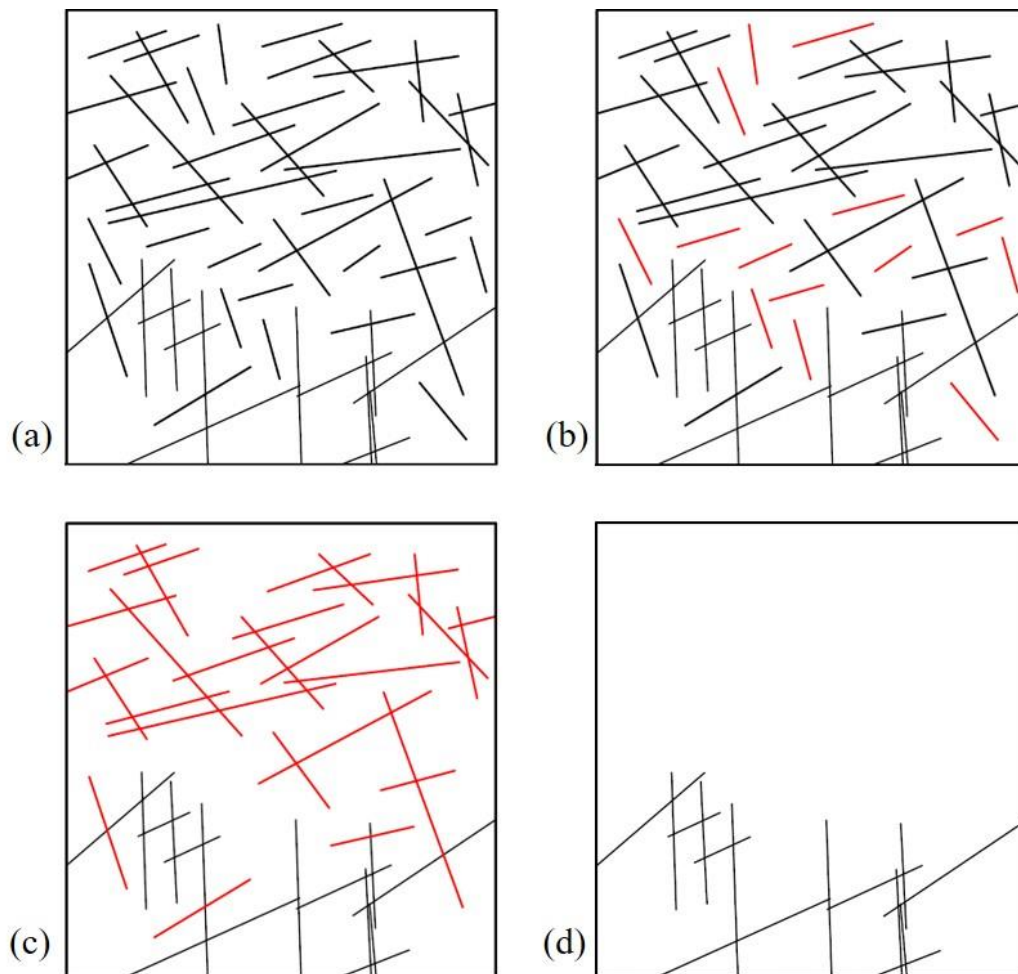


Figure 3.3. Generation of discrete fracture networks followed by the simplification for obtaining the one used in numerical simulations. (a) the initial generated DFN; (b) eliminating the isolated fractures (red lines), (c) eliminating the fractures with dead ends (red lines); (d) remaining backbone fracture network.

Fracture aperture is another important factor that needs to be addressed. Generally, the conceptual models for the fracture aperture are divided into two categories: 1) the parallel plate concept; 2) raster- element concept, as presented in **Figure 3.4**. The limitation of the parallel plate concept is that it cannot take into account the preferential flow path caused by fracture roughness, while the raster- element concept is restricted by the computational capacity [36]. In this work, we use an approach in between. For example, as presented in **Figure 3.5**, three fractures are mutually intersected and form a simple fracture network, generating 9 sub- fractures altogether, of which the apertures

for each sub- fracture are independent and can be different.

Several researches have demonstrated that fracture apertures are typically followed by the normal distribution or gamma distribution in a given stress field [37]–[39]. In this study, the normal distribution is selected to describe the aperture distribution of sub-fractures.

$$N(d_f) = \frac{1}{\sigma\sqrt{2\pi}} e^{-\frac{1}{2}\left(\frac{d_f-\mu}{\sigma}\right)^2} \quad (17)$$

where d_f presents the fracture aperture, $N(d_f)$ is the probability density of the sub-fracture with the aperture of d_f , μ and σ are the mean and standard deviation of the DFNs apertures, respectively. The term “coefficient of variation (σ_r)” is introduced and defined as the ratio of standard deviation (σ) to mean aperture (μ) as presented following.

$$\sigma_r = \frac{\sigma}{\mu} \quad (18)$$

The coefficient of variation combines the two variables for normal distribution and avoids the error from the application of single σ . For example, provided that the $\sigma = 0.1$, for the $\mu = 0.3$ and 0.7 , the degrees of coefficient of variation of fracture apertures are not identical.

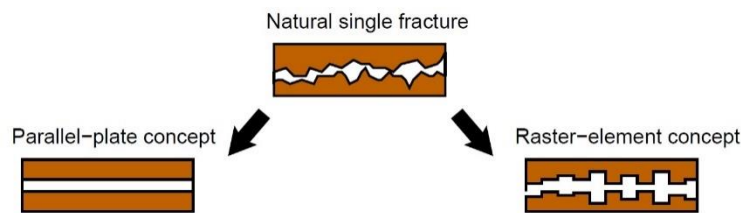


Figure 3.4. Model concepts for a fracture aperture [36].

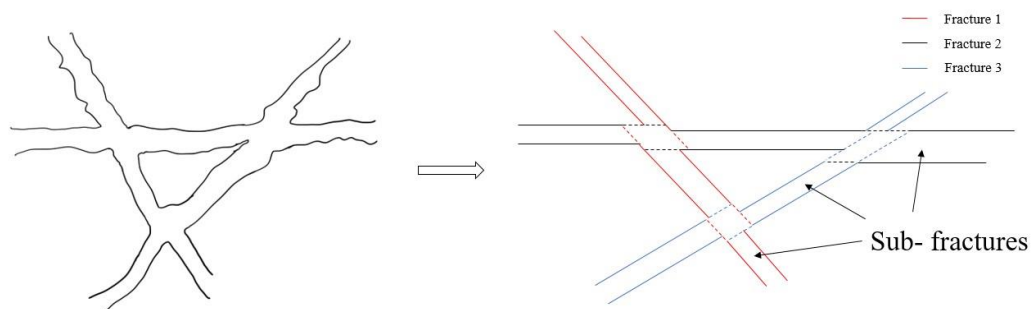


Figure 3.5. Schematic representation of the partial raster- element concept, from natural to modelling.

3.4. Numerical model

3.4.1. Modelling strategy

The main objective of this work is to investigate the influence of the properties of backbone DFNs on the performance of geothermal reservoirs. The key properties of the backbone DFN are the fracture density and fracture aperture distribution, and of the reservoir performance are the outlet temperature and average heat production rate over the production period. The influences from aperture distribution are studied by comparing the simulation results with different coefficient of variations and mean apertures (the zero- coefficient of variation presents that all fractures have the same aperture). Then the effects from the fracture density are investigated based on the various fracture density among the six scenarios. Finally, the roles of aperture distribution and fracture density on the performance of geothermal reservoirs are compared, and the suggestions for improving the average heat production rate are provided.

3.4.2. Monte-Carlo method

In this paper, six scenarios with different backbone DFNs are generated (**Figure 3.6** and **Table 3.2**). For each scenario, twenty-five different combinations of average fracture aperture and coefficient of variation are applied. Within every combination, the fracture apertures are randomly distributed, forming different realizations, of which the statistic properties (mean fracture aperture and coefficient of variation) are the same. Monte- Carlo method is applied such that for each combination, a large number of realizations is simulated to assure that the simulation results reach to a statistical equilibrium.

3.4.3. Model description

The simulation model is implemented with the commercial software COMSOL

Multiphysics and based on finite element method. In this work, the two-dimensional (2D) simulated area is 1000m × 200m. The depth of the simulated reservoir is assumed to be located from 6400m to 6600m underground. Three sets of fracture configurations are employed to generate the discrete fracture networks (DFN). The properties of the DFN are referenced from the previous publications [29]- [33] and the detailed values are presented in **Table 3.2**.

The generation of backbone DFN is based on the methodology given above and properties representative of crystalline rocks. The simulated fracture density ranges between 0.0121 m/m² and 0.054 m/m². The detailed parameters and fracture densities are summarized in **Table 3.2**.

Table 3.2. Parameters of fracture network generation

Scenarios	1	2	3	4	5	6
Fracture densities	0.0223	0.0392	0.054	0.0121	0.032	0.0256
DFNs	Set1		Set2		Set3	
Dip angle (°) ^{[29] [30]}	10		75		80	
Fracture trace length	Power- law distribution (a = 2)					
Min (m) ^{[31] - [33]}	100		40		60	
Max (m) ^{[31] - [33]}	528		100		300	
Fracture number	100		50		25	

The initial pressure distribution in the system results from a hydrostatic pressure gradient (9.81MPa/km) and an atmospheric pressure of 0.1 MPa at the surface. This results in the pressure of 62.9 MPa at top of the domain. A static temperature distribution linearly increasing from 200 °C at the top boundary with a thermal gradient of 18 °C/km is assigned [40].

Water is injected into the reservoir from the left boundary with the temperature of 20 °C and is abstracted from the right boundary. The given pressure on the top of the left boundary of the domain is set to 64.4 MPa and the pressure on the top of the right

boundary of the domain is 62.4 MPa [17]. The total simulation period is 30 years. The fundamental parameters for the models come from Li et al. [17] and are summarized in **Table 3.3**.

Table 3.3. Parameters for the simulations

Parameters	value
Density of rocks (kg/m ³)	2700
Density of water (kg/m ³)	Eq. 10
Viscosity of water (Pa·s)	Eq. 11-12
Porosity of fractures (-)	0.2
Porosity of rock matrix (-)	0.01
Permeability of rock matrix (m ²)	1×10^{-18}
Permeability of fractures (m ²)	Eq. 5
Thermal conductivity of rocks (W/m/K)	2
Thermal conductivity of water (W/m/K)	Eq. 14
Heat capacity of rocks (J/kg/K)	2000
Heat capacity of water (J/kg/K)	Eq. 13

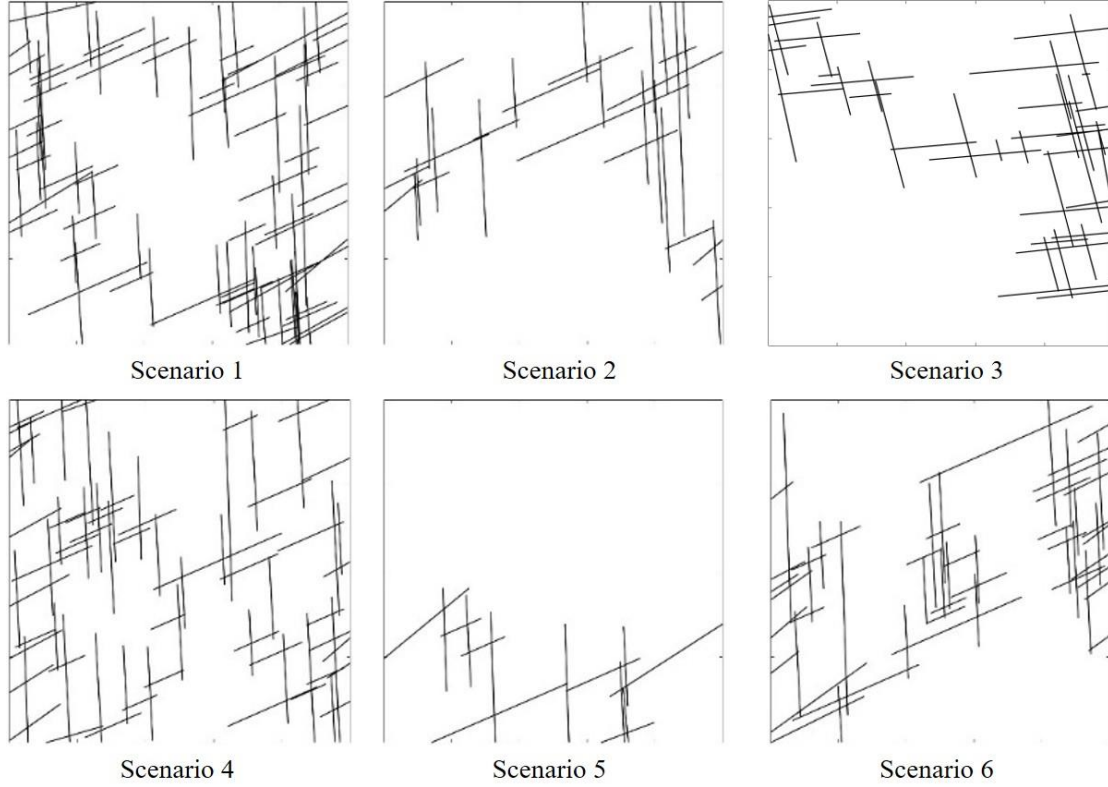


Figure 3.6. Simulated geometries of the six backbone DFNs (1000m in length × 200m in height).

3.4.4. Definition of characteristic parameters

Some key performance indicators are introduced for the assessment of the effect of the aperture distribution on the performance of heat production in the geothermal reservoir:

(i) Outlet temperature (T_o) is the production temperature at production well, which is the average temperature of fractures and rock matrix [9] [10] [17]:

$$T_o = \frac{\sum \mathbf{u}_f d_f T_f + \int \mathbf{q}_m T_m dy}{\sum \mathbf{u}_f d_f + \int \mathbf{q}_m dy} \quad (19)$$

where d_f is the fracture aperture, \mathbf{u}_f , \mathbf{q}_m , T_f , and T_m are the flux from fracture, flux from matrix, fracture temperature and matrix temperature at production boundary, respectively.

(ii) Variation of the average final outlet temperature (V_T) is the difference between the outlet temperature at the beginning and the end of the production period:

$$V_T = \frac{T_{fo} - T_{bo}}{T_{bo}} \times 100\% \quad (19)$$

where V_T is the temperature variation, T_{fo} and T_{bo} are the average outlet temperature at the end and beginning of the production period.

(iii) Heat production rate (P):

$$P(t) = \int_0^L \rho_w C_w \mathbf{v}_w (T_{out} - T_{in}) L_z dl \quad (20)$$

where L is the length of the abstraction boundary, T_{out} is the outlet temperature, L_z is the effective thickness of the domain, which is equal to 1m.

(iv) Average heat production rate (A_r) is the average of the heat production rate over the whole production period:

$$A_r = \frac{1}{t_{end}} \int_0^{t_{end}} P(t) dt \quad (21)$$

where t_{end} is the production time.

3.5. Results analysis

3.5.1. Effects of the number of realizations

Due to the low fracture density of backbone DFN, the results of Monte Carlo method can vary greatly. Thus, it is necessary to investigate the result variations for all the scenarios. **Figure 3.7** presents the relationships between average heat production rates and the number of realizations for the six scenarios. In this case, the average aperture is 0.7mm while the coefficient of variation is 1. It is observed that for all the six scenarios, the average heat production rates are stabilizing at a constant level with the increase of the realization numbers. Fifty realizations are sufficient to reach the statistical convergence. Furthermore, as with the decrease of the coefficient of variation, the convergence takes place at fewer number of realizations, fifty realizations were deemed to be sufficient even for the cases of lower coefficient of variation values (i.e., $\sigma_r < 1$) Based on this, for each mean aperture – coefficient of variation combination fifty, realizations were simulated. In total, altogether 7500 realizations were run for the six backbone DFNs, for the altogether twenty-five parameter combinations (**Table 3.4**), with fifty realizations for each combination.

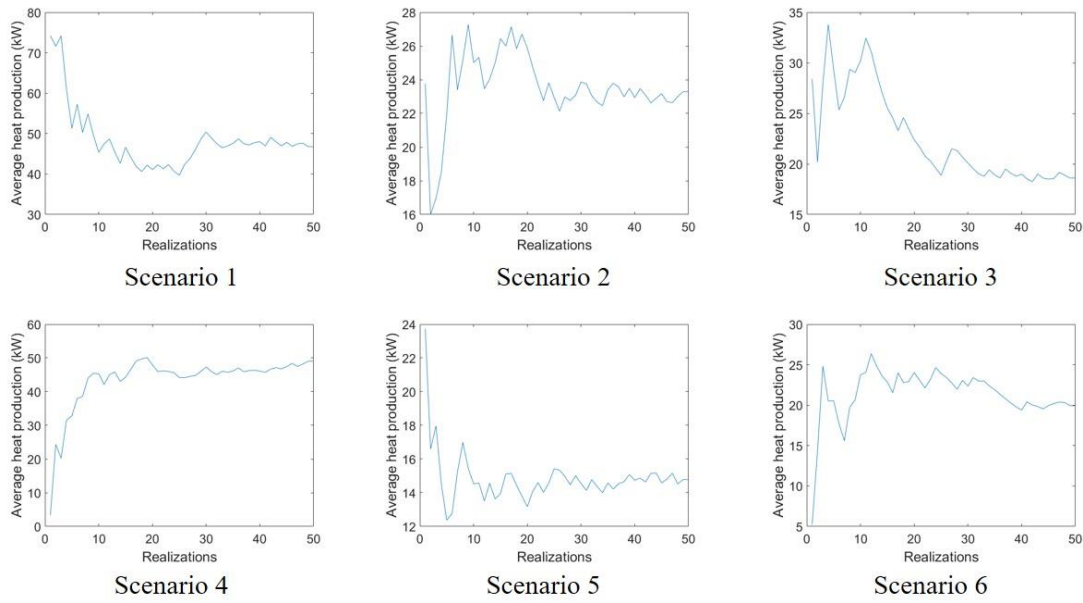


Figure 3.7. Simulated average heat production rates as a function of the number of realizations for all six scenarios (mean aperture of 0.7mm and coefficient of variation of 1).

In the following sections, the results present the performance of the geothermal reservoirs using different geometries of the generated backbone DFNs. Please note the word “backbone” is going to be omitted from here onwards. The investigation on the effect of the coefficient of variation are illustrated firstly. Then, the influences from fracture density are displayed. Finally, the roles of fracture properties on EGS performance are analyzed.

Table 3.4. Combinations of mean aperture and coefficient of variations

Mean aperture (mm)	Coefficient of variations
0.3	0.33, 0.67, 1
0.4	0.25, 0.5, 0.75, 1
0.5	0.2, 0.4, 0.6, 0.8, 1
0.6	0.167, 0.33, 0.5, 0.67, 0.83, 1
0.7	0.14, 0.28, 0.43, 0.57, 0.71, 0.86, 1

3.5.2. Effects of coefficient of variation

This section investigates the influences of the coefficient of variation on the outlet temperature and average heat production rate. **Figure 3.8** and **3.9** give the examples of the distributions of the over- pressure (i.e., the difference between pore pressure and initial pressure) and temperature for different coefficient of variations ($\sigma_r = 0, 0.2,$ and 0.6) at 5th and 30th years.

Due to the higher permeability and lower storage of the fractures, the pressure distribution has a strong correlation with the coefficient of variation. As presented in **Figure 3.8**, the variation of pore pressure is mainly reflected within the DFN at the 5th year, the over – pressure generally decreases from left boundary to right boundary. Then, the pore pressures generally penetrate into the rock matrix with the production processing. The over- pressure distributions with $\sigma_r = 0,$ and 0.2 are very similar. However, with the growth of the $\sigma_r,$ the discrepancy appears. For example, the pressure gradients become more significant at the case with σ_r equals to $0.6,$ compared with case with σ_r equals to 0 and $0.2.$

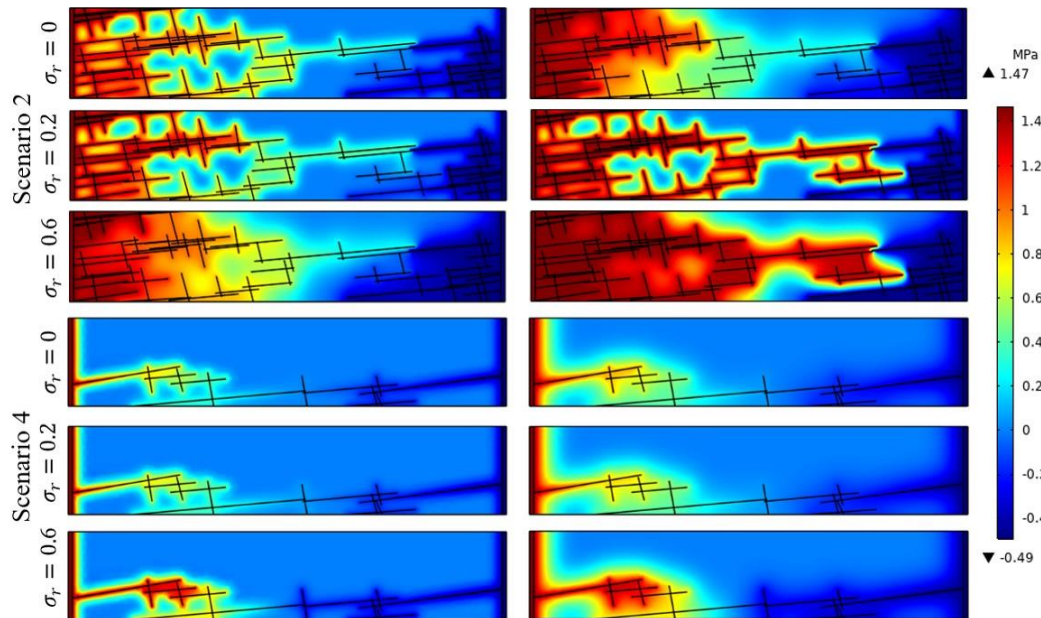


Figure 3.8. Pore pressure distributions with $\sigma_r = 0, 0.2,$ and 0.6 at 5th and 30th years.

Figure 3.9 presents the corresponding temperature distribution for $\sigma_r = 0, 0.2,$ and 0.6

at 5th year and 30th year. It is observed that the DFN forms the main flow path of the thermal fluid due to its higher permeability. The heat propagation pathways for the different values of σ_r are similar, but the heat propagation efficiency is strongly affected by the coefficient of variation. With the increase of coefficient of variation, the heat transfer efficiencies are reduced.

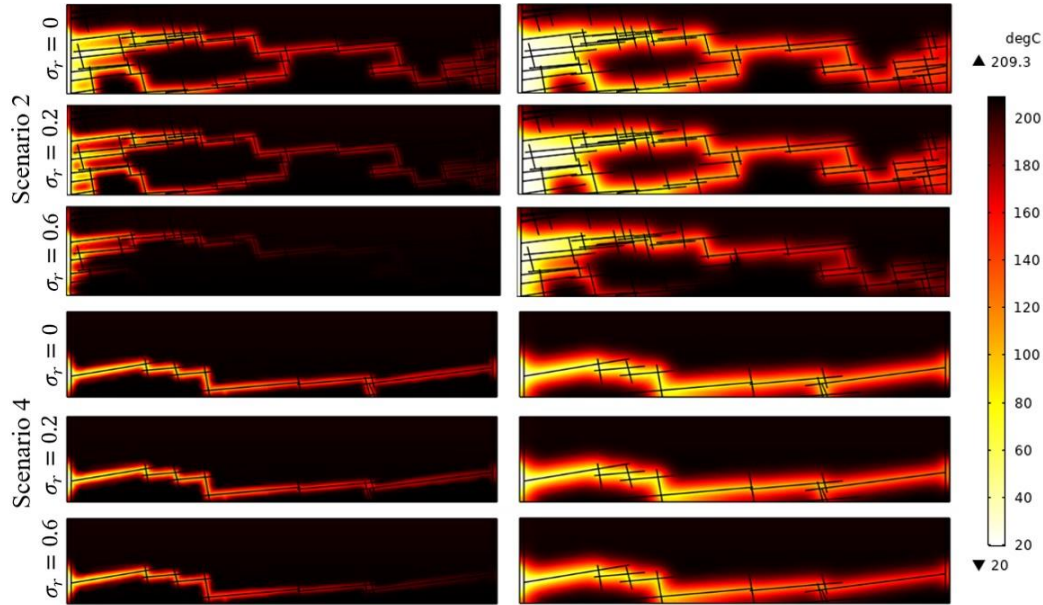


Figure 3.9. Temperature distributions with $\sigma_r = 0, 0.2, 0.6,$ and 1 at 5th and 30th years.

Next, comparisons of the outlet temperature, production flow rate, average heat extraction rate, and the cumulative energy generation are illustrated for scenario 4, the average aperture of 0.5 mm and the coefficient of variation ranges between 0 to 1.

Figure 3.10 presents the variation of (a) the outlet temperature and (b) the production flow rate plotted over the production time for different coefficient of variations (0.2, 0.4, and 0.8). The solid lines are the mean values from Monte Carlo method, while the colored areas present the standard deviation of the realizations ($\sigma_c = \mu \pm \sigma$). It is observed that the T_{f0} s remain constant before the breakthrough arrives. After the breakthrough, the temperatures have a nearly linear reduction until the end of the simulations. The discrepancies over the coefficient of variation are apparent. The outlet temperature decreases with the growth of the coefficient of variation, which results

from that the flow rate over the system is affected by the variation of fracture aperture, impeding the movement of cold fluid. On the other hand, the colored areas become wider as the coefficient of variation increases, indicating the variation of production temperature increases with the enlargement of coefficient of variation. Besides, the case of $\sigma_r = 0.2$ has a very small colored area, which confirms the system with low variation coefficient (σ_r) of fracture aperture has the similar performance with the homogeneous system.

As presented in **Figure 3.10(b)**, the reduction of production flow rate over production time results from the propagation of the front of cold working fluid. The lower temperature increases the flow resistance (e.g., viscosity), and decrease the flow rate. A similar result has been obtained by Gong et al., (2020). On the other hand, the production flow rate is reduced with the increase of the coefficient of variation, which further proves the reduction on production temperature results from the decrease of the flow rate. The colored areas are consistent with the observations in **Figure 3.10(a)**, and are not discussed further.

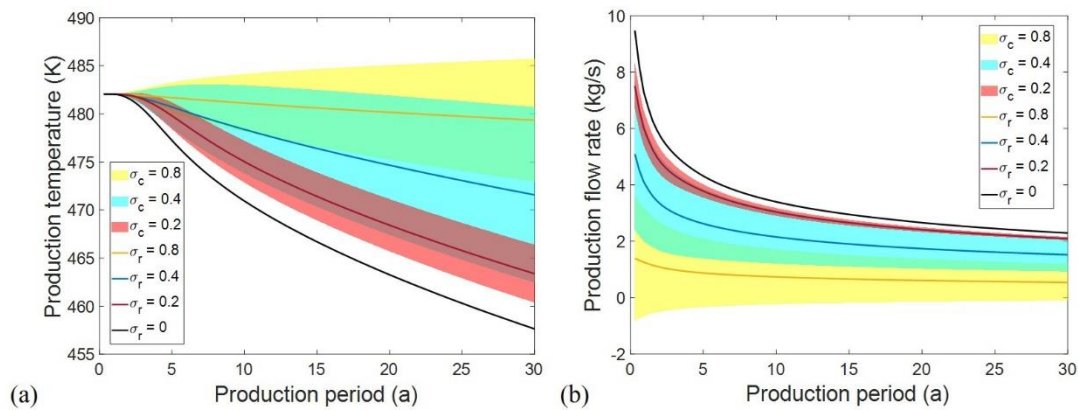


Figure 3.10. the variation of (a) the outlet temperature and (b) the production flow rate over the production time with different coefficient of variations of aperture distributions. Solid lines: the average results of the realizations; colored area, the standard deviation of the realizations.

Figure 3.11 presents the variation of (a) the heat production rates and (b) the cumulative

energy production over the production time for different coefficients of variations. It is observed that the overall tendencies of the heat production rate are similar for all values of coefficient of variations, i.e., the reduction of heat production rate generally becomes slower as the production proceed. Additionally, the curves of heat production rate are similar with those of production flow rate, indicating the production flow rate dominates the heat production rate (i.e., the variations of fluid density and heat capacity can be negligible). Furthermore, there is a reduction in heat production rates with the growth of coefficient of variation. The lower flow rate caused by the higher coefficient of variation is the reason for the phenomenon.

The cumulative produced energy in EGS are significantly affected by the coefficient of variations of aperture distribution. As presented in **Figure 3.11(b)**, the total produced energy from the system with $\sigma_r = 0.8$ is approximately 200 kJ, while the value from the system with $\sigma_r = 0$ is three times larger, reaching 800 kJ at the end of the production period (30th year).

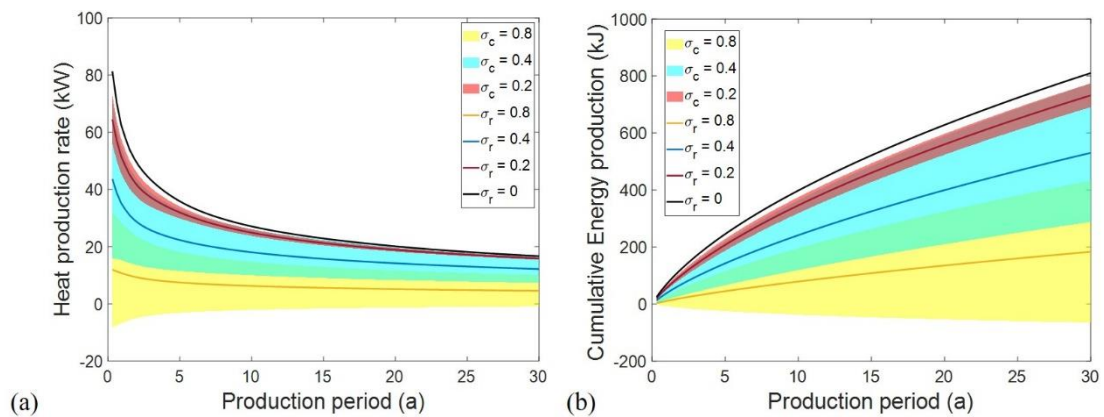


Figure 3.11. the variation of (a) the heat production rates and (b) the cumulative energy production over the production time with different coefficient of variations of aperture distributions. Solid lines: the average results of the realizations; colored area, the standard deviation of the realizations.

Figure 3.12 shows the variation of the average of (a) heat production rate (A_r) and (b) outlet temperature (V_T) at the end of simulation of fifty realizations over the coefficient of variation. The blue hollow circles present the results from the Monte Carlo

realizations. There are apparently more results below the result of the homogeneous system than above it for both the A_r and V_T , which indicates that the aperture distribution of DFN tends to impede flow channeling and reduce the heat production rate as well as the change of outlet temperature. Occasionally, the system with distributed fracture aperture performs better than the homogeneous system. In this case, the low apertures mainly located at the branch fractures while the apertures of the main flow pathway are high, resulting in a more considerable flow rate, then the larger A_r and V_T . Furthermore, with the growth of the coefficient of variation, the average A_r of Monte Carlo realizations firstly has a slight reduction which is followed by a sharp decrease; finally, the value tends to be stable, keeping at a nearly constant level.

The V_T for the six cases are presented in **Figure 3.12(b)**. It is observed that the V_T has the similar tendency as the A_r . It is observed that average V_T has a sharp reduction with low coefficient of variation, while when the coefficient of variation is considerable, the value varies at a limited range.

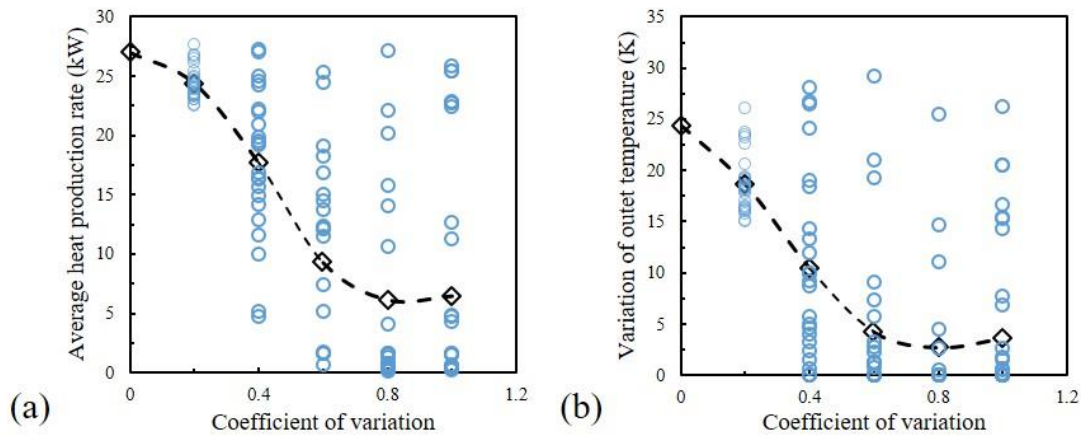


Figure 3.12. (a) Average heat production rate A_r and (b) the variation of outlet temperature V_T at the end of simulation period as function of the coefficient of variation. Black points and line: the average of fifty realizations, blue points: the results of the realizations.

Figure 3.13 presents the average heat production rate (A_r) over coefficient of variation for the 25 combinations of the mean value (μ) and coefficient of variation (σ_r) for each

scenario with Monte Carlo method. Only the results from RG1, RG2, and RG3 are presented; the results for the other geometries are presented in the appendix. The μ ranges between 0.3 mm and 0.7 mm and σ_r ranges from 0 to 1. The S- shape relationship between A_r and σ_r is observed for all the scenarios. With the increase of σ_r , A_r firstly enters the lower σ_r stage at the range of $\sigma_r < 0.3$, in which there is a slight reduction in A_r . Then the A_r comes to the middle σ_r stage when the σ_r ranges between approximately 0.3 to 0.6, where the A_r has a considerable decrease. Finally, the A_r keeps at a nearly constant level when σ_r is larger than approximately 0.6 (i.e., high σ_r stage). The existence of the three σ_r stages in the three scenarios indicates that, the relationships between A_r and σ_r are independent of the geometries with different DFNs.

Additionally, if the average heat production rate (A_r) at the three stages are compared, it is obtained that the A_r have solid linear relationships with the mean apertures at all three σ_r stages, as presented in **Figure 3.13**. With the increase of coefficient of variation, the slopes of $A_r - \mu$ curves have a slight reduction, indicating the growths of A_r through the enlargement of mean aperture generally decrease with the increase of coefficient of variation.

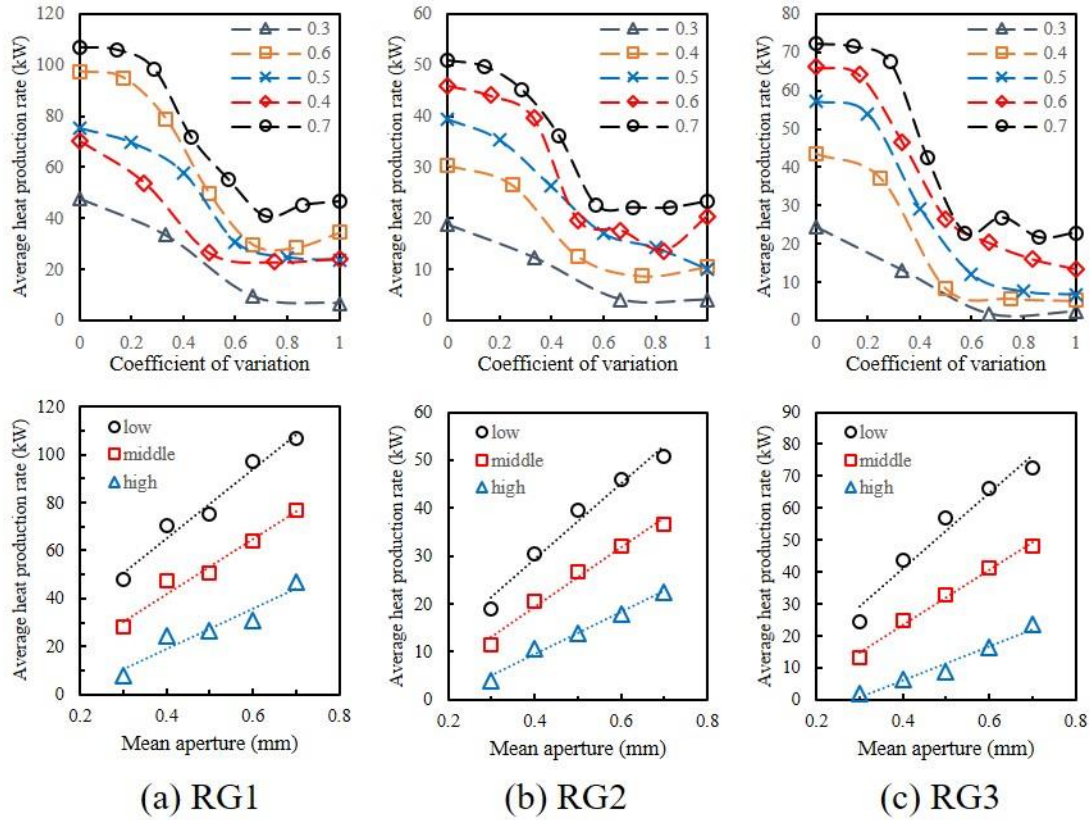


Figure 3.13. The relationships between the average heat production rate and coefficient of variation for different mean apertures (upper panels) and the relationship between the average heat production rate and mean aperture for different networks (lower panels) at different stage of coefficient of variation (low: $\sigma_r < 0.3$, middle: $0.3 < \sigma_r < 0.6$, and high: $\sigma_r > 0.6$), (a) RG1, (b) RG2, (c) RG3.

The effects of coefficient of variation on the variation of outlet temperature at 30th year (V_T) for scenarios 1, 2, and 3 are presented in **Figure 3.14**. The S- shape relationships between V_T and coefficient of variation are observed for all the mean apertures ranged between 0.3 and 0.7 mm. Unlike A_r , the ranges of low σ_r stages for V_T are very limited (approximately ranged from 0 to 0.2), indicating the outlet temperatures are more likely to be affected by the low value of coefficient of variation. **Figure 3.14** also presents the V_T over mean fracture apertures at different σ_r stages for scenario 1, 2, and 3. It is obtained that the V_T s have solid linear relationships with the average fracture

aperture (μ) at all three σ_r stages. On the other hand, the slopes of the $V_T - \mu$ curves decrease with the growth of coefficient of variation, indicating the enlargement of average aperture has smaller effects on the outlet temperature in the reservoirs with high coefficient of variation compared with the lower one.

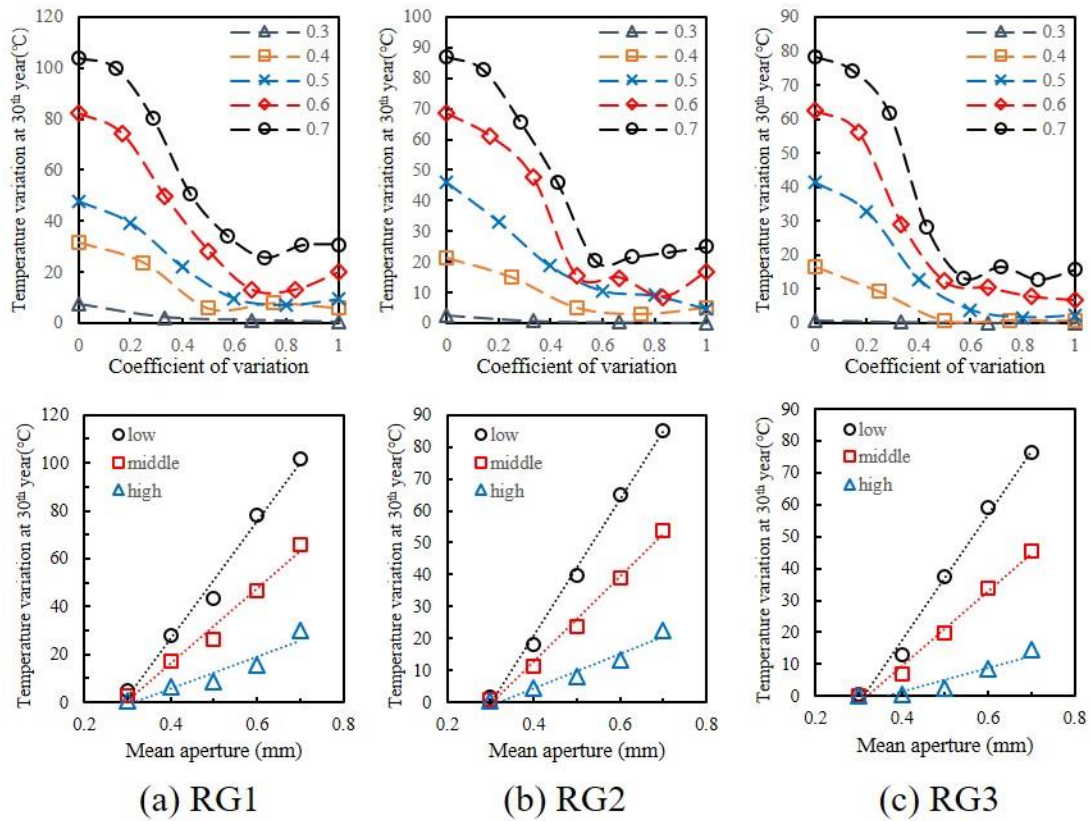


Figure 3.14. The relationships between the variation of outlet temperature and coefficient of variation for different mean apertures (upper panels) and the relationship between the variation of outlet temperature and mean aperture for different networks (lower panels) at different stage of coefficient of variation (low: $\sigma_r < 0.2$, middle: $0.2 < \sigma_r < 0.6$, and high: $\sigma_r > 0.6$), (a) RG1, (b) RG2, (c) RG3.

3.5.3. Effect of fracture density

In this section, the effects of fracture densities (ρ_{21}) on the average heat production rate (A_r) are presented and investigated. **Figure 3.15** presents the A_r over ρ_{21} with

different mean apertures at the three σ_r stages. It is observed that for all the mean apertures, the A_r has solid linear relationships with fracture density at the low and middle coefficient of variation stages with the correlation coefficients $R^2 = 0.9726$ and $R^2 = 0.9512$, respectively. However, for the high coefficient of variation, the linear correlation between A_r and ρ_{21} is comparably weak; the average correlation coefficient is only 0.7197. This is because higher coefficient of variation leads to more considerable complexity and randomness of the geothermal systems, resulting in the more enormous discrepancies. The slope of $A_r - \rho_{21}$ curve increases with the enlargement of mean aperture for all the three σ_r stages, which means the influence from ρ_{21} is more considerable at the larger mean aperture. At the low σ_r stage, with the enlargement of ρ_{21} , the A_r with $\mu = 0.7$ increases by 72.09 kW, from 34.74 kW to 106.83 kW while the growth of A_r with $\mu = 0.3$ is only 35.14 kW, from 12.76 kW to 47.9 kW. For the middle σ_r stage, the increases from $\mu = 0.7$ and 0.3 are 51 kW and 20.53 kW, respectively.

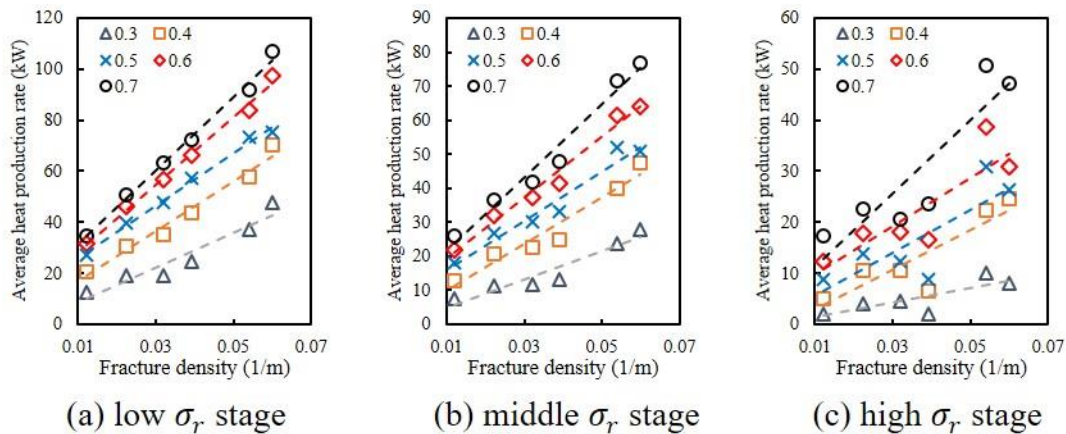


Figure 3.15. The relationships of average heat production rate with fracture density for different mean aperture at (a) low coefficient of variation stages, (b) middle coefficient of variation stage, and (c) high coefficient of variation stage.

Figure 3.16 presents the relationships between the A_r and ρ_{21} at three σ_r stages when $\mu = 0.3, 0.5, \text{ and } 0.7$, respectively. It is observed that the influences from ρ_{21} on A_r are more considerable at the low σ_r stage for all the mean apertures. The

slopes of the $A_r - \rho_{21}$ curves are 687.87, 1034.2, and 1437.4 respectively with $\mu = 0.3, 0.5,$ and 0.7 at low σ_r stage. On this other hand, the slopes are 141.67, 420.1, and 718.37 for the high σ_r stage. The discrepancy can be explained by the permeability of the new created fracture with the growth of fracture density. At the low σ_r stage, the apertures and permeability of the newly created fractures are very close to the pre-existing fractures. In contrast, at the high σ_r stage, the permeability of the newly created fracture is more likely lower than the mean-aperture fracture, considering the cubic law of fracture permeability.

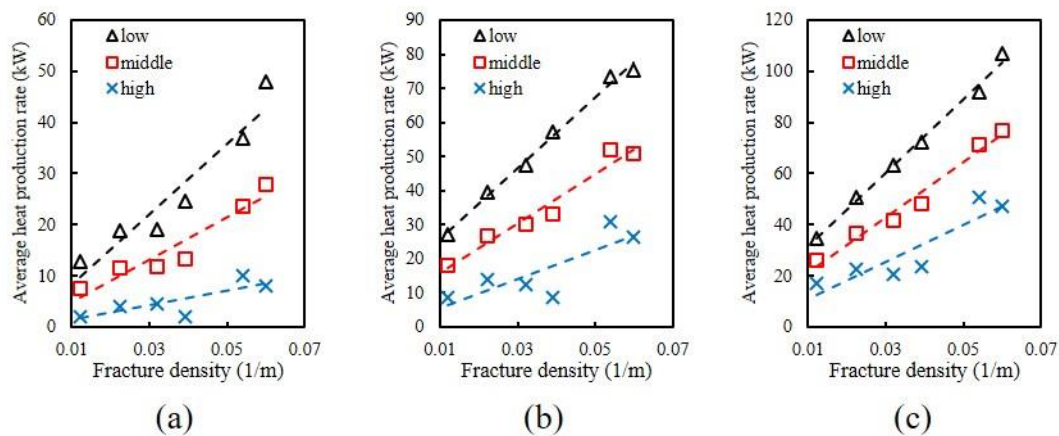


Figure 3.16. The relationships of average heat production rate with fracture density at three coefficient of variation stages when the mean aperture equals (a) 0.3 mm, (b) 0.5 mm, and (c) 0.7 mm.

3.5.4. Effects from fracture aperture and fracture density

The individual effects from the fracture aperture and fracture density on average heat production rates have been presented before. Next, the influences from the two parameters are combined and discussed in this section.

Since the ranges of fracture density and aperture coefficient of variation have a considerable discrepancy, i.e., 0.0121 1/m to 0.054 1/m for fracture density and 0.3 to 0.7 for coefficient of variation, in order to facilitate the comparison, the magnification method and a dimensionless parameter named magnification factor (f_m) are applied.

Based on the magnification method, a value of fracture aperture and fracture density are selected as the base value; then the magnification factors are calculated by the ratios of proposed values of fracture aperture and density to the base values. With the magnification factors, the comparison between fracture aperture and density becomes possible.

Figure 3.17 presents the comparison of the effects from fracture aperture and density on average heat production rates at low, middle, and high σ_r stages. RG4 is selected as the base geometry with the fracture density of 0.0121 1/m; thus the magnification factor for fracture density ranges from 1 to 4.96 (obtained by RG1, with the density of 0.06 1/m). On the other hand, the mean aperture of 0.3 mm is selected as the base value, leading to the range of magnification factor for fracture aperture is 1 to 2.33 (obtained by the average aperture of 0.7 mm). It is observed that at low and middle σ_r stages, the A_r have solid linear relationships with magnification factors. The slopes of the $A_r - f_m$ curves are 16.41 and 8.32 for fracture aperture and density at low σ_r stage, which means that provided that the magnification factors becomes double as the base value, A_r would increase approximately 16.41 kW from the aperture while the growth from fracture density is nearly 8.32 kW. On the other hand, the slopes of $A_r - f_m$ curves are 13.82 and 5.02 at the middle σ_r stage, and 11.23 and 1.71 at the high σ_r stage for fracture aperture and density, respectively. The higher slopes from fracture aperture indicate that the increase of fracture aperture is much more beneficial for the improvement of average heat production rate, especially at the high σ_r stage.

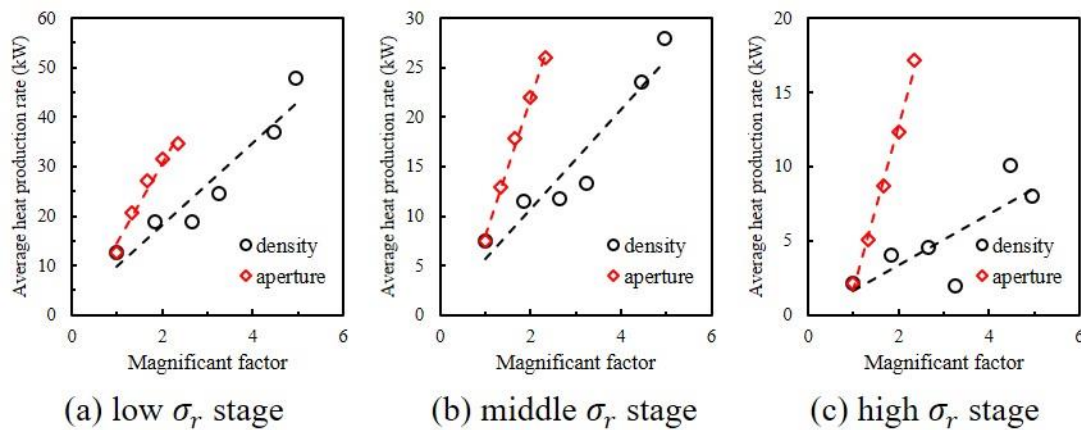


Figure 3.17. The relationships of average heat production rate with fracture density for different average aperture at three coefficient of variation stages.

3.6. Conclusion

In this study, a two-dimensional model for simulating thermal- hydraulic (TH) coupled processes in discrete fracture networks (DFN) is presented for studying fluid flow and heat transport in geothermal reservoirs. The discrete fracture model uses a lower-dimensional representation of the fracture elements. First, the proposed numerical model is validated by comparing the results with an analytical solution. The comparison indicates that the proposed model can well simulate the thermal- hydraulic processes in a lower-dimensional single horizontal fracture domain. The model is then applied to investigate the effects of the characteristics of the DFNs on the performance of geothermal reservoirs in EGS. The DFNs employed in this work are the backbone DFNs, from which the isolated fractures and the fractures with dead end are eliminated. The following conclusion can be obtained:

- (1) The coefficient of variation of fracture apertures plays a critical role in evaluating the performance of a geothermal reservoir. The performance can be divided into three stages depending on the coefficient of variation: at the low (lower than 0.2) and high (higher than 0.6) coefficient of variation stages, the average heat production rates keep at a nearly constant level, while at the middle coefficient of variation stage (between 0.2 and 0.6), the average heat production rates have a sharp reduction.
- (2) The increase of the average heat production rate with the average fracture aperture is highly related to the coefficient of variation. The high coefficient of variation inhibits the effects from average fracture aperture, resulting in the lower growth of average heat production rate compared with the low coefficient of variation.
- (3) The average heat production rate (A_r) has a linear relationship with the fracture density (ρ_{21}). Their relationship is proportional to the average fracture aperture: the higher average fracture aperture leads to a more considerable growth rate of the average heat production rate. Additionally, their relationship is also related to the coefficient of

variation. The slopes of $A_r - \rho_{21}$ curves are inversely proportional to the coefficient of variation.

(4) The increase of heat production rate of an existing geothermal reservoir with the discrete fracture network can be achieved by the enlargement of fracture density or aperture. Provided that the base value of aperture is 0.3 mm and of density is 0.0121 1/m, the performance from enlarging DFN aperture is obviously better than creating new fractures.

3.7. Appendix:

1. The data of average heat production and outlet temperature for RG(4), RG(5), and RG(6).

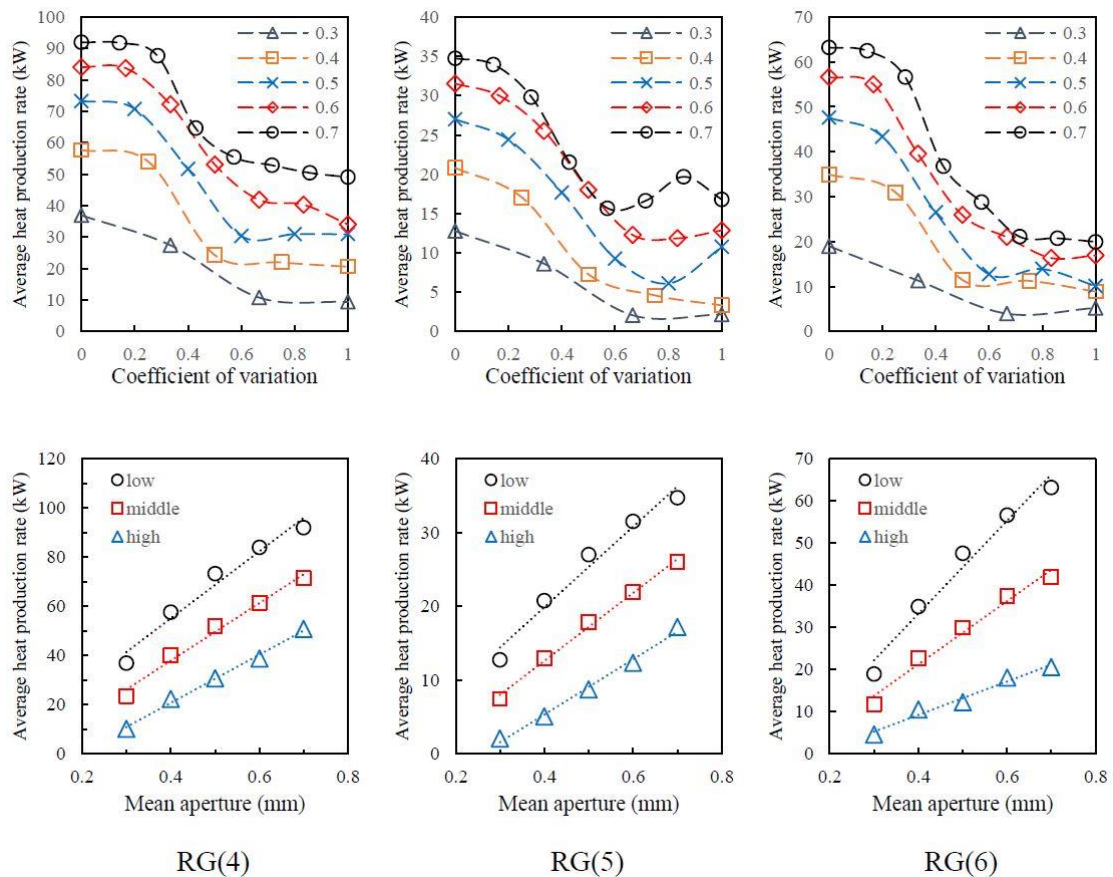


Figure 3.18. The relationships of average heat production rate with coefficient of variation and mean aperture for different discrete fracture networks, (a) RG4, (b)

RG5, (c) RG6.

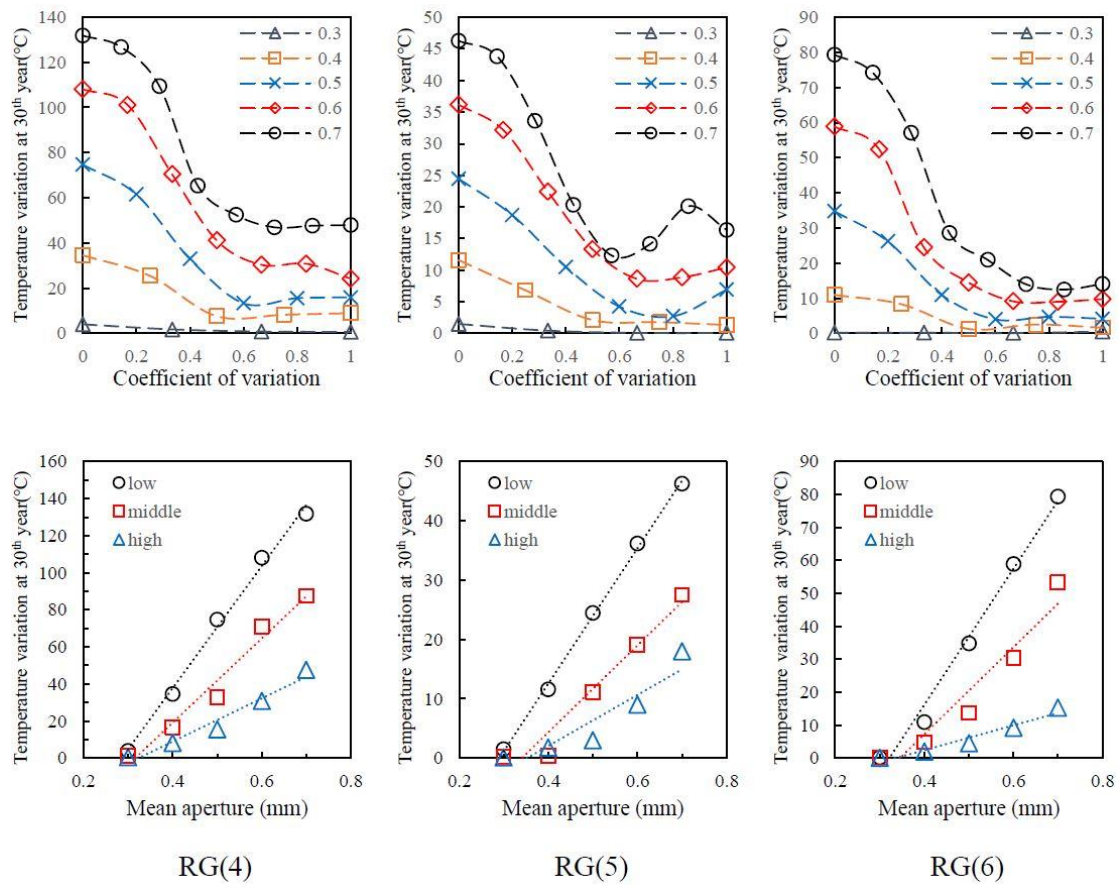


Figure 3.19. The relationships of the variation of outlet temperature with coefficient of variation and mean aperture for different discrete fracture networks, (a) RG4, (b) RG5, (c) RG6.

2. Model verification against another analytic solution proposed by Gringarten et al [41].

The analytic solution describes the heat extraction from multiple fractures in the hot rock system. As presented in **Figure 3.20**, the parallel fractures locate between the rock matrix. The cold water is injected from the bottom of the fractures, and abstract from the fracture top. It is assumed the thickness of the fracture is $2d_f$ and the spacing between the fractures is 160m. The domain height and width are set to be 1km, and the length are assumed to be infinite. The heat radiation is negligible in this analytic solution. The detailed parameters can be found in Gringarten et al. (1975).

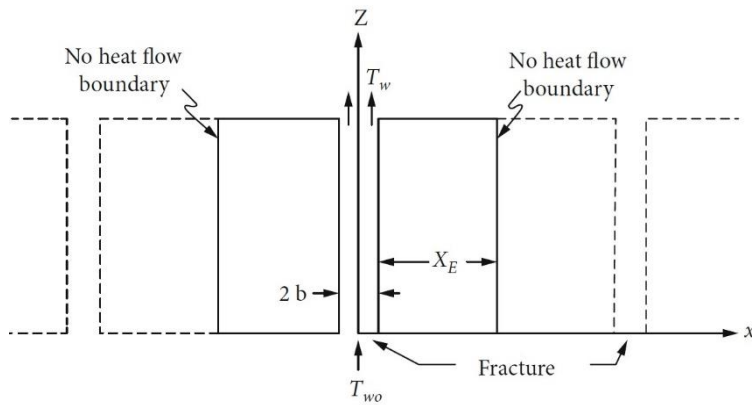


Figure 3.20. Mathematical model for fractured hot dry rock [41].

Figure 3.21 presents the results from the analytic solution and numerical simulation. It can be obtained that the model result has a very good agreement with the analytic solution which indicate the results from the numerical model is accurate. The discrepancy at the end of the simulation may come from the pre-assumption of the analytic solution, i.e., the length of the analytic solution is infinite while the value in the model is set to be 1km.

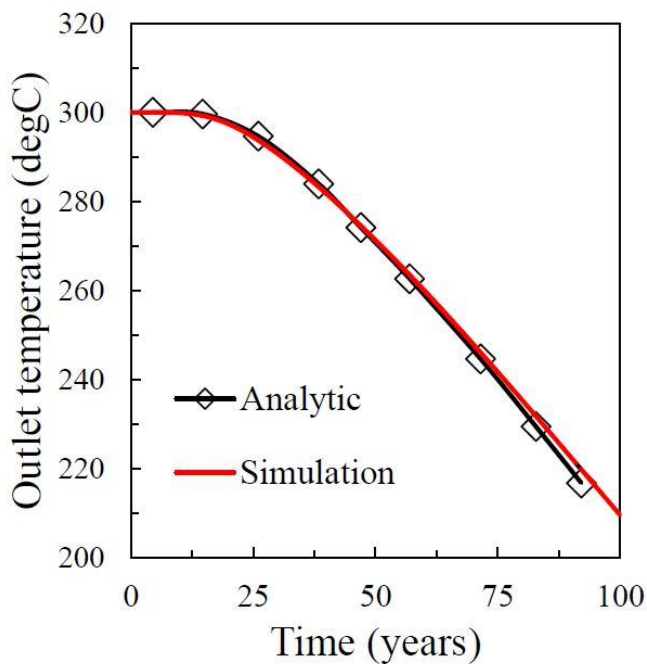


Figure 3.21. Comparison between the analytical solution and the numerical

simulation.

3.8. Acknowledgements

This work acknowledges financial support from the China scholarship council (CSC).

3.9. References

- [1] G. Hutterer, “Geothermal Power Generation in the World 2015-2020 Update Report,” Proceedings World Geothermal Congress 2021, Reykjavik, Iceland, (2021).
- [2] S.-M. Lu, “A global review of enhanced geothermal system (EGS),” *Renew. Sustain. Energy Rev.*, vol. 81, pp. 2902–2921, Jan. 2018, doi: 10.1016/j.rser.2017.06.097.
- [3] IEA (2019), Key World Energy Statistics 2019, IEA, Paris <https://www.iea.org/reports/key-world-energy-statistics-2019>
- [4] Lund, John & Bjelm, Leif & Bloomquist, Gordon & Mortensen, A.. (2008). Characteristics, development and utilization of geothermal resources - a Nordic perspective. Episodes. 31. 10.18814/epiiugs/2008/v31i1/019.
- [5] Armstead, H. Christopher H., and Jefferson W. Tester. 1987. Heat mining: a new source of energy. London: E. & F.N. Spon..
- [6] Brown, D. W., 1995. “The U.S. Hot Dry Rock Program- 20 Years of Experience in Reservoir Testing,” in Proceedings , World Geothermal Congress, May 18-31, 1995, Florence, Italy, International Geothermal Assn., Inc., Auckland, New Zealand, vol 4, pp 2607-2611 .
- [7] P. Olasolo, M. C. Juárez, M. P. Morales, S. D’Amico, and I. A. Liarte, “Enhanced geothermal systems (EGS): A review,” *Renew. Sustain. Energy Rev.*, vol. 56, pp. 133–144, Apr. 2016, doi: 10.1016/j.rser.2015.11.031.
- [8] C. R. Chamorro, J. L. García-Cuesta, M. E. Mondéjar, and A. Pérez-Madrado, “Enhanced geothermal systems in Europe: An estimation and comparison of the technical and sustainable potentials,” *Energy*, vol. 65, pp. 250–263, Feb. 2014, doi: 10.1016/j.energy.2013.11.078.
- [9] Z. Sun, “Numerical simulation of the heat extraction in EGS with thermal-hydraulic-mechanical coupling method based on discrete fractures model,” *Energy*, vol. 120, pp. 20–33, 2017, doi: <https://doi.org/10.1016/j.energy.2016.10.046>.
- [10] F. Gong *et al.*, “Evaluation of geothermal energy extraction in Enhanced Geothermal System (EGS) with multiple fracturing horizontal wells (MFHW),” *Renew. Energy*, vol. 151, pp. 1339–1351, May 2020, doi: 10.1016/j.renene.2019.11.134.
- [11] B. Guo, P. Fu, Y. Hao, C. A. Peters, and C. R. Carrigan, “Thermal drawdown-induced flow channeling in a single fracture in EGS,” *Geothermics*, vol. 61, pp. 46–62, May 2016, doi: 10.1016/j.geothermics.2016.01.004.
- [12] W. Cao, W. Huang, and F. Jiang, “A novel thermal–hydraulic–mechanical model for the enhanced geothermal system heat extraction,” *Int. J. Heat Mass Transf.*, vol.

- 100, pp. 661–671, Sep. 2016, doi: 10.1016/j.ijheatmasstransfer.2016.04.078.
- [13] C. Xu, P. A. Dowd, and Z. F. Tian, “A simplified coupled hydro-thermal model for enhanced geothermal systems,” *Appl. Energy*, vol. 140, pp. 135–145, Feb. 2015, doi: 10.1016/j.apenergy.2014.11.050.
- [14] D. Zhou, A. Tatomir, and M. Sauter, “Thermo-hydro-mechanical modelling study of heat extraction and flow processes in enhanced geothermal systems,” *Adv. Geosci.*, vol. 54, pp. 229–240, Jun. 2021, doi: 10.5194/adgeo-54-229-2021.
- [15] A. Borgia, K. Pruess, T. J. Kneafsey, C. M. Oldenburg, and L. Pan, “Simulation of CO₂-EGS in a Fractured Reservoir with Salt Precipitation,” *Energy Procedia*, vol. 37, pp. 6617–6624, 2013, doi: 10.1016/j.egypro.2013.06.594.
- [16] T. Guo, F. Gong, X. Wang, Q. Lin, Z. Qu, and W. Zhang, “Performance of enhanced geothermal system (EGS) in fractured geothermal reservoirs with CO₂ as working fluid,” *Appl. Therm. Eng.*, vol. 152, pp. 215–230, Apr. 2019, doi: 10.1016/j.applthermaleng.2019.02.024.
- [17] J. Li, “Investigations of heat extraction for water and CO₂ flow based on the rough-walled discrete fracture network,” *Energy*, vol. 206, no. 1, p. 33, Sep. 2020, doi: <https://doi.org/10.1016/j.energy.2020.118062>.
- [18] A. Borgia, K. Pruess, T. J. Kneafsey, C. M. Oldenburg, and L. Pan, “Numerical simulation of salt precipitation in the fractures of a CO₂-enhanced geothermal system,” *Geothermics*, vol. 44, pp. 13–22, Oct. 2012, doi: 10.1016/j.geothermics.2012.06.002.
- [19] M. Huang, “Numerical investigation on heat extraction performance of an enhanced geothermal system with supercritical N₂O as working fluid,” *Appl. Therm. Eng.*, p. 15, 2020, doi: <https://doi.org/10.1016/j.applthermaleng.2020.115436>.
- [20] T. Koch *et al.*, “DuMux 3 – an open-source simulator for solving flow and transport problems in porous media with a focus on model coupling,” *Comput. Math. Appl.*, vol. 81, pp. 423–443, Jan. 2021, doi: 10.1016/j.camwa.2020.02.012.
- [21] D. Gläser, B. Flemisch, R. Helmig, and H. Class, “A hybrid-dimensional discrete fracture model for non-isothermal two-phase flow in fractured porous media,” *GEM - Int. J. Geomath.*, vol. 10, no. 1, p. 5, Dec. 2019, doi: 10.1007/s13137-019-0116-8.
- [22] A.-B. Tatomir, *From discrete to continuum concepts of flow in fractured porous media*. Stuttgart: Inst. für Wasser- und Umweltsystemmodellierung, 2012.
- [23] A. B. Tatomir, A. Szymkiewicz, H. Class, and R. Helmig, “Modeling Two Phase Flow in Large Scale Fractured Porous Media with an Extended Multiple Interacting Continua Method”, *CMES-Computer Modeling in Engineering & Sciences*, 77(2), 81–112, doi: 10.3970/cmcs.2011.077.081.
- [24] Y. Ma *et al.*, “Analysis on the heat extraction performance of multi-well injection enhanced geothermal system based on leaf-like bifurcated fracture networks,” *Energy*, vol. 213, p. 118990, Dec. 2020, doi: 10.1016/j.energy.2020.118990.
- [25] S. N. Pandey, A. Chaudhuri, and S. Kelkar, “A coupled thermo-hydro-mechanical modeling of fracture aperture alteration and reservoir deformation during heat extraction from a geothermal reservoir,” *Geothermics*, vol. 65, pp. 17–31, Jan. 2017, doi: 10.1016/j.geothermics.2016.08.006.

- [26] W. Huang, "Heat extraction performance of EGS with heterogeneous reservoir: A numerical evaluation," *Int. J. Heat Mass Transf.*, p. 13, 2017, doi: <https://doi.org/10.1016/j.ijheatmasstransfer.2016.12.037>.
- [27] S. Saeid, R. Al-Khoury, and F. Barends, "An efficient computational model for deep low-enthalpy geothermal systems," *Comput. Geosci.*, vol. 51, pp. 400–409, Feb. 2013, doi: [10.1016/j.cageo.2012.08.019](https://doi.org/10.1016/j.cageo.2012.08.019).
- [28] H.A. Lauwerier, "The transport of heat in an oil layer caused by the injection of hot fluid", *Applied Scientific Research*, vol. 5, pp. 145–150, 1955, doi: <https://doi.org/10.1007/BF03184614>.
- [29] F. B. J. Barends, "Complete Solution for Transient Heat Transport in Porous Media, Following Lauwerier's Concept", SPE Annual Technical Conference and Exhibition, Florence, Italy, September 2010. doi: <https://doi.org/10.2118/134670-MS>.
- [30] A. Fox, P. L. Pointe, J. Hermanson, and J. Öhman, "Statistical geological discrete fracture network model - Forsmark modelling stage 2.2," Sweden: N. p., 2007. Web.
- [31] C. Darcel, "Statistical methodology for discrete fracture model – including fracture size, orientation uncertainty together with intensity uncertainty and variability," Sweden: N. p., 2009. Web. .
- [32] A. Rouleau and J. E. GALEt, "Statistical Characterization of the Fracture System in the Stripa Granite, Sweden," *International Journal of Rock Mechanics and Mining Sciences & Geomechanics Abstracts*, vol. 22, Issue 6, 1985, pp. 353-367, doi: [https://doi.org/10.1016/0148-9062\(85\)90001-4](https://doi.org/10.1016/0148-9062(85)90001-4), .
- [33] V. Cvetkovic, S. Painter, N. Outters, and J. O. Selroos, "Stochastic simulation of radionuclide migration in discretely fractured rock near the Äspö Hard Rock Laboratory: RETENTION IN FRACTURE NETWORKS," *Water Resour. Res.*, vol. 40, no. 2, Feb. 2004, doi: [10.1029/2003WR002655](https://doi.org/10.1029/2003WR002655).
- [34] J. Gong and W. R. Rossen, "Modeling Flow in Naturally Fractured Reservoirs: Effect of Fracture Aperture Distribution on Critical Sub-Network for Flow," *Pet. Sci.* 14, 138–154 (2017). <https://doi.org/10.1007/s12182-016-0132-3> .
- [35] Aharony, A. and D. Stauffer, "Introduction to percolation theory". 1992, Taylor & Francis.
- [36] Anongnart Assteerawatt, *Flow and transport modelling of fractured aquifers based on a geostatistical approach*. 2008. Accessed: Jun. 17, 2021. [Online]. Available: <https://nbn-resolving.org/urn:nbn:de:bsz:93-opus-36392>
- [37] M. Bonnet *et al.*, "Determining Crack Aperture Distribution in Rocks Using the ¹⁴C-PMMA Autoradiographic Method: Experiments and Simulations," *J. Geophys. Res. Solid Earth*, vol. 125, no. 1, Jan. 2020, doi: [10.1029/2019JB018241](https://doi.org/10.1029/2019JB018241).
- [38] S. P. Bertels, D. A. DiCarlo, and M. J. Blunt, "Measurement of aperture distribution, capillary pressure, relative permeability, and in situ saturation in a rock fracture using computed tomography scanning," *Water Resour. Res.*, vol. 37, no. 3, pp. 649–662, Mar. 2001, doi: [10.1029/2000WR900316](https://doi.org/10.1029/2000WR900316).
- [39] E. Hakami, "Aperture distribution of rock fractures," Tekniska högsk., Stockholm, 1995.
- [40] B. Figueiredo, C.-F. Tsang, and A. Niemi, "The Influence of Coupled

Thermomechanical Processes on the Pressure and Temperature due to Cold Water Injection into Multiple Fracture Zones in Deep Rock Formation,” *Geofluids*, vol. 2020, pp. 1–14, Jan. 2020, doi: 10.1155/2020/8947258.

[41] A. C. Gringarten, P. A. Witherspoon, and Y. Ohnishi, “Theory of heat extraction from fractured hot dry rock,” *J. Geophys. Res.*, vol. 80, no. 8, pp. 1120–1124, Mar. 1975, doi: 10.1029/JB080i008p01120.

Chapter 4.

Assessment of EGS Performance Employing Supercritical CO₂ and H₂O as Working Fluids in a Fractured-Porous Reservoir by Two-Phase Flow Modelling

Dejian Zhou¹, Alexandru Tatomir^{1,2}, Ingrid Tomac³, Martin Sauter¹

¹Department of Applied Geology, Geoscience Center Göttingen, University of Göttingen, Germany

²Department of Earth Sciences, Geocentrum, Uppsala University, Sweden

³Department of Structural Engineering, University of California, San Diego, USA.

Keywords:

Multi-dimensional two-phase flow system

Supercritical carbon dioxide

Discrete fracture network

Three kinds of geothermal reservoirs

Enhanced geothermal system

Citation:

Zhou, D., Tatomir, A., Tomac, I., Sauter, M., Assessment of EGS Performance Employing Supercritical CO₂ and H₂O as Working Fluids in a Fractured-Porous Reservoir by Two-Phase Flow Modelling., Applied Thermal Engineering, Under Review.

Abstract

With the development of Enhanced Geothermal Systems (EGS) technology, geothermal energy became considerably more feasible worldwide. In the effort to reduce atmospheric emissions of greenhouse gases, supercritical carbon dioxide (scCO₂) emerged as an appealing working fluid alternative to water. A lower-dimensional numerical model for non-isothermal two-phase flow in fractured porous media is implemented in the open-source software DuMu^X to simulate the multiphase fluid flow and heat transport in an EGS reservoir. This paper compares the performances of three specific EGS setups: 1) the combined scCO₂-H₂O-EGS; 2) scCO₂- saturated EGS; and 3) H₂O- saturated EGS. Results show that the heat production rate of the combined scCO₂-H₂O EGS is higher than that of scCO₂- and of the H₂O- saturated EGS. Furthermore, the spatial temperature distributions in the mixed scCO₂- H₂O-EGS and scCO₂-saturated EGS are similar but differ considerably from the H₂O- saturated EGS. The injection rate increase leads to improved performance of the reservoirs employing scCO₂ as a working fluid. The improved performance is due to an increase in the total produced geothermal energy, while the reservoir lifespan remains unchanged. In contrast, H₂O-EGS show a reduction in the total produced geothermal energy due to a significant decrease in the reservoir lifespan.

4.1. Introduction

This paper evaluates the advantages of supercritical carbon dioxide (scCO₂) over H₂O as a working fluid for geothermal energy extraction in porous, fractured Enhanced Geothermal Systems (EGS) over a reservoir lifespan. A better understanding of the multiphase flow and transport processes in fractured reservoirs is essential for the decision-making and planning of the EGS employing scCO₂ as a working fluid. Thus, using scCO₂ as a working fluid in an EGS becomes potentially attractive.

EGS can utilize the geothermal energy stored in the deep hot rock formations, addressing some of the current environmental challenges, such as reducing greenhouse gas emissions and the energy transition from fossil fuels [1], [2]. Generally, EGS reside

at depths between 3 km and 10 km [3], where rock mass temperatures exceed 150 °C [4]. A low-temperature working fluid circulates through the hot rock matrix of the geothermal reservoir, heats up, and transports thermal energy to a production well [5]. EGS can theoretically be placed at any location because of the rock permeability enhancement via hydraulic fracturing or reopening of existing fractures by hydro-shearing [6].

To date, the performances of EGS using water (H₂O) and supercritical carbon dioxide (scCO₂) as working fluids are widely investigated [7]. Because field experiments at the depths of several kilometers are costly to set up and operate, numerical models are frequently used and remain a preferred method to investigate EGS performance to date. After Pruess et al. (2006) first pointed at the possibility of employing scCO₂ as a working fluid for EGS [8], [9], the development of numerical models for the EGS heat extraction using the scCO₂ as working fluid ramped up significantly [10]–[13]. However, most existing models assume that the fluid that geothermal reservoirs are initially saturated with is identical to the working fluid. For example, Guo et al. [14] applied the commercial software COMSOL Multiphysics to build a three-dimensional (3D) coupled thermo-hydro-mechanical (THM) model with a discrete fracture network (DFN). They found that scCO₂-saturated EGS generates more energy than H₂O-saturated EGS for the same production conditions. Li et al. [15] developed a two-dimensional (2D) rough-walled discrete fracture network model that includes the coupled THM processes to investigate the heat production using scCO₂ as the working fluid. They found that the heat production rate of H₂O-saturated EGS is more significant than that of scCO₂-saturated EGS for the short-term period, but less considerable for the long-term production. This is because the lower heat capacity of scCO₂ delays the breakthrough of the cold plume, which leads to a higher production temperature compared to H₂O-saturated EGS. Based on a 3D numerical model, Wang et al. [16] investigated mass losses when using scCO₂ and H₂O as working fluids in reservoirs saturated with identical fluids, respectively. The fluid loss rate of scCO₂-saturated EGS depends on the permeability and the initial temperature of the geothermal reservoir. At

high average reservoir permeability and high initial temperatures, the fluid loss rate of scCO₂-saturated EGS is much higher than that of H₂O-saturated EGS. In contrast, the fluid loss rate is lower at low average reservoir permeability and low initial temperature. Besides the scCO₂-saturated EGS and H₂O-saturated EGS, several studies explored combined scCO₂-H₂O systems, where geothermal reservoirs are assumed to be initially fully saturated with H₂O while the injected working fluid is scCO₂ [7]. Different from the Carbon-dioxide Geothermal Plume (CGP) technology, in which the existing natural fractures are applied, the scCO₂-H₂O EGS is a man-made fractured permeable reservoir, which is located several kilometers underground. For example, Borgia et al. [17], [18] proposed a two-phase flow dual-porosity continuum numerical model with TOUGH2 to simulate the phase displacement and heat flow and transport in EGS. Findings show that the most crucial benefit of the combined scCO₂-H₂O EGS is that the actual heat flow rate from a given reservoir could be up to five times larger than the heat flow rate achievable with water as a working fluid. However, in the combined scCO₂-H₂O EGS, scCO₂ partially recovers during the production phase because of the buoyancy and capillary trapping. Nevertheless, when most scCO₂ recovers, at least 10% of the pore volume remains filled with residual, capillary trapped scCO₂. Liao et al. [19] presented a continuum anisotropic permeability model to simulate the combined scCO₂-H₂O EGS using the same simulator as Borgia et al. The simulations show that the geothermal reservoir can maintain a relatively stable heat production with scCO₂ as a working fluid because of the low injection pressure. On the other hand, the final cooldown temperature of the production fluid plays an essential role in evaluating EGS performance. For example, Guo et al. defined the reservoir lifespan as when the production temperature decreases from the initial temperature to 120°C [20]. Similarly, Su et al. proposed 150°C for the reservoir lifespan [21]. However, a lower fluid temperature is still widely accepted for operating purposes. For example, municipal district heating uses fluid temperatures lower than 80°C [22], [23]. Meanwhile, the reservoir lifespan and the heat production rate are also controlled by the injection rate [4], [24]–[26].

Although EGS with scCO₂ working fluid has already been investigated, previous studies focused on either single-phase flow systems with fractures or two-phase flow system without fractures. Specifically, the considered working fluid is the same as the initial fluid in the fully saturated domain in the single-phase flow system. At the same time, the equivalent continuum models lack the representation of the fractures as discrete elements [27]–[29]. The studies on combined scCO₂-H₂O EGS simulating the two-phase flow system in discrete fracture networks are rare. The simulation of EGS should contain both fractures and matrix to represent the natural enhanced geothermal reservoirs in EGS as much as possible [27]–[29]. Thus, this study uses a fully coupled thermal-hydraulic (T-H) model with a discrete fracture network to simulate the phase displacement and heat transfer in an enhanced geothermal reservoir. The newly studied combined scCO₂-H₂O EGS is compared with the two similar types of enhanced geothermal reservoirs, i.e., scCO₂-saturated EGS and H₂O-saturated EGS.

Furthermore, this study considers an advanced representation of discrete fracture networks, including the partial-raster concept for fracture aperture [30]. This study assumes randomly distributed fracture apertures, following the normal distribution, allowing a more realistic representation of the geothermal reservoir [30]. The EGS performance is evaluated based on standard variables such as the fluid production temperature and the heat production rate. In addition, this work addresses a gap in the literature by investigating the impacts of the final cooldown temperatures lower than 120 °C and the variable injection rates on the EGS performance.

4.2. Methodology

4.2.1. Problem definition

A fully coupled, non-isothermal two-phase flow discrete fracture model TH model is implemented in DuMu^X [31], [32], an open-source simulator for solving flow and transport problems in porous media. The model investigates fluid flow, phase displacement, and heat transport in a fractured porous georeservoir under the following assumptions:

- The simulated EGS reservoir consists of a porous rock matrix and a DFN. A continuum porous medium represents the rock matrix with homogeneous and isotropic permeability and porosity. The porosity of the rock matrix is constant during the simulation, while the permeability varies with effective pore pressure and temperature changes.
- The fractures are represented as lower-dimensional entities, i.e., the rock matrix is two-dimensional while the DFN is one-dimensional. Fracture aperture varies between different fractures, but it is constant within an individual fracture. The cubic law model governs fracture permeability.
- As the temperatures in the reservoir are lower than 220°C, and the pore pressures are higher than 20 MPa, over the entire simulation, the working fluids in the reservoir do not change phase, i.e., water remains liquid, the scCO₂ supercritical. [33]. Convection and conduction govern the heat exchange between water and rock matrix.
- The fractures are assumed to be created or reopened before the beginning of the simulation. Therefore, there are no new fractures created during the simulation.
- The geochemical reaction between scCO₂ and minerals may reach to equilibrium at the initial production period, for the long-term production, the geochemical reactions have minimal effects on reservoir performances. Thus, this work ignores the reactions between scCO₂ and minerals.

The numerical models, i.e., multi-domain 2pmodel, are implemented in the open-source software, DuMu^X. In the model of the combined scCO₂-H₂O EGS, the geothermal reservoir is initially fully saturated with H₂O, while the injected working fluid is scCO₂. In the CO₂-saturated EGS and the H₂O-saturated EGS, the initially saturated fluids and the injected working fluids are the same and are scCO₂, and H₂O, respectively. The geothermal reservoir is located at 6000 m underground, whose size is 1000 m × 100 m with an effective width of 1 m.

As a fracture network is essential for EGS, the DFN needs to represent the natural

geological structure. In that sense, a (geo)statistical fracture generator can distribute fractures in the DFN model. Previous publications [40]–[44] proposed a configuration of three fracture sets, with fracture orientations of 10° , 95° , and 170° for crystalline rocks. The fracture traces range between 100 m and 500 m in length. The partial-raster concept varies fracture apertures, following a normal distribution [30], [43], [45]. Specifically, the mean value of fracture aperture is 1 mm with the standard deviation of 0.5. **Figure 1** presents the fracture network simplifying process from the statistically generated fracture network. Firstly, 51 fractures are generated, as presented in **Figure 1(a)**. In **Figure 1(b)**, the fractures presented in red are isolated fractures, which are not connected to both the left and right boundaries of the simulated reservoir. They affect the reservoir performance only at initial production period, i.e., before the phase breakthrough at production well, approximately 5 days, but have minimal influence for the long-period production, i.e., 30 years. On the other hand, the isolated fractures increase the numerical instability and require a higher computational capacity. Thus, the isolated fractures are removed, and only the fracture network connecting the left and right boundaries is kept. Zhou et al. and Gong et al. [30], [46] described a method to obtain the simplified fracture network in detail.

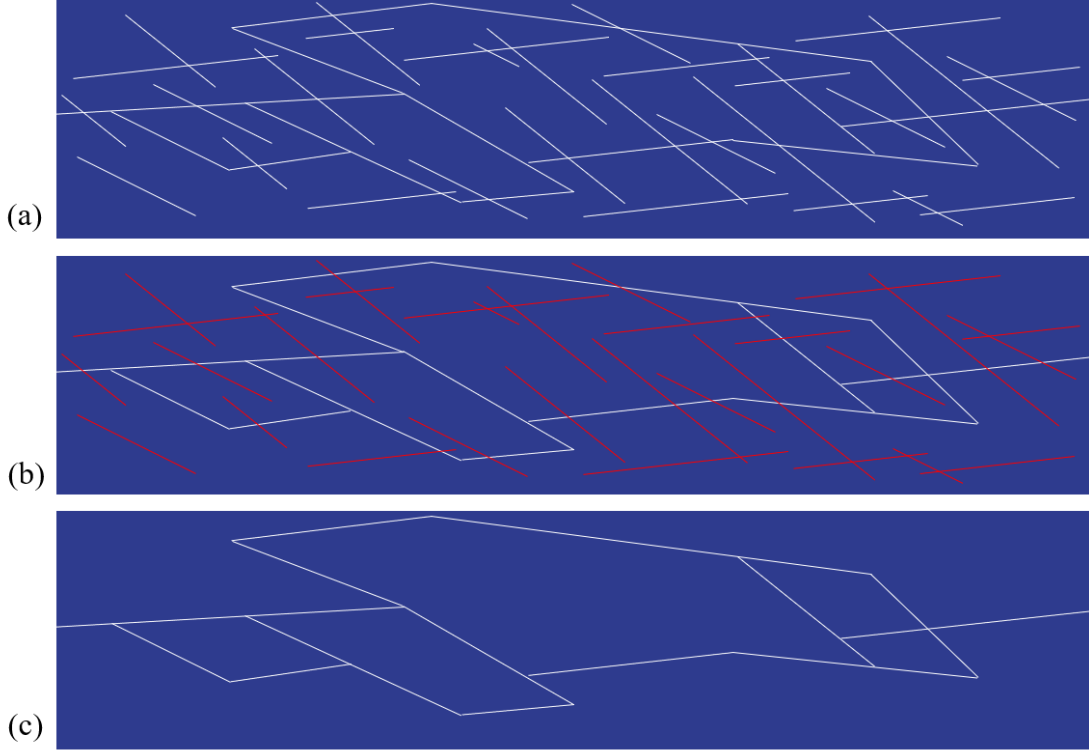


Figure 4.1. The generation of discrete fracture network: (a) initial fracture network; (b) the main fractures (white) and isolated fractures (red), and (c) the main fractures.

4.2.2. Numerical and Mathematic model

This work considers the flow of two immiscible fluids. The mass balance equation of the fluid phase α in a porous medium is:

$$\phi \frac{\partial(\rho_{\alpha} S_{\alpha})}{\partial t} + \nabla \cdot (\rho_{\alpha} \mathbf{v}_{\alpha}) + q_{\alpha} = 0, \quad \alpha \in \{w, n\} \quad (1)$$

where ϕ is the porosity of rock matrix which remains constant, ρ_{α} is the density of phase α , t is time, S_{α} is the phase saturation, \mathbf{v}_{α} is the fluid phase flow velocity, and q_{α} is the mass source, the subscript α denotes the phase index, w and n refer to the wetting and non-wetting phases. Darcy's law expresses the fluid phase flow velocity through the rock mass:

$$\mathbf{v}_{\alpha} = -\frac{k_{r\alpha}}{\mu_{\alpha}} \mathbf{K}(\nabla p_{\alpha} + \rho_{\alpha} \mathbf{g}) \quad (2)$$

where \mathbf{K} is the intrinsic permeability tensor of the rock matrix, which is assumed to be

isotropic in this work, μ_α is the fluid phase dynamic viscosity, $k_{r\alpha}$ is the relative permeability, p_α is the phase pressure, and \mathbf{g} is the gravitational acceleration. The phase saturation and pressure satisfied the relationships:

$$S_n + S_w = 1 \quad (3a)$$

$$p_n = p_w + p_c \quad (3b)$$

in which the p_c is the capillary pressure. The capillary pressure relationship with water saturation can be described by the van Genuchten equation [34]:

$$S_{we} = S_{wr} + \frac{1}{[1+(p_c/p_e)^n]^{1-1/n}} \quad (3c)$$

$$k_{rw} = S_{we}^{1/2} (1 - (1 - S_{we}^{1/m})^m)^2 \quad (3d)$$

$$k_{rnw} = (1 - S_{we})^{1/2} (1 - S_{we}^{1/m})^{2m} \quad (3e)$$

where p_e is the air entry pressure, n is an index of the pore-size distribution, and S_{wr} is the residual wetting-phase saturation, m is the function of n , i.e., $m = 1-1/n$.

All constituents within a representative elementary volume, i.e., the wetting, non-wetting, and porous media, are in local thermal equilibrium. The thermal energy balance equations are:

$$\phi \sum_\alpha \frac{\partial \rho_\alpha S_\alpha u_\alpha}{\partial t} + (1 - \phi) \frac{\partial \rho_s c_s T}{\partial t} + \nabla \cdot (\sum_\alpha \rho_\alpha h_\alpha \mathbf{v}_\alpha - \lambda \nabla T) = q_h \quad (4)$$

where T is the temperature, u_α and h_α are phase-specific internal energies and enthalpies, ρ_s and c_s are the density and the heat capacity of rock matrix, λ is the thermal conductivity coefficient of the rock matrix, and q_h is the heat flux at the source point.

Temporal discretization uses the implicit Euler scheme. For solving the non-linear system of equations, the Newton-Raphson method is applied together with the direct solver UMFPack [35].

The fractures within the rock matrix can strongly influence fluid flow and heat transport because fracture hydraulic properties can be orders of magnitude higher than that of the surrounding rock matrix [36]. Similar with rock matrix, the following equations represent the fluid flow, phase displacement, and the heat transfer in discrete fracture network:

$$a\phi_f \frac{\partial(\rho_{\alpha,f} S_{\alpha,f})}{\partial t} - a\nabla \cdot \left(\rho_{\alpha,f} \frac{k_{r\alpha,f}}{\mu_{\alpha,f}} \mathbf{K}_f (\nabla p_{\alpha,f} + \rho_{\alpha,f} \mathbf{g}) \right) = q_{\alpha,f-m} \quad (5)$$

$$a\phi_f \sum_{\alpha,f} \frac{\partial \rho_{\alpha,f} S_{\alpha,f} u_{\alpha,f}}{\partial t} + a(1 - \phi_f) \frac{\partial \rho_{s,f} c_{s,f} T_f}{\partial t} + a\nabla \cdot (\sum_{\alpha,f} \rho_{\alpha,f} h_{\alpha,f} \mathbf{v}_{\alpha,f} - \lambda_f \nabla T_f) = q_{h,f-m} \quad (6)$$

where a is the fracture aperture, $q_{\alpha,f-m}$ and $q_{h,f-m}$ are the mass and energy transfers between fracture and surrounding rocks, and \mathbf{K}_f is the fractures permeability, which can be described by cubic law based on previous publications [20], [30]:

$$\mathbf{K}_f = \frac{a^2}{12} \quad (7)$$

A detailed description of the numerical model, discretization methods, and mass and energy transfers between fracture and surrounding rocks can be found in Gläser et al., 2017 and 2019 [36], [37]. The model assumes that the local thermal equilibrium can be applied in each representative elementary volume. Therefore, the temperatures of fluid and matrix are the same in the respective representative elementary volumes. The pore pressure is the effective pore pressure, an average of wetting and non-wetting phase pressure. Rutqvist et al. [38] used the normal fracture stiffness k_n to describe the relationship between the aperture variation and change of effective stress. In this work, the model assumes that the change of effective stress is equal to the change in pore pressure. Thus, the variation of fracture aperture can be written as following:

$$\Delta a_p = \frac{\partial p_e}{k_n} \quad (8)$$

where p_e is the effective pressure, i.e., $p_e = \sum S_\alpha p_\alpha$. On the other hand, the fracture aperture variation with the change of temperature is:

$$\Delta a_T = a \cdot \alpha_T \Delta T \quad (9)$$

where α_T is the effective thermal expansion coefficient and can be defined as $\alpha_T = \sum S_i \cdot \alpha_i$, the α_i is the phase i ($i = n, w$) thermal expansion coefficient. The total aperture change is the summation of changes from pressure and temperature:

$$\Delta a = \Delta a_T + \Delta a_p \quad (10)$$

4.2.3. Parameters for evaluating the geothermal reservoir performance

This section presents the parameters and criteria for the evaluation of the performance of the simulated geothermal reservoir [4], [14], [30], [39]. The parameters include the production temperature, heat production rate, total production rate, reservoir lifespan, and energy efficiency, which are defined as follows:

(i) Production temperature (T_o [°C]) is calculated according to:

$$T_o = \frac{\sum q_f T_f + \int q_s T_s dy}{\sum q_f + \int q_s dy} \quad (11)$$

where q_f [m/s] and q_s [m/s] are the fluxes from fractures and matrix, respectively.

(ii) Heat production rate ($P(t)$ [kW]):

$$P(t) = Q_f C_{p,eff}(T_o - T_{in}) + Q_s C_{p,eff}(T_o - T_{in}) \quad (12)$$

where Q_f [kg/s] and Q_s [kg/s] are the production fluid flux from fractures and matrix, respectively. The total production flux equals the injection rate, i.e., $Q_{in} = Q_s + Q_f$. $C_{p,eff}$ [kJ/kg/°C] is the heat capacity of the produced fluid, for the combined CO₂-H₂O EGS, $C_{p,eff} = \sum S_\alpha C_{p,\alpha}$ ($\alpha = n, w$).

(iii) Total production rate (E_{total} [kJ]):

$$E_{total} = \int_0^{t_{end}} P(t) dt \quad (13)$$

Where t_{end} [year] is the production period.

(iv) The reservoir lifespan

The reservoir lifespan is the time [years] when the production temperature decreases from the initial temperature to the final cooldown production temperature (T_{end}). In sections 3.1 and 3.2, $T_{end} = 120$ °C, while in section 3.3, the $T_{end} = 120$ °C, 90 °C, 60 °C, and 30 °C are investigated.

4.2.4. Initial and boundary conditions

The initial pressure distribution in the simulated geothermal reservoir results from the hydrostatic pressure (9.81 MPa/km) and the atmospheric pressure (0.1 MPa). The initial temperature of the system increases linearly from 191.15 °C at the top of the reservoir with a constant thermal gradient of 0.03 °C/m. The working fluid is injected

from the left side of the boundary with the injection temperature $T_{in} = 30 \text{ }^\circ\text{C}$. The Working fluid with a flow rate of 3.57 L/s is injected and produced from the left and right boundaries. The volume rate, instead of the mass rate, is employed to ensure a fair comparison among the three EGS setups. To be specifically, the volume rate is not affected by the varying phase saturations, and can be kept constant during the entire production period. The injection and production areas are between 25 m and 75 m on the left and right boundaries. In contrast, the remaining right boundary areas remain at initial conditions, i.e., the boundary pressure is the same as the initial reservoir pressure. The top and bottom are no-flow boundaries, as presented in **Figure 4.2**, in which the color-coded fractures present the various apertures of the DFN. The brine (H_2O) and scCO_2 physical properties are obtained from the International Association for the Properties of Water and Steam (IAPWS) [47] and Span and Wagner (1996) [48]. The parameters employed in this work are based on the former publications [36], [37], and summarized in **Table 4.1**.

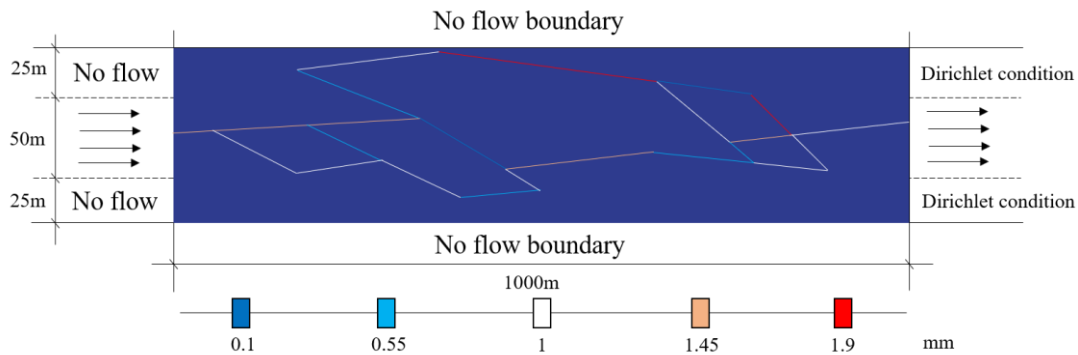


Figure 4.2. Illustration of the boundary conditions of the proposed model and of the main fracture network aperture sizes (in coloured bar).

Table 4.1. Parameters for the simulations

Parameters	value
Density of rock matrix (kg/m^3)	2700
Porosity of fractures (-)	0.85
Porosity of rock matrix (-)	0.01

Permeability of rock matrix (m ²)	1×10^{-15}
Thermal conductivity of rocks (W/m/°C)	2.8
Heat capacity of rocks (J/kg/°C)	790
Brine salinity (-)	0.1
Air enter pressure of fracture (Pa)	1000
Van Genuchten coefficient n of fracture (-)	3
Air enter pressure of rocks (Pa)	10000
Van Genuchten coefficient n of rocks (-)	3
Residual wetting phase saturation (-)	0
Normal stiffness (GPa/m)	500
Thermal expansion coefficient (brine) (1/°C)	10^{-4}
Thermal expansion coefficient (scCO ₂) (1/°C)	10^{-5}

4.2.4. Sensitivity analysis concerning the discretization

For the study domain containing the simplified DFN, a conforming finite element mesh is generated with Gmsh, a finite element mesh generator with built-in pre-and post-processing facilities [49]. The mesh is generated and checked automatically within the software. The finite element number plays an essential role in the accuracy of the simulation results. Thus, the sensitivity analysis tests the numerical solution's accuracy and determines the optimal mesh size. **Figure 4.3** illustrates the finite element meshes used in the sensitivity analysis. **Figure 4.4** shows the analysis curve of scCO₂ saturation at the production well plotted for the grids. By increasing the element number, the scCO₂ saturation at a production well in the 30th year grows until reaching a constant level. For example, when the element number increases to 8776, the scCO₂ saturation is 0.598; then, the saturation remains at the level of approximately 0.6. Therefore, considering the available computational capacity, the grid with 8776 elements is selected to guarantee the accuracy of the numerical simulation.

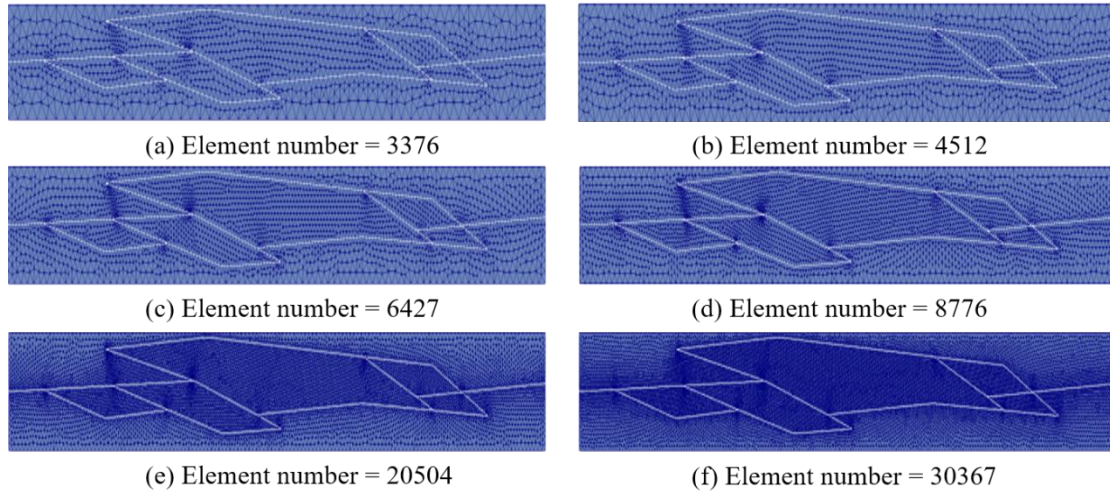


Figure 4.3. Representation of the different grid discretization and the corresponding finite element numbers

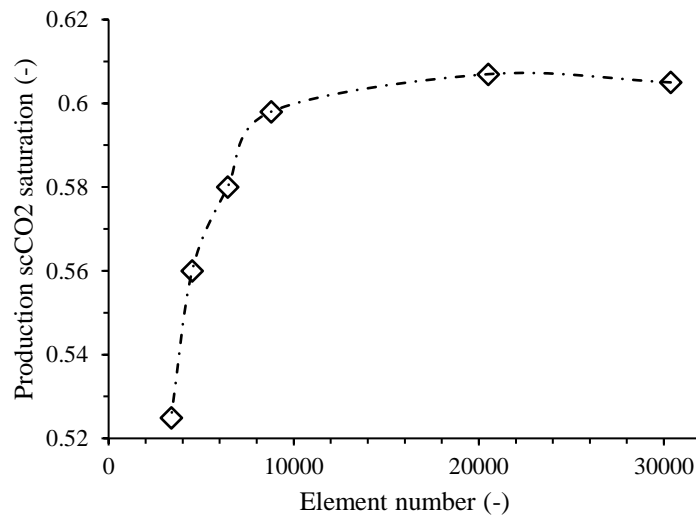


Figure 4.4. Relationship between scCO₂ saturation at the production well in 30th year and mesh refinement (element number).

4.3. Results

4.3.1. Comparison of the geothermal reservoirs performances using working fluids scCO₂ and H₂O

This section compares reservoir production temperatures and heat production rates with scCO₂ and water as working fluids. In addition, the discrepancy between the combined scCO₂-H₂O EGS and the scCO₂- saturated EGS is presented. **Figure 4.5** shows the

saturation distribution of scCO₂ in the 1st, 5th, 10th, and 30th years for the combined scCO₂-H₂O EGS, where scCO₂ is injected into the reservoir initially saturated with H₂O. The fractures are the primary scCO₂ flow paths. Thus, the fractures' saturation is much higher than in the surrounding rock matrix in the 1st year. As the production progresses, more injected scCO₂ enters the rock matrix from the fractures. Furthermore, the buoyancy begins to dominate the scCO₂ transport mechanism, resulting in a predominately upward migration that is visible later.

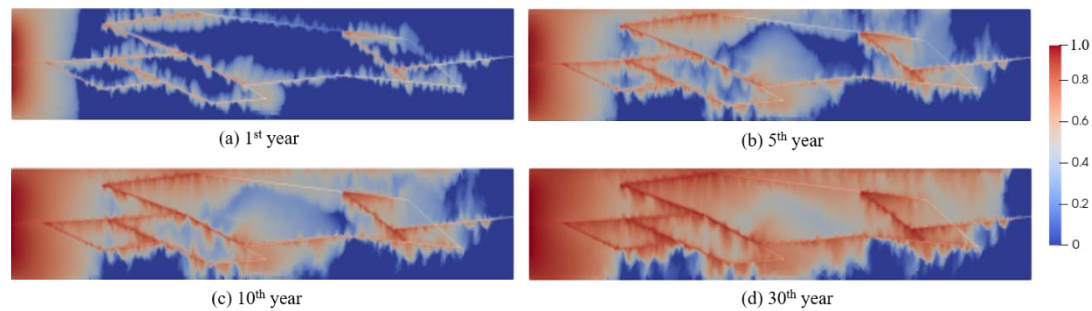


Figure 4.5. Spatial distribution of scCO₂ saturation after 1, 5, 10, and 20 years.

Figure 4.6 compares the temperature distributions among the three considered reservoir scenarios after years 5 and 30. For the combined scCO₂-H₂O EGS, the scCO₂ is injected into a fully H₂O saturated reservoir, while in the scCO₂-saturated EGS and H₂O-saturated EGS, injected and saturation fluids are the same. It can be observed from the temperature distribution of H₂O-saturated EGS in the 5th year that fractures represent preferential paths for fluid flow and heat transport. The temperature in fractures is significantly lower than that in the surrounding rock matrix. The temperature distribution of the combined scCO₂-H₂O EGS is very similar to that of the scCO₂-saturated EGS but considerably different than that of H₂O-saturated EGS. The cold temperature fluid primarily accumulates near the injection well when employing the scCO₂ as the working fluid, while in other areas, the temperature remains unchanged during the 30-year production. When applying H₂O as working fluid, the temperature of the cold water has a much wider distribution due to the higher density and high heat capacity of H₂O compared to scCO₂ under reservoir pressure and temperature. The

same injection rate takes more thermal energy to heat cold H₂O than scCO₂. Thus, the temperature of the H₂O-saturated EGS rock matrix changes more rapidly than that of the scCO₂-saturated EGS and of the combined scCO₂-H₂O EGS. The lower part of **Figure 4.6** presents the flow velocities within the fractures among the three reservoirs. The flow velocity of the combined scCO₂-H₂O EGS is similar to that of scCO₂ saturated EGS but slightly lower than that of H₂O saturated EGS. On the other hand, H₂O has a significantly larger density and heat capacity than scCO₂, resulting in a higher Peclet number (Pe) of H₂O saturated EGS according to **Eq. 18**:

$$Pe = v\rho C_p D/k \quad (18)$$

where Pe is the Peclet number, v is the average flow velocity among the fractures, C_p is heat capacity, D is the characteristic length, which is assumed to be the fracture aperture in this work, k is the thermal conductivity. The Peclet number reflects whether the heat convection or conduction dominates the heat transfer in the enhanced geothermal reservoirs, indicating why the temperature distributions among the three kinds of EGS are different. The relationships among the Pe, output temperature, and heat production rate of the three types of enhanced geothermal reservoirs are summarised in **Table 4.2**. It is observed that Pe of H₂O- saturated EGS is much larger than these of scCO₂- saturated EGS and combined scCO₂- H₂O EGS. The higher Pe presents the heat convection dominates over heat conduction. Thus, the heat is transported faster in H₂O- saturation EGS than in the reservoirs using scCO₂ as working fluid, resulting in the shorter temperature breakthrough time of H₂O- saturated EGS. Furthermore, the fluid volume within the rock matrix is very small due to the porosity of 0.01. Thus, the pore fluid can only provide minimal thermal energy for heating the cold working fluid, while the rock matrix supplies most. Therefore, the influence of the fluid which initially saturates the rocks on heat transfer can be ignored, as the combined CO₂-H₂O – EGS and CO₂ saturated- EGS result in similar temperature distribution.

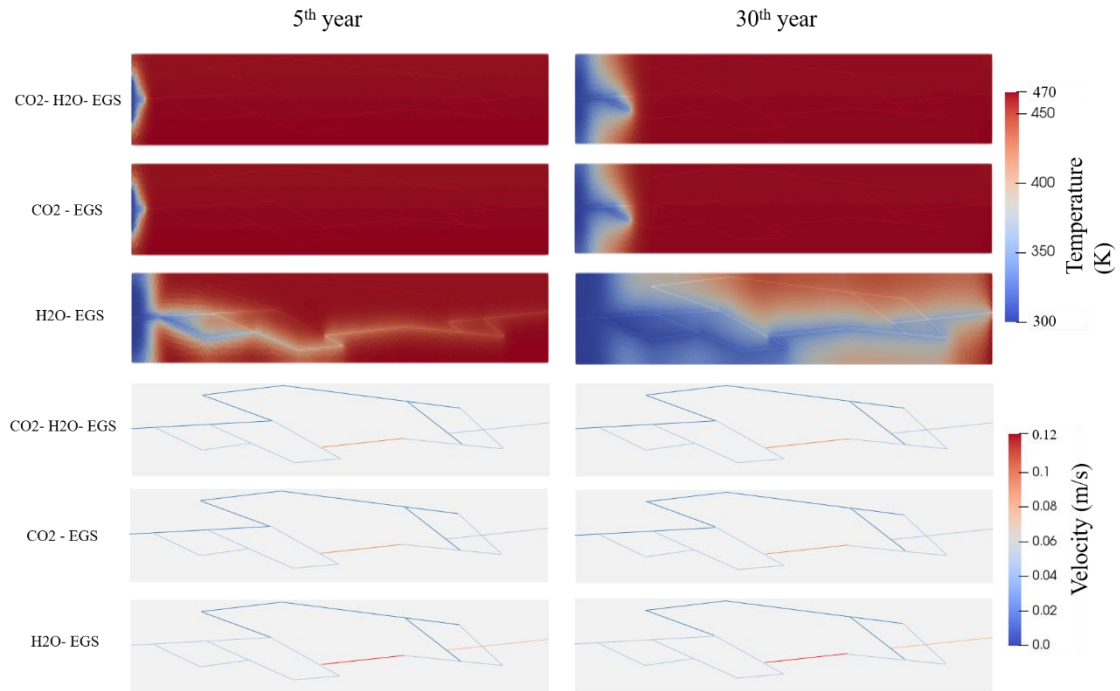


Figure 4.6. Temperature (top) and fractures (bottom) velocity distributions among the combined scCO₂- H₂O- EGS, scCO₂- saturated EGS, and H₂O- saturated EGS after years 5 and 30.

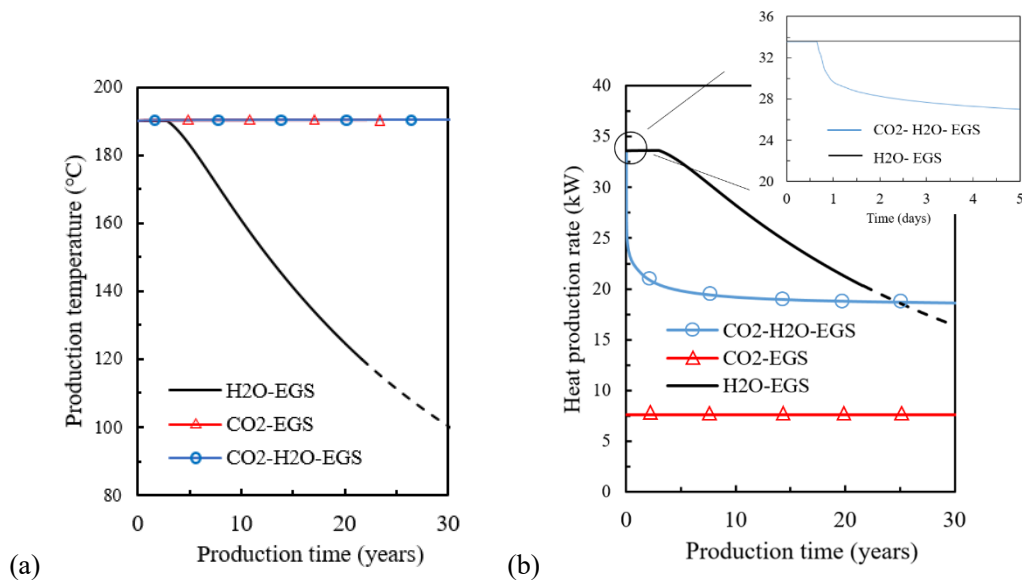
Table 4.2. Relationships between Peclet number (Pe), temperature breakthrough time, and heat production rate.

EGS types	Pe		Output Temperature (°C)		Temperature BT time (years)
	5 th	30 th	5 th	30 th	
combine scCO ₂ and H ₂ O	9.14	9.22	191.15	191.15	30
scCO ₂ saturated	9.14	9.22	191.15	191.15	30
H ₂ O saturated	81.3	82.5	183.03	100.12	2.8

Figure 4.7 presents (a) the production temperature evolution versus the production time and (b) the heat production rate versus the production time for the combined scCO₂-H₂O EGS, scCO₂-saturated EGS, and H₂O-saturated EGS. The production temperatures of the combined scCO₂-H₂O EGS and the scCO₂-saturated EGS remain unchanged because the cold plumes have not arrived at the production well at the end of 30th year production, as presented in **Figure 4.6**. Conversely, the production temperature of the

H₂O-saturated EGS has a reduction after the initial stable period. The reservoir lifespan ends when the production temperature decreases from the initial temperature to 120 °C. Therefore, the scCO₂ reservoirs have a lifespan much longer than 30 years.

On the other hand, the H₂O saturated EGS lifespan is approximately 20 years. **Figure 4.7(b)** shows that the heat production rate of scCO₂ saturated EGS is much lower than that of combined scCO₂-H₂O EGS and H₂O saturated EGS. The lower scCO₂ heat production rate results from the lower heat capacity of scCO₂ than that of H₂O. For the combined scCO₂-H₂O EGS, before the scCO₂ plume reaches the production well, all the produced fluid is H₂O. Thus, the heat production rate of the combined scCO₂-H₂O EGS is the same as H₂O-saturated EGS at the early stage. Then, because of the breakthrough of scCO₂ at the production well, when the saturation of scCO₂ at the production boundary starts to increase, the heat production rate of the combined scCO₂-H₂O EGS begins to drop presented in **Figure 4.7(c)**. On the other hand, the reduction of the heat production rate of H₂O-saturated EGS results from the decrease of the production temperature.



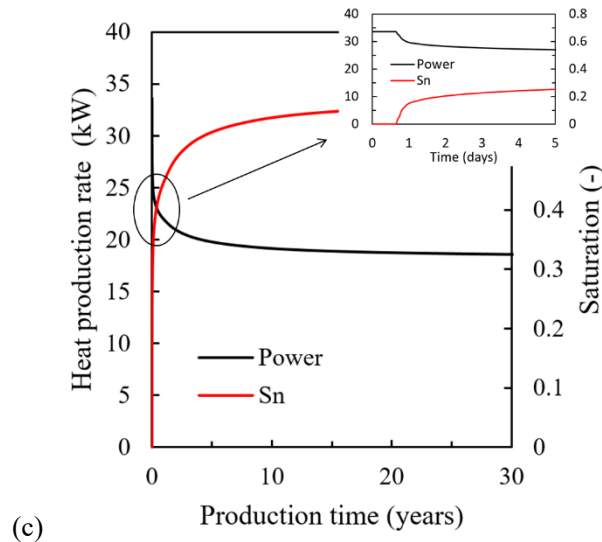


Figure 4.7. The relationship between (a) production temperature and (b) heat production rate and production time in the combined scCO₂-H₂O EGS, scCO₂-saturated EGS, and H₂O-saturated EGS. The black dash line presents the results without considering the reservoir lifespan, i.e., the production still proceeds when production temperature is lower than 120 °C, and (c) The relationship between heat production rate ("power" in the legend) and scCO₂ saturation ("Sn" in the legend).

Figure 4.8 illustrates the relationship between the total produced thermal energy and production time. The black dash line presents the total produced thermal energy without considering the reservoir lifespan. The scCO₂- saturated EGS yields the lowest total thermal energy produced, while the H₂O-saturated EGS has the highest thermal energy. The total produced thermal energy of the combined scCO₂-H₂O EGS is between the scCO₂ saturated EGS and H₂O saturated EGS. However, considering the reservoir lifespan of H₂O saturated EGS, the total produced geothermal energy from the combined scCO₂-H₂O EGS generally approaches and finally exceeds that of H₂O-saturated EGS at the approximately 30th year. Thus, although the H₂O-saturated EGS has the most prominent thermal energy output at the beginning of the production, the short lifespan restricts the sustainable application and development of the H₂O-saturated EGS.

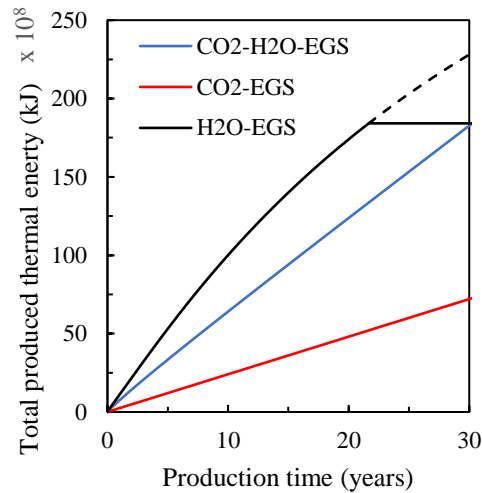


Figure 4.8. The relationship between total produced thermal energy and production time among combined scCO₂-H₂O EGS, scCO₂-saturated EGS, and H₂O-saturated EGS. The black dash line presents the results without considering the reservoir lifespan, i.e., the production still proceeds when the production temperature is lower than 120 °C.

4.3.2. Sensitivity analysis with respect to the impact of injection rate

This section investigates the reservoir performance for different injection rates, and presents the simulation results with 10.71 L/s and 24.99 L/s. Since the lifespans of the reservoirs using scCO₂ as the working fluid are larger than 30 years when the injection rate is 3.57 L/s, only the injection rates higher than 3.57 L/s are investigated.

Figure 4.9 presents the relationship between (a) production temperature and production time and (b) heat production rate and production time with the injection rate of 10.71 L/s between the combined scCO₂-H₂O, scCO₂-saturated, and H₂O-saturated EGS. Similar to the simulation results presented in **Figure 4.7(a)**, the production temperatures of the combined scCO₂-H₂O EGS and scCO₂-saturated EGS remain constant during the 30-year production, while the H₂O-saturated EGS drop sharply from the beginning of the production. Considering the definition of reservoir lifespan, the service time of the H₂O-saturated EGS is only approximately four years at the injection rate of 10.71 L/s, which is considerably shorter than that of the combined

scCO₂-H₂O and scCO₂-saturated EGS. On the other hand, due to the production temperature drop of H₂O-saturated EGS, its heat production rate also sharply reduces after the beginning of production. However, the heat production rate of the combined scCO₂-H₂O EGS remains constant after the initial decrease and exceeds that of the H₂O-saturated EGS at approximately year 6. Furthermore, the heat production rate of the H₂O-saturated EGS decreases even further than that of the scCO₂-saturated EGS, which indicates using scCO₂ as the working fluid shows better performance at a higher injection rate than H₂O.

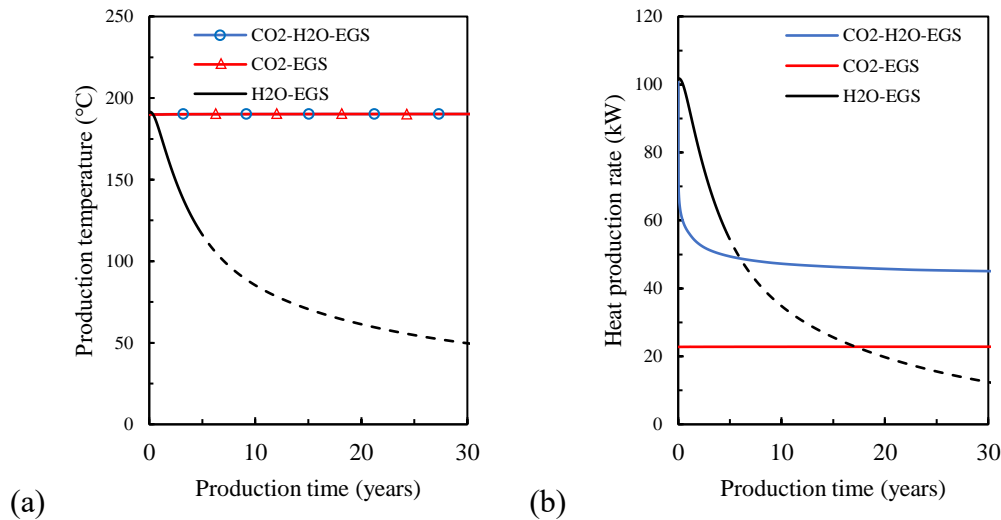


Figure 4.9. Relationship between (a) production temperature and (b) heat production rate and production rate at an injection rate of 10.71 L/s for the combined scCO₂-H₂O EGS, scCO₂-saturated EGS, and H₂O-saturated EGS. The black dashed line presents the results without considering the reservoir lifespan, i.e., the production still processes when the production temperature is lower than 120 °C.

Figure 4.10 presents the relationship between (a) production temperature and production time and (b) the heat production rate and production time with the injection rate of 24.99 L/s for the combined scCO₂-H₂O EGS, scCO₂-saturated EGS, and H₂O-saturated EGS. The combined scCO₂-H₂O EGS production temperatures and scCO₂-saturated EGS drop drastically in year 29, decreasing from 190 °C to 61 °C. Compared

to the production temperature of H₂O-saturated EGS, the variations of production temperature of scCO₂-saturated H₂O-saturated EGS and scCO₂-saturated EGS are much more abrupt. The discrepancy between scCO₂ and H₂O can be explained in **Figure 4.11**, which shows temperature distributions for the first arrival of the cold plume at the production well. When the H₂O cold plume reaches the production well, the rock matrix temperature near fractures is high, and H₂O heats up by the surrounding rock matrix. In contrast, when the scCO₂ cold plume arrives in the production well, the rock matrix near the fractures has already been cooled down, and the fracture fluid only received limited energy from the rock matrix. Thus, the production temperature shows a sharp drop at the breakthrough.

Figure 4.10(b) shows that at the injection rate of 24.99 L/s, the heat production rate of H₂O-saturated EGS rapidly decreases with time. In contrast, heat production rates of the combined scCO₂-H₂O EGS and scCO₂-saturated EGS remain constant during nearly the whole production period of 30 years. At the end of the simulation, the heat production rate of the combined scCO₂-H₂O EGS and scCO₂-saturated EGS show sharp drops resulting from decreases in production temperatures.

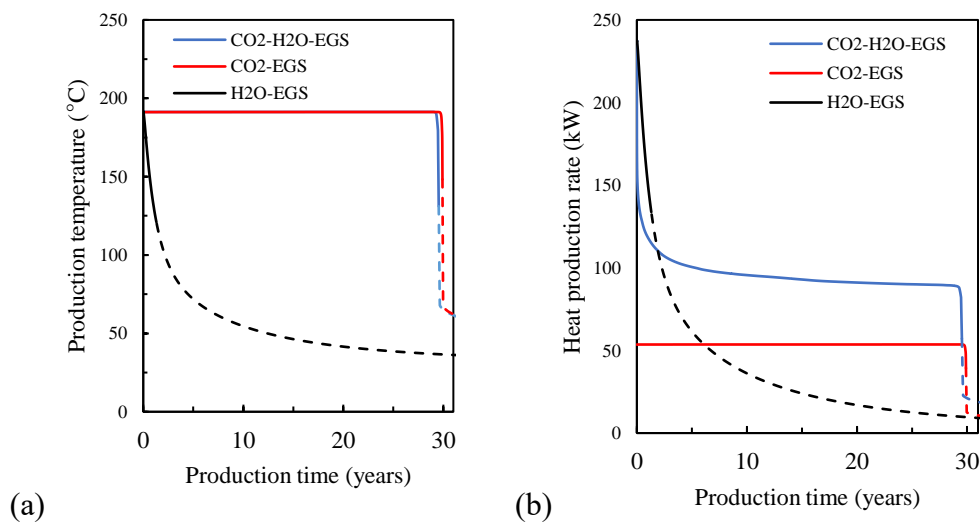


Figure 4.10. Relationship between (a) production temperature and production time and (b) heat production rate and the production rate for an injection rate of 24.99 L/s for the combined scCO₂-H₂O EGS, scCO₂-saturated EGS, and H₂O-saturated EGS setups. The dashed lines present the results without considering

the reservoir lifespan, i.e., the production still progresses even with production temperatures below 120 °C.

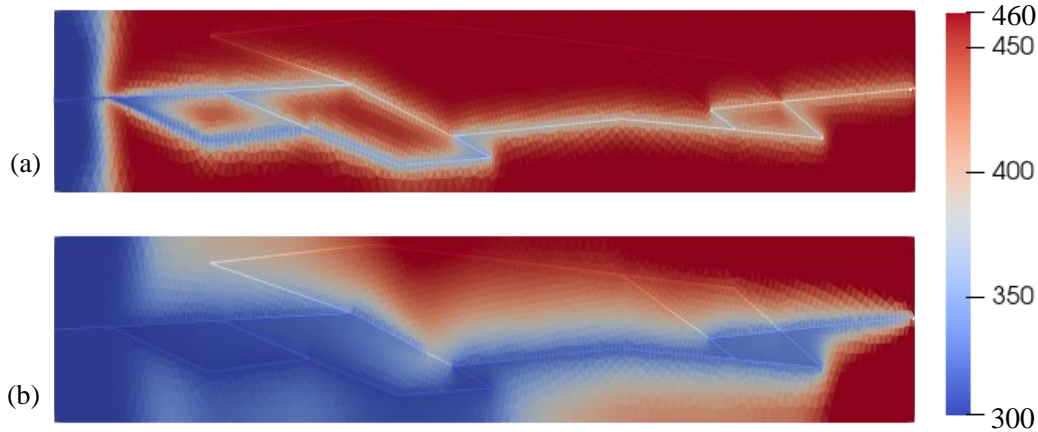


Figure 4.11. Temperature distribution when the cold plumes first arrive in the production well with (a) H₂O and (b) scCO₂ as the working fluids for an injection rate of 24.99 L/s.

Figure 4.12 presents the relationship between total produced thermal energy and production time for an injection rate of (a) 10.71 L/s and (b) 24.99 L/s. The scCO₂ working fluid leads to a much-improved performance compared with H₂O at high injection rates. The combined scCO₂-H₂O EGS and scCO₂-saturated EGS provide geothermal energy during the whole production period continuously and stably, while the heat production rate of the H₂O-saturated EGS generally decreases with continued production. Furthermore, for an injection rate of 10.71 L/s, concerning the total produced geothermal energy, the H₂O-saturated EGS still exceeds in performance compared to scCO₂-saturated EGS. In contrast, the total produced geothermal energy of the combined scCO₂-H₂O EGS exceeded that of H₂O-saturated EGS at approximately year 16. However, with the injection rate of 24.99 L/s, the better performance of H₂O-saturated EGS on scCO₂-saturated EGS ceases. The total geothermal energy produced by the scCO₂-saturated EGS and the combined scCO₂-H₂O EGS exceeded the energy produced by the H₂O-saturated EGS at approximately

year 19 and the start of production, i.e., year 5, respectively. Considering the reservoir lifespan, the lower performance of H₂O-saturated EGS is more prominent. With the injection rates of 10.71 L/s and 24.99 L/s, the H₂O-saturated EGS has the lowest total produced energy compared to the combined scCO₂-H₂O EGS and scCO₂-saturated EGS.

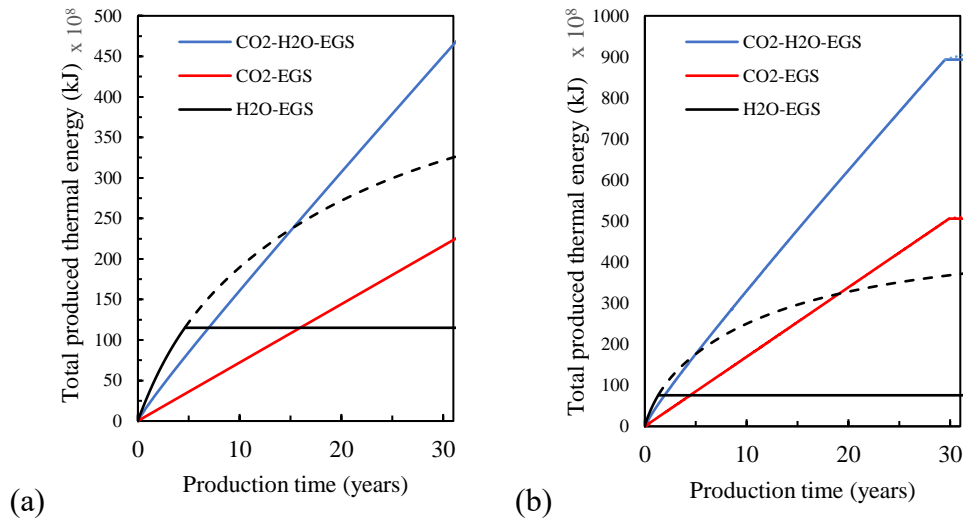


Figure 4.12. Relationship between total produced thermal energy and production time with injection rates of (a) 10.71 L/s and (b) 24.99 L/s. The black dashed line presents the results without considering the reservoir lifespan, i.e., production still continues even for production temperatures lower than 120 °C.

4.3.3. Effects of final cooldown production temperature on EGS performance

This work defines reservoir lifespan as the time for production temperature to decrease from 190 °C to 120 °C. Still, the geothermal energy from the produced fluid at temperatures lower than 120 °C can be exploited in district heating or binary powerplants [22], [23]. Thus, this section investigates the influence of the final cooldown production temperature on reservoir performance.

Figure 4.13 illustrates the relationship between (a) total produced thermal energy and injection rates of working fluids with different final cooldown production temperatures. The combined scCO₂-H₂O EGS and scCO₂-saturated EGS lifespans are nearly independent of the injection rate at higher injection rates. On the other hand, due to the

earlier cold plume breakthrough time at a higher injection rate, the reservoir lifespan of H₂O saturated EGS shows a sharp decrease with the increasing injection rate in cases where the final cooldown production temperature is higher than the injection temperature. The reservoir lifespan and total produced energy of scCO₂-saturated EGS and combined scCO₂- H₂O EGS remain unchanged with different final cooldown production temperatures, and their temperature development is not shown.

Figure 4.13(b) shows that the total thermal energy produced by combined scCO₂-H₂O EGS and scCO₂-saturated EGS increases considerably with increasing injection rate. In contrast, the output energy of H₂O saturated EGS depends on the final cooldown production temperature. For example, with the increasing injection rate, the final cooldown production temperature of 30 °C leads to a continuous increase in the total output energy. Still, the value of 120 °C results in an opposite performance, i.e., the total output energy presents a reduction with the increasing injection rate. For an injection rate of 3.57 L/s, the total produced thermal energy of H₂O-saturated EGS reduces from approximately 2.36×10^{10} kJ to 1.84×10^{10} kJ. On the other hand, the reductions of the total produced thermal energy for injection rates of 10.71 L/s and 24.99 L/s range from 3.28×10^{10} kJ to 1.15×10^{10} kJ and from 3.73×10^{10} kJ to 0.757×10^{10} kJ. Furthermore, the total thermal energy produced by the combined scCO₂-H₂O EGS and scCO₂-saturated EGS is considerably higher than that of H₂O-saturated EGS for an injection rate of 24.99 L/s, which indicates that reservoir performance applying scCO₂ as the working fluid is to be preferred compared to employing H₂O as working fluid at a high injection rate.

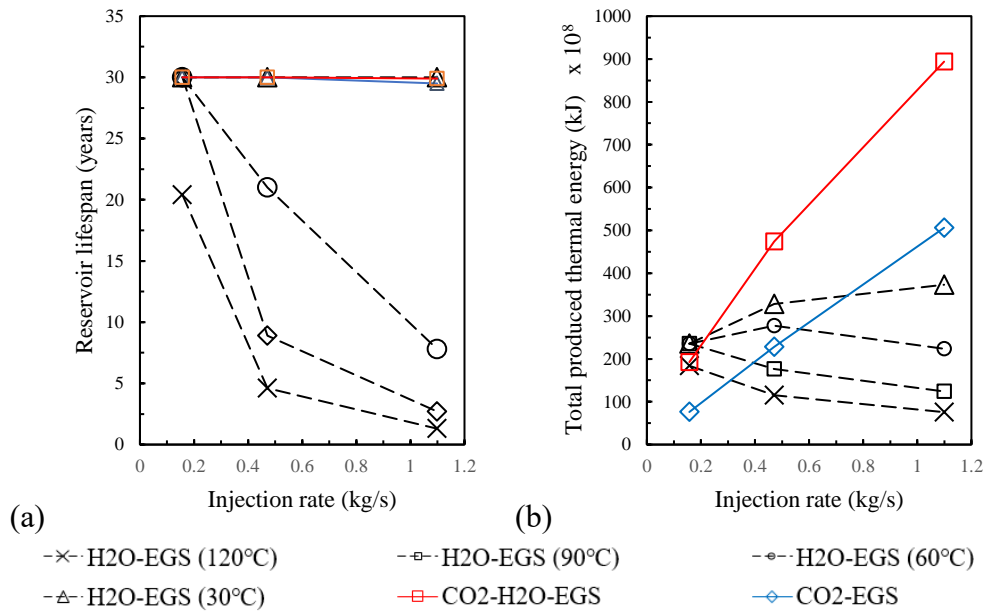


Figure 4.13. Relationship between reservoir lifespan and injection rate with different final cooldown production temperature, i.e., the period before the production temperature drops to specific values: 120 °C, 90 °C, 60 °C, and 30 °C.

4.6. Discussion and Conclusions

This study uses a lower-dimensional numerical model for non-isothermal two-phase flow in fractured porous media to simulate the fluid flow, phase displacement, and heat transport in EGS. The numerical model is implemented in the open-source simulator, DuMuX.

Brine (H₂O) and supercritical carbon dioxide (scCO₂) serve as working fluids for the heat circulation within the geothermal reservoirs. With these two working fluids, three types of EGSs are evaluated: 1) scCO₂-saturated EGS, where the fluid in the initially saturated reservoir and the injected working fluid are both scCO₂; 2) H₂O-saturated EGS, where the fluid in the initial saturated reservoir and the injected working fluid are both H₂O; 3) the combined scCO₂-H₂O EGS, where the fluid in the initially saturated reservoir is H₂O while the injected working fluid is scCO₂. Comparing the three types of EGS, the following conclusions can be drawn:

1. Temperature distributions of the combined scCO₂-H₂O EGS and scCO₂-saturated EGS are very similar but differ significantly from H₂O-saturated EGS. The cold plume

in the H₂O-saturated EGS migrates much faster than that of the combined scCO₂- H₂O EGS and scCO₂-saturated EGS. This is because the heat capacity of H₂O is approximately four times higher than that of scCO₂; for the same injection rate, the cold fluid of H₂O-saturated EGS needs considerably more geothermal energy to be heated to the same temperature compared to that of the combined scCO₂-H₂O EGS and scCO₂-saturated EGS.

2. For an injection rate of 3.57L/s, the production temperature of the reservoirs that use scCO₂ as the working fluid keeps at a constant level during the 30-year heat production, while the production temperature of the reservoir using H₂O as the working fluid starts to decrease from approximately year five onwards. Furthermore, the total produced thermal energy of scCO₂-saturated EGS is the lowest, while the H₂O-saturated EGS has the highest total produced thermal energy over the 30-year production period.

3. The injection rate highly affects heat production rates and production temperatures. With higher injection rates (10.71 L/s and 24.99 L/s), the total produced thermal energy and lifespan of H₂O-saturated EGS display sharp drops because of the decrease in production temperature. On the other hand, the reservoirs with scCO₂ as working fluid perform better at higher injection rates; the total produced geothermal energy shows a considerable increase while the reservoir lifespans are kept nearly unchanged.

4. The decrease in production temperature of the reservoirs with scCO₂ as working fluid is considerably more significant than that of H₂O-saturated EGS before the thermal breakthrough. In the combined scCO₂-H₂O EGS and scCO₂-saturated EGS, the rock matrix temperature adjacent to the fractures has already cooled down when the cold plume arrives at the production well, resulting in the cold fluid not being effectively heated. In contrast, the rock matrix still displays higher temperatures when the production temperature decreases. Thus, the reduction in the production temperature of H₂O-saturated EGS is much gentler.

In conclusion, the combined scCO₂-H₂O EGS shows the best performance among the three EGSs. At low injection rates, the combined scCO₂-H₂O EGS produces considerably more geothermal energy than reservoirs saturated by scCO₂. On the other

hand, the combined scCO₂-H₂O has a longer reservoir lifespan than the H₂O-saturated EGS. The combined scCO₂-H₂O EGS performs better at higher injection rates than H₂O-saturated EGS and CO₂-saturated EGS. Specifically, compared to H₂O-saturated EGS, the combined scCO₂-H₂O EGS shows considerably higher heat production rates and a longer reservoir lifespan. On the other hand, the reservoir lifespans of the combined scCO₂-H₂O EGS and scCO₂-saturated EGS are the same, but the heat production rate of the combined scCO₂-H₂O EGS is much higher than that of scCO₂-saturated EGS.

Nomenclature			
Governing Equations		n	VG coefficient
ϕ	porosity	\mathbf{g}	Gravity
α	phase index	ρ_s	Rock density
S_α	Saturation	ρ_α	Phase density
S_{we}	Effective saturation	c_s	Rock heat capacity
S_{wr}	Residual saturation	h_α	Phase enthalpies
\mathbf{K}	Permeability	α_T	Thermal expansion coefficient
$k_{r\alpha}$	Relative permeability	λ	Thermal conductivity of rocks
q_α	Flux source and sink	a	Fracture aperture
q_h	Energy source and sink		
\mathbf{v}_α	Fluid velocity	Performance	
μ_α	Fluid viscosity	T_o	Production temperature
p_α	Phase pressure	Q_f	Flux from fracture
p_c	Capillary pressure	Q_s	Flux from rock matrix
p_e	Air entry pressure	$P(t)$	Heat production rate
m	VG coefficient	E_{total}	Cumulative produced energy

4.7. Acknowledgment

We acknowledge the financial support for Deijan Zhou from the China scholarship council (CSC).

4.8. References

- [1] M. Z. Jacobson, M. A. Delucchi, M. A. Cameron, and B. V. Mathiesen, "Matching demand with supply at low cost in 139 countries among 20 world regions with 100%

- intermittent wind, water, and sunlight (WWS) for all purposes," *Renew. Energy*, vol. 123, pp. 236–248, Aug. 2018, doi: 10.1016/j.renene.2018.02.009.
- [2] S. Teske, Ed., *Achieving the Paris Climate Agreement Goals: Global and Regional 100% Renewable Energy Scenarios with Non-energy GHG Pathways for +1.5°C and +2°C*. Cham: Springer International Publishing, 2019. doi: 10.1007/978-3-030-05843-2.
- [3] M. Huang, Y. Jiao, J. Luo, C. Yan, L. Wu, and P. Guan, "Numerical investigation on heat extraction performance of an enhanced geothermal system with supercritical N₂O as working fluid," *Appl. Therm. Eng.*, vol. 176, p. 115436, Jul. 2020, doi: 10.1016/j.applthermaleng.2020.115436.
- [4] F. Gong *et al.*, "Evaluation of geothermal energy extraction in Enhanced Geothermal System (EGS) with multiple fracturing horizontal wells (MFHW)," *Renew. Energy*, vol. 151, pp. 1339–1351, May 2020, doi: 10.1016/j.renene.2019.11.134.
- [5] C. R. Chamorro, J. L. García-Cuesta, M. E. Mondéjar, and A. Pérez-Madrado, "Enhanced geothermal systems in Europe: An estimation and comparison of the technical and sustainable potentials," *Energy*, vol. 65, pp. 250–263, Feb. 2014, doi: 10.1016/j.energy.2013.11.078.
- [6] F. H. Cocks, *Energy Demand and Climate Change: Issues and Resolutions*, 1st ed. Wiley, 2009. doi: 10.1002/9783527627035.
- [7] S.-M. Lu, "A global review of enhanced geothermal system (EGS)," *Renew. Sustain. Energy Rev.*, vol. 81, pp. 2902–2921, Jan. 2018, doi: 10.1016/j.rser.2017.06.097.
- [8] K. Pruess, "Enhanced geothermal systems (EGS) using CO₂ as working fluid—A novel approach for generating renewable energy with simultaneous sequestration of carbon," *Geothermics*, vol. 35, no. 4, pp. 351–367, Aug. 2006, doi: 10.1016/j.geothermics.2006.08.002.
- [9] K. Pruess, On the production behavior of enhanced geothermal systems with CO₂ as working fluid. Lawrence Berkeley National Laboratory. Retrieved from <https://escholarship.org/uc/item/6xf1m956>, 2008.
- [10] T. R. Elliot, T. A. Buscheck, and M. Celia, "Active CO₂ reservoir management for sustainable geothermal energy extraction and reduced leakage," *Greenh. Gases Sci. Technol.*, vol. 3, no. 1, pp. 50–65, Feb. 2013, doi: 10.1002/ghg.1328.
- [11] M. R. Fleming, B. Adams, and M. O. Saar, "Using Sequestered CO₂ as Geothermal Working Fluid to Generate Electricity and Store Energy," 2020, doi: 10.3929/ETHZ-B-000449690.
- [12] O. Kolditz *et al.*, "A systematic benchmarking approach for geologic CO₂ injection and storage," *Environ. Earth Sci.*, vol. 67, no. 2, pp. 613–632, Sep. 2012, doi: 10.1007/s12665-012-1656-5.
- [13] E. R. Okoroafor, M. J. Williams, J. Gossuin, O. Jimoh-Kenshiro, and R. N. Horne, "Comparison of EGS Thermal Performance with CO₂ and Water as Working Fluids," Stanford University, Stanford, California, Feb 15-17, 2021.
- [14] T. Guo, F. Gong, X. Wang, Q. Lin, Z. Qu, and W. Zhang, "Performance of enhanced geothermal system (EGS) in fractured geothermal reservoirs with CO₂

- as working fluid," *Appl. Therm. Eng.*, vol. 152, pp. 215–230, Apr. 2019, doi: 10.1016/j.applthermaleng.2019.02.024.
- [15] J. Li *et al.*, "Investigations of heat extraction for water and CO₂ flow based on the rough-walled discrete fracture network," *Energy*, vol. 189, p. 116184, Dec. 2019, doi: 10.1016/j.energy.2019.116184.
- [16] C.-L. Wang, W.-L. Cheng, Y.-L. Nian, L. Yang, B.-B. Han, and M.-H. Liu, "Simulation of heat extraction from CO₂-based enhanced geothermal systems considering CO₂ sequestration," *Energy*, vol. 142, pp. 157–167, Jan. 2018, doi: 10.1016/j.energy.2017.09.139.
- [17] A. Borgia, K. Pruess, T. J. Kneafsey, C. M. Oldenburg, and L. Pan, "Simulation of CO₂-EGS in a Fractured Reservoir with Salt Precipitation," *Energy Procedia*, vol. 37, pp. 6617–6624, 2013, doi: 10.1016/j.egypro.2013.06.594.
- [18] A. Borgia *et al.*, "Simulations of CO₂ injection into fractures and faults for improving their geophysical characterization at EGS sites," *Geothermics*, vol. 69, pp. 189–201, Sep. 2017, doi: 10.1016/j.geothermics.2017.05.002.
- [19] J. Liao *et al.*, "Field scale numerical modeling of heat extraction in geothermal reservoir based on fracture network creation with supercritical CO₂ as working fluid," *Environ. Earth Sci.*, vol. 79, no. 12, p. 291, Jun. 2020, doi: 10.1007/s12665-020-09001-7.
- [20] B. Guo, P. Fu, Y. Hao, C. A. Peters, and C. R. Carrigan, "Thermal drawdown-induced flow channeling in a single fracture in EGS," *Geothermics*, vol. 61, pp. 46–62, May 2016, doi: 10.1016/j.geothermics.2016.01.004.
- [21] Z. Su and H. Zhai, Evaluation of Heat Production from Single Fracture Hot Dry Rock with Applications for EGS Reservoir Design. Available at SSRN: <https://ssrn.com/abstract=3895685> or <http://dx.doi.org/10.2139/ssrn.3895685>
- [22] L. Liu, T. Zhu, N. Gao, and Z. Gan, "A Review of Modeling Approaches and Tools for the Off-design Simulation of Organic Rankine Cycle," *J. Therm. Sci.*, vol. 27, no. 4, pp. 305–320, Aug. 2018, doi: 10.1007/s11630-018-1023-2.
- [23] K. Salhi, M. Korichi, and K. M. Ramadan, "Thermodynamic and thermo-economic analysis of compression–absorption cascade refrigeration system using low-GWP HFO refrigerant powered by geothermal energy," *Int. J. Refrig.*, vol. 94, pp. 214–229, Oct. 2018, doi: 10.1016/j.ijrefrig.2018.03.017.
- [24] T. Wang, Z. Sun, K. Zhang, C. Jiang, Y. Xin, and Q. Mao, "Investigation on Heat Extraction Performance of Fractured Geothermal Reservoir Using Coupled Thermal-Hydraulic-Mechanical Model Based on Equivalent Continuum Method," *Energies*, vol. 12, no. 1, p. 127, Dec. 2018, doi: 10.3390/en12010127.
- [25] B. Figueiredo, C.-F. Tsang, and A. Niemi, "The Influence of Coupled Thermomechanical Processes on the Pressure and Temperature due to Cold Water Injection into Multiple Fracture Zones in Deep Rock Formation," *Geofluids*, vol. 2020, pp. 1–14, Jan. 2020, doi: 10.1155/2020/8947258.
- [26] D. Zhou, A. Tatomir, and M. Sauter, "Thermo-hydro-mechanical modelling study of heat extraction and flow processes in enhanced geothermal systems," *Adv. Geosci.*, vol. 54, pp. 229–240, Jun. 2021, doi: 10.5194/adgeo-54-229-2021.
- [27] A.-B. Tatomir, *From discrete to continuum concepts of flow in fractured porous*

- media*. Stuttgart: Inst. für Wasser- und Umweltsystemmodellierung, 2012.
- [28] P. Dietrich, R. Helmig, M. Sauter, H. Hötzl, J. Köngeter, and G. Teutsch, *Flow and transport in fractured porous media*. Berlin ; New York: Springer, 2005.
- [29] D. Gläser *et al.*, "An Approach Towards a FEP-based Model for Risk Assessment for Hydraulic Fracturing Operations," *Energy Procedia*, vol. 97, pp. 387–394, Nov. 2016, doi: 10.1016/j.egypro.2016.10.030.
- [30] D. Zhou, A. Tatomir, A. Niemi, C.-F. Tsang, and M. Sauter, "Study of Fracture Aperture Variation in a Fracture Network on Heat Production from an Enhanced Geothermal System (EGS)," *SSRN Electron. J.*, 2021, doi: 10.2139/ssrn.3918922.
- [31] T. Koch *et al.*, "DuMux 3 – an open-source simulator for solving flow and transport problems in porous media with a focus on model coupling," *Comput. Math. Appl.*, vol. 81, pp. 423–443, Jan. 2021, doi: 10.1016/j.camwa.2020.02.012.
- [32] B. Flemisch *et al.*, "DuMux: DUNE for multi- $\{\text{phase, component, scale, physics, \dots}\}$ flow and transport in porous media," *Adv. Water Resour.*, vol. 34, no. 9, pp. 1102–1112, Sep. 2011, doi: 10.1016/j.advwatres.2011.03.007.
- [33] J. P. Kaszuba, L. L. Williams, D. R. Janecky, W. K. Hollis, and I. N. Tsimpanogiannis, "Immiscible CO_2 - H_2O fluids in the shallow crust: CRUSTAL CO_2 - H_2O FLUIDS," *Geochem. Geophys. Geosystems*, vol. 7, no. 10, p. n/a-n/a, Oct. 2006, doi: 10.1029/2005GC001107.
- [34] M. Th. van Genuchten, "A Closed-form Equation for Predicting the Hydraulic Conductivity of Unsaturated Soils," *Soil Sci. Soc. Am. J.*, vol. 44, no. 5, pp. 892–898, Sep. 1980, doi: 10.2136/sssaj1980.03615995004400050002x.
- [35] T. A. Davis, "Algorithm 832: UMFPACK V4.3---an unsymmetric-pattern multifrontal method," *ACM Trans. Math. Softw.*, vol. 30, no. 2, pp. 196–199, Jun. 2004, doi: 10.1145/992200.992206.
- [36] D. Gläser, B. Flemisch, R. Helmig, and H. Class, "A hybrid-dimensional discrete fracture model for non-isothermal two-phase flow in fractured porous media," *GEM - Int. J. Geomath.*, vol. 10, no. 1, p. 5, Dec. 2019, doi: 10.1007/s13137-019-0116-8.
- [37] D. Gläser, R. Helmig, B. Flemisch, and H. Class, "A discrete fracture model for two-phase flow in fractured porous media," *Adv. Water Resour.*, vol. 110, pp. 335–348, Dec. 2017, doi: 10.1016/j.advwatres.2017.10.031.
- [38] J. Rutqvist, J. Noorishad, C.-F. Tsang, and O. Stephansson, "Determination of fracture storativity in hard rocks using high-pressure injection testing," *Water Resour. Res.*, vol. 34, no. 10, pp. 2551–2560, Oct. 1998, doi: 10.1029/98WR01863.
- [39] Z. Sun, "Numerical simulation of the heat extraction in EGS with thermal-hydraulic-mechanical coupling method based on discrete fractures model," *Energy*, vol. 120, pp. 20–33, 2017, doi: <https://doi.org/10.1016/j.energy.2016.10.046>.
- [40] C. Darcel, P. Davy, R. Le Goc, J.R. de Dreuzy, and O. Bour, *Statistical methodology for discrete fracture model - including fracture size, orientation uncertainty together with intensity uncertainty and variability*. Sweden: N. p., 2009. Web.
- [41] A. Fox, P. La Pointe, A. Simeonov, J. Hermanson, and J. Oehman. *Statistical geological discrete fracture network model. Forsmark modelling stage 2.2*.

- Sweden: N. p., 2007. Web.
- [42] R, Alain and J. E. Gale. "Statistical characterization of the fracture system in the Stripa granite, Sweden." *International Journal of Rock Mechanics and Mining Sciences & Geomechanics Abstracts* 22 (1985): 353-367.
- [43] E, Hakami. Aperture distribution of rock fractures (KTH-AMI-PHD--1003). Sweden, 1995.
- [44] S. P. Bertels, D. A. DiCarlo, and M. J. Blunt, "Measurement of aperture distribution, capillary pressure, relative permeability, and in situ saturation in a rock fracture using computed tomography scanning," *Water Resour. Res.*, vol. 37, no. 3, pp. 649–662, Mar. 2001, doi: 10.1029/2000WR900316.
- [45] A. Assteerawatt, *Flow and transport modelling of fractured aquifers based on a geostatistical approach*. 2008. Accessed: Jun. 17, 2021. [Online]. Available: <https://nbn-resolving.org/urn:nbn:de:bsz:93-opus-36392>
- [46] J. Gong and W. R. Rossen, "Modeling Flow in Naturally Fractured Reservoirs: Effect of Fracture Aperture Distribution on Critical Sub-Network for Flow," DFNE 2014: Proceedings of the 1st International Conference on Discrete Fracture Network Engineering, Vancouver, Canada, 19-22 October 2014
- [47] International Association for the Properties of Water and Steam, R7-97: Advisory Note No. 6: Revised Release on the IAPWS Industrial Formulation 1997 for the Thermodynamic Properties of Water and Steam (The revision only relates to the extension of region 5 to 50 MPa), (2012).
- [48] R. Span and W. Wagner, "A New Equation of State for Carbon Dioxide Covering the Fluid Region from the Triple-Point Temperature to 1100 K at Pressures up to 800 MPa," *J. Phys. Chem. Ref. Data*, vol. 25, no. 6, pp. 1509–1596, Nov. 1996, doi: 10.1063/1.555991.
- [49] C. Geuzaine and J.-F. Remacle, "Gmsh: A 3-D finite element mesh generator with built-in pre- and post-processing facilities: THE GMSH PAPER," *Int. J. Numer. Methods Eng.*, vol. 79, no. 11, pp. 1309–1331, Sep. 2009, doi: 10.1002/nme.2579.

Chapter. 5

Effects of Heterogeneous Fracture Permeability on the Performances of an Enhanced Geothermal System

Dejian Zhou^{1,*}, Alexandru Tatomir¹, Huhao Gao¹, Martin Sauter¹

¹ Department of Applied Geology, University of Göttingen, 37077, Göttingen, Germany

* Corresponding author. Email: dejian.zhou@geo.uni-goettingen.de

Citation:

Zhou, D., etc.,

Effects of Heterogeneous Fracture Permeability on the Performances of an Enhanced Geothermal System

In Preparation

To be submitted to Applied Energy

Abstract

With the development of Enhanced Geothermal System (EGS) technology, the application of deep geothermal energy has become increasingly attractive. An EGS reservoir is usually formed by a single fracture or a fracture network in which preferential flow plays an essential role in reservoir performance. Considering the buoyancy force of the scCO₂ within the H₂O saturated reservoir, the effects of heterogeneous permeability may be very different in the two-phase system compared to a single-phase system. This work is employing Monte Carlo method to investigate the influence of a heterogeneous permeability field on the performance of the EGS reservoir with a single fracture. The results show that the preferential flow pathway generated by the heterogeneous permeability significantly increases the scCO₂ velocity toward the production well during the initial production period, such that the breakthroughs of scCO₂ and temperature at production well are advanced. However, preferential flow pathways lead to a worse long-term energy performance. On the other hand, the total sequestered scCO₂ mass presents a slight reduction within the heterogeneous permeability field compared to the homogeneous field. Furthermore, the reservoir using scCO₂ as working fluid has a much better energy performance than the reservoir whose working fluid is H₂O.

5.1. Introduction

Geothermal energy is becoming increasingly attractive with the development of the new

technology of Enhanced Geothermal System (EGS). According to the theoretical calculation, the current geothermal energy estimated could provide more than 200-million-year support for human civilization's energy demand [1]–[4]. An EGS is created in crystalline formations by generating new fractures or enhancing the existing the natural fractures [5], [6]. Thus, the working fluid within EGS reservoirs circulates through a single fracture or through a fracture network. Due to the considerable differences between fractures and the surrounding rock matrix, in which the fracture has a significant higher permeability than rock matrix, the fractures form the primary flow pathway for the working fluid movement, which determine the EGS reservoir performance, such as the production temperature and energy production rate. Therefore, understanding how fracture properties impact the working fluid flow is of key importance.

Variations in the distribution of fracture apertures (which in practice correspond to variations in fracture permeabilities) are ubiquitous in natural fracture networks [7], [8]. Generally, preferential flow pathways are formed by the connection of higher permeability regions within the single fracture, in which the working fluid circulation time is shorter. As a result, the heating time for the cold working fluid is shorter and the temperature presents an earlier breakthrough in the production well. On the other hand, the heat production rate also varies under the combined effects of fluid flow rate and production temperature.

Many researchers have made contributions to the investigation of fracture heterogeneity.

Zhou et al. (2022) proposed a novel concept, i.e., partial-raster element, to simulate the

aperture distribution of the fracture networks with different fracture densities. The results of numerical simulations using Monte Carlo method indicate that a heterogeneous aperture field leads to a reduction in the average heat production rate and the production temperature over a long-term period (i.e., 30 years). On the other hand, increased mean apertures of the existing fractures have a more substantial effect on increasing reservoir heat production rate than creating new fractures [5]. Based on the high-temperature reservoir in the Guide basin, Zhang et al. (2021) established a three-dimensional thermal-hydraulic-mechanical coupled model to explore the influence of reservoir heterogeneity on the extraction ability. It was found that the reservoir specific heat capacity variation has a negligible impact on reservoir performance, while the spatially heterogeneous permeability field has much more significant effects due to the creation of preferential flow path in unevenly distributed permeability field [9]. Fox et al. (2015) generated a heterogeneous aperture field and obtained that when the fracture network field has a low standard deviation, the average aperture has more considerable effects on reservoir energy performance compared to the high value of aperture standard deviation. On the other hand, provided that the injection rate is fixed, the reservoir with a larger number of fractures performs better because the dispersed flow rate within each fracture delays the temperature breakthrough extending the reservoir lifespan [10].

However, up to now, most studies on reservoir preferential flow pathway investigated primarily water-based EGS. The study on the EGS with other working fluids, e.g., supercritical carbon dioxide (scCO₂), is rare. Since 2006, when employing scCO₂ as

EGS working fluid was firstly proposed, the possibility of CO₂-based EGS has been widely discussed [11]–[15]. scCO₂ shows several advantages over H₂O as a reservoir working fluid: 1) the lower viscosity requires lower pressure to circulate scCO₂ within EGS reservoir; and 2) the sequestered scCO₂ benefits the reduction of greenhouse gas in the atmosphere. The studies on CO₂-based EGS usually ignore the fracture heterogeneity, i.e., the aperture/permeability is assumed to be homogeneously distributed in the fracture network. For example, using TOUGH2 numerical simulator for a two-phase flow model, Borgia et al. [13], [16] concluded that the actual heat flow rate of combined scCO₂-H₂O EGS could be up to five times larger than the heat flow rate achievable with water as a working fluid. Nevertheless, they did not consider the heterogeneity of fracture aperture and permeability.

Because of the existing buoyancy force of the scCO₂ within a H₂O saturated EGS reservoirs, the scCO₂ migration direction is not only determined by preferential flow pathways but also by the buoyancy force. In this case, combined effects of the buoyancy force and preferential flow pathways on the reservoir performance need to be further investigated.

This study, based on an the open-source research software, DuMu^X, develops a two-dimensional (2D) two-phase thermal-hydraulic (2pTH) model to investigate the influences of preferential flow pathways within heterogeneous permeability field on the EGS reservoir performances, i.e., the production scCO₂ saturation, production temperature, cumulative produced energy, and sequestered scCO₂ mass. The EGS reservoir is formed by a single vertical fracture, and the permeability is randomly

distributed over the fracture following a Gaussian distribution. The geo-statistical R package, Gstat, is employed to generate the permeability field. The correlation length (CL) and standard deviation (STD) of the Gaussian distribution are the primary variables controlling permeability distribution and are being investigated in this study. Furthermore, the Monte Carlo method is applied to ensure the simulation results reach to statistical equilibrium over one hundred and fifty realizations for each CL-STD combination. Finally, the performances of the reservoirs using scCO₂ and H₂O as working fluids are compared.

5.2. Methodology

5.2.1 Mathematical and numerical model

The two-phase flow model with fully coupled hydraulic-thermal processes, which describes the flow of scCO₂ and H₂O in the EGS reservoir, is implemented in an open-source research simulator, DuMu^X, which focus on the transport problems in fractured porous media. This work assumes the 1) water and scCO₂ are immiscible and water does not evaporate during the whole production period; and 2) parameters for water retention curve and relative permeability are independent of the fracture permeability.

The mass balance equation of the fluid phase α in a fractured porous medium is:

$$\phi \frac{\partial(\rho_{\alpha} S_{\alpha})}{\partial t} + \nabla \cdot (\rho_{\alpha} \mathbf{v}_{\alpha}) + q_{\alpha} = 0, \quad \alpha \in \{w, n\} \quad (1)$$

where ϕ is the porosity of rock matrix which remains constant, ρ_{α} is the density of phase α , t is time, S_{α} is the phase saturation, \mathbf{v}_{α} is the fluid phase flow velocity,

and q_α is the source or sink term, the subscript α denotes the phase index, w and n refer to the wetting, i.e., water, and non-wetting phases, i.e., scCO₂. Darcy's law expresses the fluid phase flow velocity through the porous media:

$$\mathbf{v}_\alpha = -\frac{k_{r\alpha}}{\mu_\alpha} \bar{\mathbf{K}}(\nabla p_\alpha + \rho_\alpha \mathbf{g}) \quad (2)$$

where $\bar{\mathbf{K}}$ is the intrinsic permeability tensor of the rock matrix, the heterogeneous permeability field is employed in this work and a detailed description is given in section 2.3, μ_α is the fluid phase dynamic viscosity, $k_{r\alpha}$ is the relative permeability, p_α is the phase pressure, and \mathbf{g} is the gravitational acceleration. The phase saturation and pressure satisfied the relationships:

$$S_n + S_w = 1 \quad (3)$$

$$p_n = p_w + p_c \quad (4)$$

in which the p_c is the capillary pressure. The capillary pressure relationship with water saturation can be described by the van Genuchten equation [17]:

$$S_{we} = S_{wr} + \frac{1}{[1+(p_c/p_e)^n]^{1-1/n}} \quad (5)$$

where p_e is the air entry pressure, n is an index of the pore-size distribution, and S_{wr} is the residual wetting-phase saturation.

In a representative elementary volume is assumed local thermodynamic equilibrium.

The thermal energy balance equations is written as:

$$\phi \sum_\alpha \frac{\partial \rho_\alpha S_\alpha u_\alpha}{\partial t} + (1 - \phi) \frac{\partial \rho_s c_s T}{\partial t} + \nabla \cdot (\sum_\alpha \rho_\alpha h_\alpha \mathbf{v}_\alpha - \lambda \nabla T) = q_h \quad (6)$$

where T is the temperature, u_α and h_α are phase-specific internal energies and enthalpies, ρ_s and c_s are the density and the heat capacity of rock matrix, and q_h is

the heat flux at the source point.

The space is discretized by a cell-centered finite volume method employing the two-point flux approach and the temporal discretization uses the implicit Euler scheme [18].

For solving the non-linear system of equations, the Newton-Raphson method is applied together with the direct solver UMFPack [19].

5.2.2 Parameters for assessing the geothermal reservoir performance

The performances of the simulated geothermal reservoir are evaluated with production temperature, production scCO₂ saturation, heat production rate, and sequestered scCO₂ mass, which are defined as following [5], [20]–[22]:

(i) Production temperature (T_{out} [°C]) is calculated according to:

$$T_{\text{out}} = \frac{\sum_{i=1}^{\text{np}} T_{\text{out},i}}{\text{np}} \quad (7)$$

where $T_{\text{out},i}$ [K] is the temperature of production element i , np is the number of elements in the production well.

(ii) Production scCO₂ saturation (S_n [1]):

$$S_n = \frac{V_{\text{scCO}_2}}{V_{\text{H}_2\text{O}} + V_{\text{scCO}_2}} \quad (8)$$

where V_{scCO_2} is the volume of output scCO₂, $V_{\text{H}_2\text{O}}$ is the volume of output H₂O.

(iii) Cumulative produced energy (E_c [MW]):

$$E_c = \int_0^{t_{\text{end}}} \sum_{\alpha} M_{\alpha} E_{\alpha} \quad (9)$$

where E_{α} is the enthalpy of phase α , t_{end} is the production time, M_{α} is the production rate of phase α , which can be calculated as:

$$M_{\alpha}(t) = \int v_{\alpha} dA \quad (10)$$

where v_{α} is the flow velocity of phase α and A is the production area.

(iv) Sequestered scCO₂ mass (M_{CO_2} [Mt]):

$$M_{\text{CO}_2} = \sum_1^{nt} S_{n,i} V_{\text{element}} \quad (11)$$

where V_{element} is the element volume, nt is total number of elements in the domain.

(v) Monte Carlo results: in this work, all the reservoir performances are deal with Monte Carlo method. The detailed description is in section 2.4.

$$R_{\text{mc}}(t) = \frac{\sum_1^{nr} R_{\text{mc},i}(t)}{nr} \quad (12)$$

where $R_{\text{mc}}(t)$ is the reservoir performance calculated by Monte Carlo method, $R_{\text{mc},i}(t)$ is the reservoir performance of realization i at time check point, nr is the number of realizations. The reservoir performances include S_n , T_{out} , M_{α} , E_c , and M_{CO_2} .

(vi) Energy variation (V_E) is calculated as follows:

$$V_E = \frac{(E_{\text{Het}} - E_{\text{Hom}})}{E_{\text{Hom}}} \times 100 \quad (13)$$

where E_{Het} and E_{Hom} are the energy output from the cases with hetero- and homogeneous permeability fields, respectively.

5.2.3 Problem definition

The geothermal reservoir consists of a vertical distributed conductive fracture, whose permeability is significantly higher than the surrounding rock matrix. Therefore, the system is assumed to be a two-dimensional (2D) domain, which is located 2500m underground with a domain size of 600m × 100m. H₂O is initially saturating the geothermal reservoir before the injection of scCO₂. The scCO₂ is injected into the reservoir from the left boundary ranging between 0m and 20m, and produced from the

right boundary ranging between 80m and 100m. The injection temperature is kept at 30 °C. The overpressure at the injection well and production well are set as 0.1 MPa. Except for the areas of injection and production, which is set as Dirichlet boundary, the remaining boundaries are closed to heat and fluid flow as presented in **Figure 5.1**. To avoid the boundary effects, i.e., the fixed non-wetting phase saturation and production pressure, the data of production area is collected from the observation line, which is located 20m away from the right boundary.

The initial pressure distribution in the simulated geothermal reservoir results from the hydrostatic pressure (9.81 MPa/km) and the atmospheric pressure (0.1 MPa). The reservoir thermal gradient is 0.03°C/m with a temperature of 141.15 °C at the top of reservoir. The physical properties of H₂O and scCO₂ are obtained from the International Association for the Properties of Water and Steam (IAPWS) [23] and Span and Wagner (1996) [24]. The primary parameters employed are summarized in **Table 5.1**.

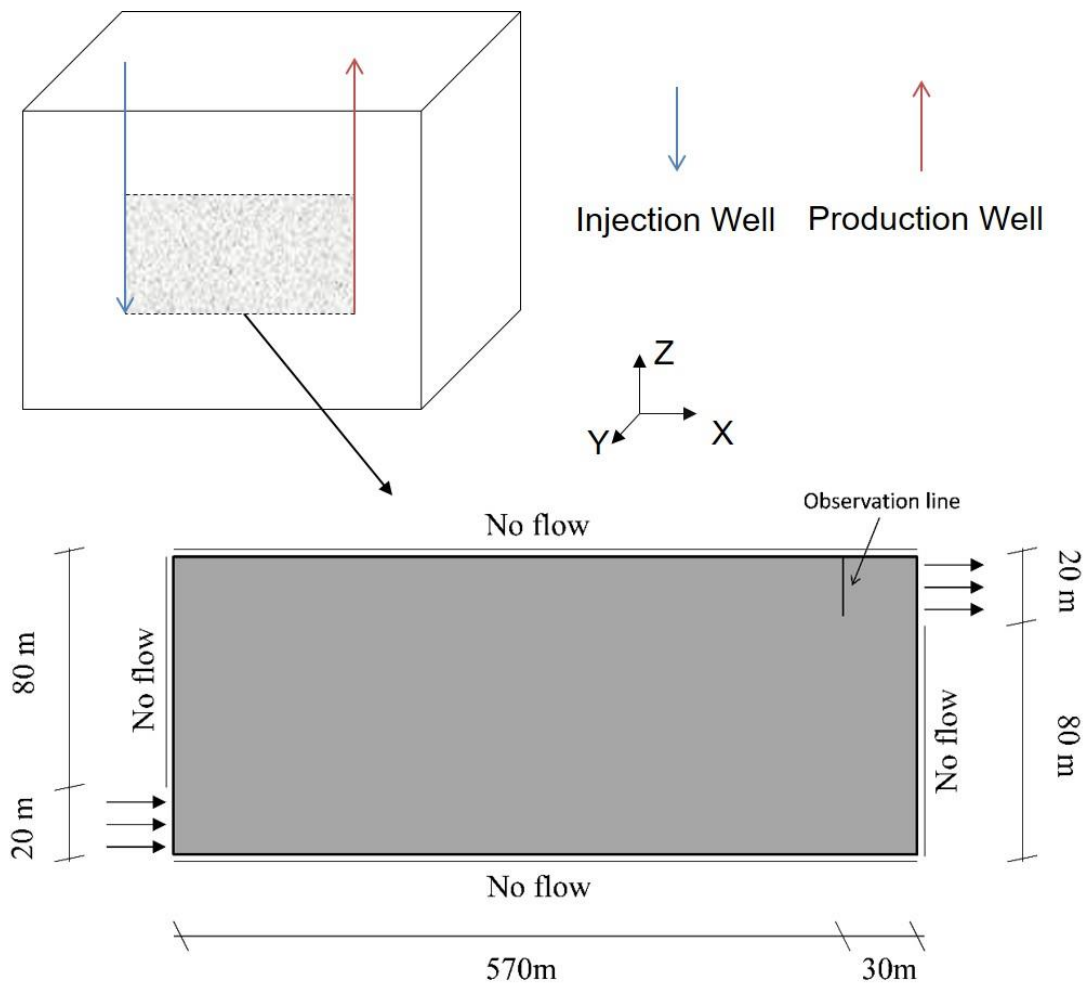


Figure 5.1. Illustration of the modelled domain and boundary conditions

Table 5.1. Parameter values for modelling of the geothermal system

Parameters	value
Rock density (kg/m^3)	2700
Permeability of rock matrix (m^2)	1×10^{-12}
Porosity (-)	0.3
Heat capacity of rocks ($\text{J/kg/}^\circ\text{C}$)	790
Thermal conductivity of rocks ($\text{W/m/}^\circ\text{C}$)	2.8
Thermal expansion coefficient (brine) ($1/^\circ\text{C}$)	10^{-4}

Thermal expansion coefficient (scCO ₂) (1/°C)	10 ⁻⁵
Van Genuchten coefficient n (-)	3
Residual wetting phase saturation (-)	0
Air entry pressure (Pa)	1000
Initial brine salinity (-)	0.2

5.2.4 Heterogeneous distribution of fracture permeability

The fracture permeability can be statistically represented by a randomly distributed permeability field, e.g., [25]–[27] and follows gamma or Gauss distribution with a given stress field (see [5], [27]–[29]). In this study, the R package Gstat, is employed to generate the heterogeneous permeability distribution [30], [31]. Gauss distribution is employed to describe the distributions of fracture aperture and permeability. The correlation length and standard deviation of the permeability are the primary variables determining the permeability distributions. The correlation length is defined as the distance within which the semi-variance, i.e., the statistical variance minus the permeability covariance, changes significantly with the distance variation between two locations [27]. As presented in **Figure 5.2**, the fracture permeability shows a broader range with a higher standard deviation, while the area with a similar permeability becomes larger under a more significant correlation length. In fractured porous media, the scCO₂ movement is significantly related to fracture permeability; and scCO₂ prefers to flow toward the high permeable area. Therefore, the different permeability distributions result in various preferential flow pathway of scCO₂ within H₂O.

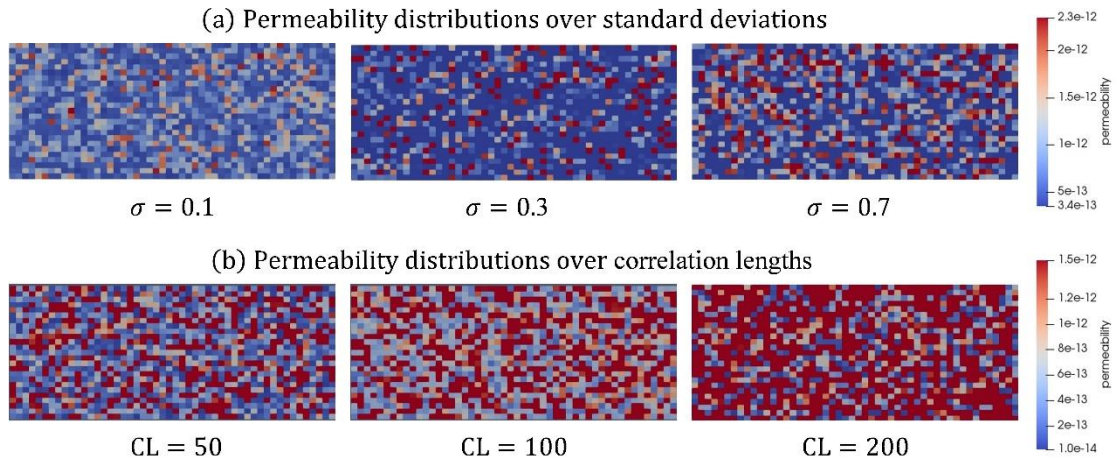


Figure 5.2. Examples of fracture permeability distributions over the change of (a) standard deviations (correlation length is 50), and (b) correlation lengths (standard deviation is 0.5).

5.2.5 Monte Carlo Method

Since the correlation length (CL) and the standard deviation (STD) determine the distribution of fracture permeability, different combinations of correlation lengths CL, and standard deviations STD, are investigated. Within each combination, the reservoir permeabilities are randomly distributed, forming various realizations, of which the statistic properties, i.e., correlation length, standard deviation, and average permeability are the same. Monte Carlo method is applied such that a significant number of realizations (i.e., at least 150) is simulated to obtain the statistical equilibrium of each combination, removing the serendipity from the random distribution. **Figure 5.3** presents the relationship between cumulatively produced energy (E_c) and the number of realizations. The realization number is 150, and the CL-STD combination is (100, 0.3). The blue dashed lines represent the results from the MC realizations, while the solid red line is the MC result, which is calculated based on Eq.(12). It is observed that

the results of the different realizations vary significantly with the heterogeneous permeability distributions, but tend to converge with the increasing realization numbers.

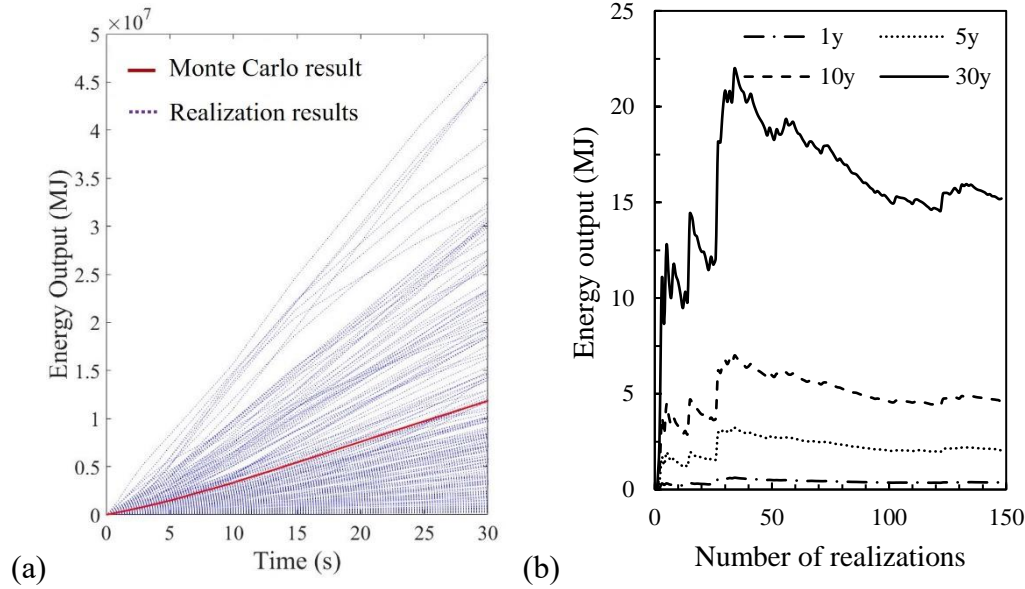


Figure 5.3. (a) Comparison of the Monte Carlo result (red line from Eq. (12)) and realization results (dashed lines) based on 150 realizations for the CL-STD combination (100, 0.3); and (b) sensitive analysis on cumulatively produced energy over realizations at different time points.

The average E_c becomes stable when the realization number grows to approximately one hundred and fifty. Thus, the realization number of 150 is selected for each CL-STD combination, and the reservoir performances are believed to reach statistical equilibrium with such a number of realizations. The Monte Carlo results with the CL-STD combination of (100, 0.3) for the other reservoir performances, i.e., temperature of production fluid (T_{out} , Eq. (7)), production $scCO_2$ saturation (S_n , Eq. (8)), $scCO_2$ production rate (M_n , Eq. (10)), and total sequestered $scCO_2$ mass (M_{co_2} , Eq. (11)), are presented in Figure 5.4.

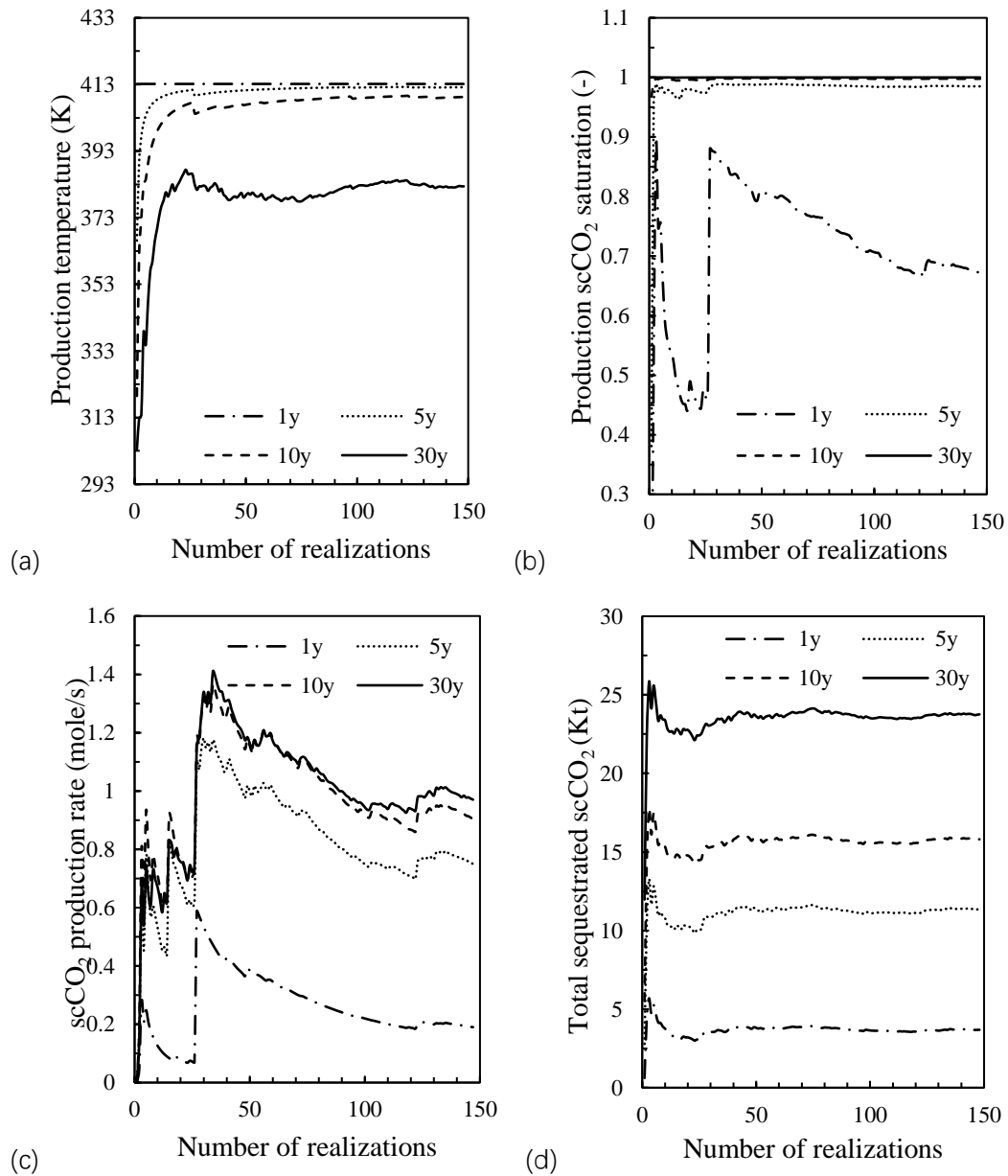


Figure 5.4. Monte Carlo results with CL-STD combination of (100, 0.3) for: (a) temperature of production fluid, (b) scCO₂ production rate, (c) total energy output, and (d) total sequestered scCO₂ mass.

5.3. Results

5.3.1 Effects of standard deviation on reservoir performances

The section presents the influence of standard deviation (STD) of heterogeneous

permeability distribution on the geothermal reservoir performances, i.e., the production scCO₂ saturation, production temperature, cumulative output energy, and sequestered CO₂ mass. The correlation length (CL) and the mean permeability (μ_K) are kept as 100 and 5×10^{-12} m².

Figure 5.5 shows an example of scCO₂ distribution at different times for the homogeneous permeability distribution and the heterogeneous permeability realizations with STD = 0.3 and 0.7, respectively. It can be observed that the realizations with different STDs have a similar scCO₂ distribution because the buoyancy force dominates the fluid flow and phase displacement (i.e., H₂O being displaced by the scCO₂). On the other hand, the unevenly distributed fluid flow across the fracture also matters. Higher STD leads to the creation of more flow pathways and disconnections in the scCO₂ plume, which have larger deviations from the homogeneous case.

The scCO₂ velocity distributions are summarized in **Figure 5.6**. Since scCO₂ has a higher flow velocity in the preferential flow pathway, here we use the scCO₂ velocity distribution to represent the scCO₂ preferential flow pathway. It is observed that during the initial production period, the buoyancy force dominates the scCO₂ movement, and the scCO₂ movement path and the preferential flow are comparably centralized. On the other hand, as shown in the middle and right parts of **Figure 5.6**, the unevenly distributed permeability leads to a significant deviation between the heterogeneous and homogeneous cases. For example, the cases with STD = 0.3 and 0.7, the scCO₂ distributed areas below the production well are obviously larger than that of the

homogeneous case. Furthermore, the case with higher STD has a larger number of preferential flow pathways, and the pathways prefer to be inside of the plume, instead of the plume edge.

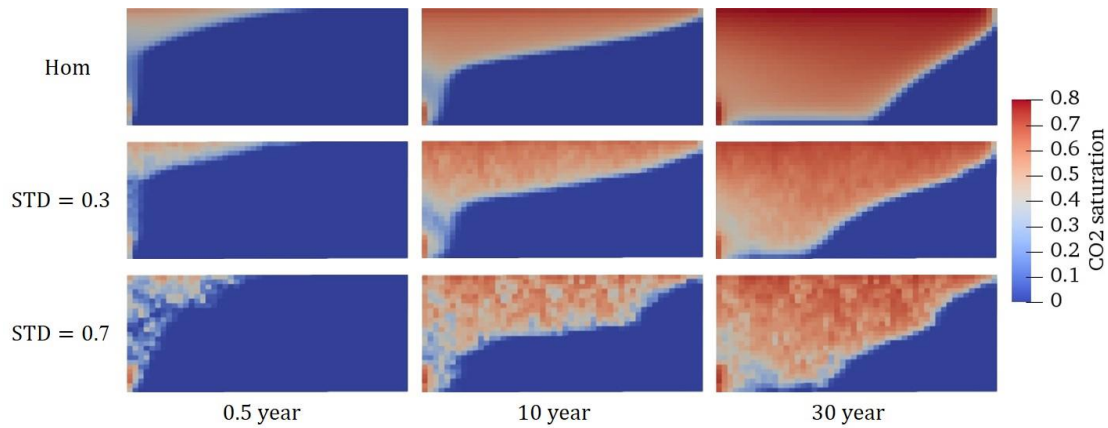


Figure 5.5. Example of scCO₂ plume spatial distributions corresponding to different STDs at 0.5th, 10th, and 30th year. The “Hom” presents the homogeneous permeability distribution. For heterogeneous permeability field, the correlation length is kept as 100.

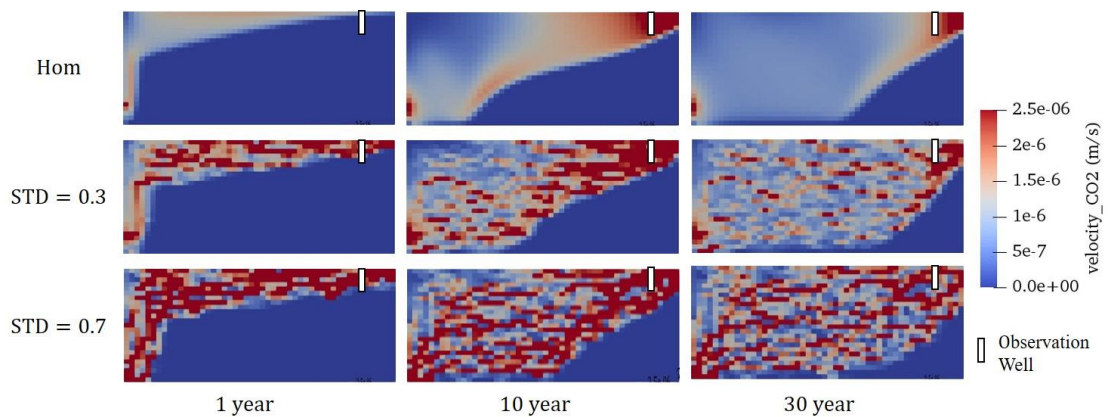


Figure 5.6. Example of scCO₂ velocity distributions with different STDs at 1st, 10th, and 30th year. The Hom presents the homogeneous permeability distribution. The high velocity areas (red areas) represent the preferential flow pathway of scCO₂. The correlation length for the heterogeneous permeability field is kept as

100.

Next, the role played by the heterogeneous permeability distribution on the geothermal reservoir performance is investigated. **Figure 5.7** presents the variation of production scCO_2 saturation (S_n) with different STD over different production period: (a) long-term, i.e., 30 years, relationship, and (b) short-term, i.e., first 3 years, relationship. It is observed that the influences of heterogeneous permeability are minimal on the production scCO_2 production for the long-term production. The S_n s are nearly identical for the homogeneous case and heterogeneous cases after the 10-year production. However, for the short-term production, the role of the unevenly distributed permeability on S_n is comparably significant. As presented in **Figure 5.7(b)**, the existing of preferential flow leads to an earlier breakthrough time of scCO_2 at production well for the heterogeneous cases. Furthermore, the production scCO_2 saturation presents a proportional relationship with the standard deviation (STD) of permeability distribution. The possible explanation is the higher STD leads to a more considerable number of preferential flows, which enhance the movement of scCO_2 toward the production well at the initial production period.

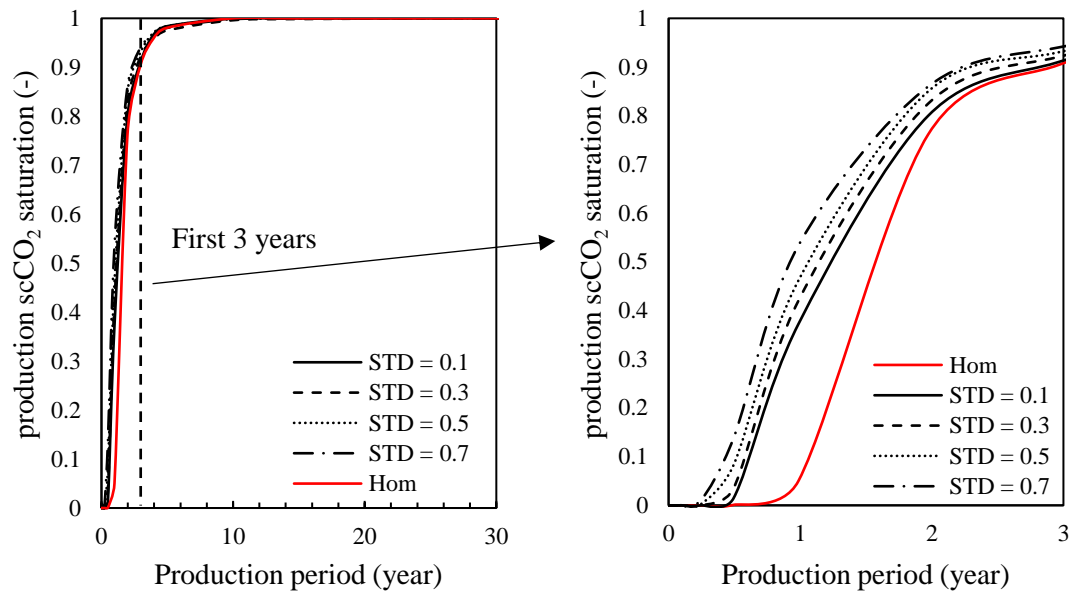


Figure 5.7. The variation of production scCO₂ saturation over the production period with different STDs: (a) long-term, i.e., 30 years, production, (b) short-term, i.e., first 3 years, production. The “Hom” in legend presents the homogeneous case.

Next, the scCO₂ production rate and the production temperature over production period for different standard deviations are investigated (see, **Figure 5.8**). It is observed that before the exceeding point, ca. 8th year, the heterogeneous permeability fields show higher scCO₂ flow velocities. This is because during the initial production period, the buoyancy forces dominate the scCO₂ flow and the plume moves fast toward the top of the reservoir. In this stage, the scCO₂ movement path is fixed and the preferential flow generated by the unevenly distributed permeability enhances the movement of scCO₂ toward the production well. As a result, the scCO₂ breakthrough time is earlier and scCO₂ flow rate is higher in heterogeneous cases than that in the homogeneous case. However, As the scCO₂ injection continues, the scCO₂ flow rate becomes lower than that in the homogeneous case. The possible reason is that the preferential flow leads to

considerably wider scCO₂ distributions than the homogeneous case, which may increase the scCO₂ movement path between the injection well and production well, reducing the scCO₂ production rate.

It is observed from **Figure 5.8(b)** that the heterogeneous permeability distribution leads to a later temperature breakthrough time than in the homogeneous permeability case.

This is because the preferential flow paths can accelerate the cold scCO₂ movement toward the production well, decreasing the time the scCO₂ and the surrounding rock matrix are in contact. Thus, the cold scCO₂ cannot be adequately heated during the period traveling to the production well compared to the homogeneous case, resulting in the earlier arrival of the cooling front at the production well. On the other hand, the wider scCO₂ distribution caused by the preferential flow pathway means that the cold scCO₂ can be heated by a larger rock area, which retards the temperature drop at the production well. Thus, the T_{out} from homogeneous permeability field becomes lower than the other cases after approximately 28-year heat production.

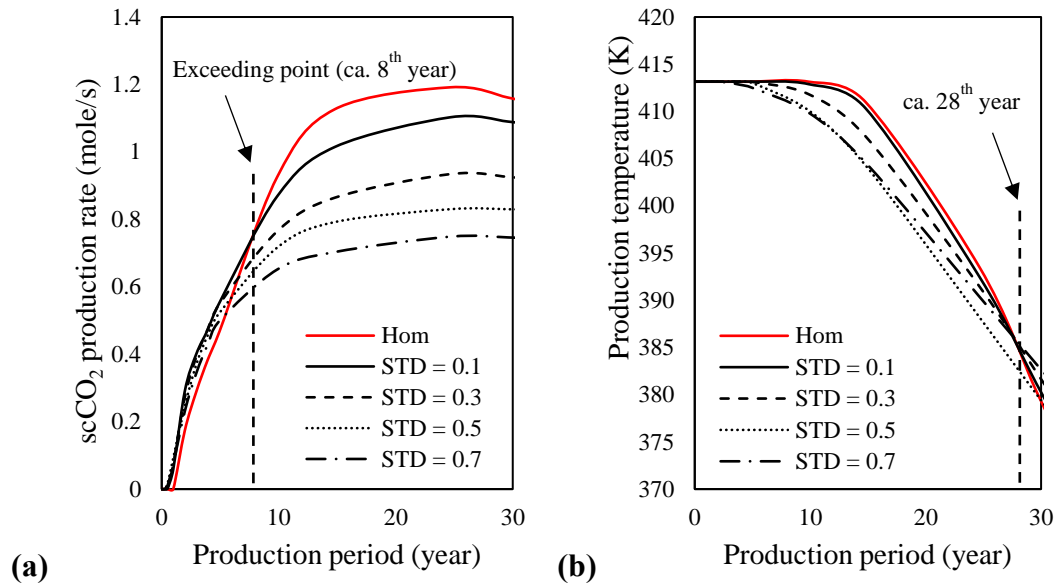


Figure 5.8. (a) scCO₂ production rate, and (b) production temperature over production period with different standard deviation (“STD” in the legend, and “Hom” represents the homogeneous permeability field). The correlation length is kept as 100.

Figure 5.9 presents (a) cumulative produced energy (E_c) and (b) sequestered scCO₂ mass over production period with various STD. Since the scCO₂ production rate dominates the reservoir energy production rate, the E_c presents the same tendency as the scCO₂ production rate, i.e., the E_c is proportional to the STD of permeability distribution for the very initial production period (the homogeneous permeability is regarded as STD= 0), but shows an inversely proportional relationship with STD for the long-term production. It is observed in **Figure 5.9(b)** that the total sequestered scCO₂ mass presents an inversely proportional relationship with the standard deviation of heterogeneous permeability field. This can be explained by that as the scCO₂ flow rate increases, the residence time of scCO₂ in the porous media is reduced, as well as,

the amount of the trapped scCO₂.

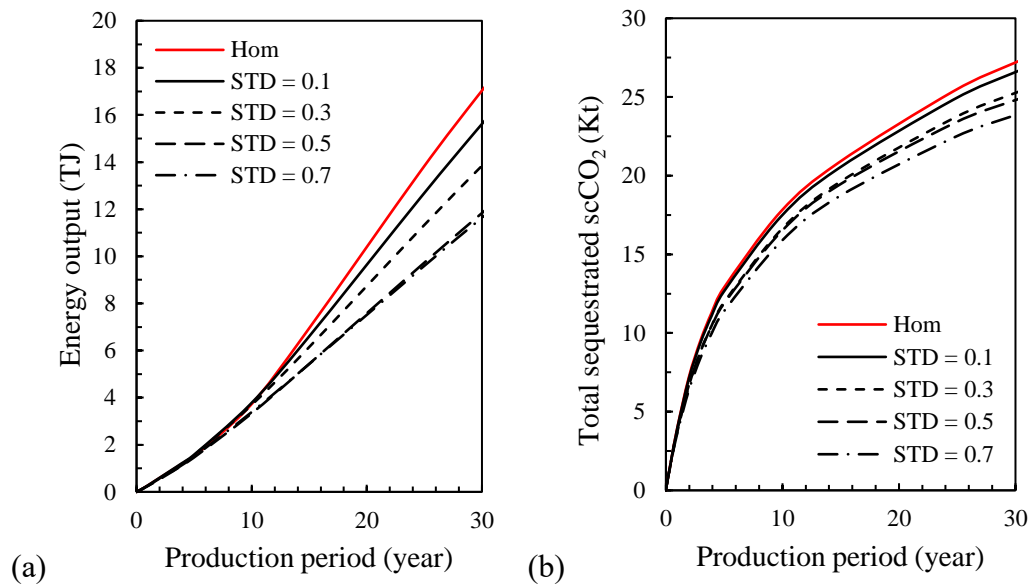


Figure 5.9. The relationship of (a) Cumulative produced energy and (b) the total sequestered scCO₂ mass with production period with different STD, “Hom” donates the homogeneous permeability field. The correlation length is kept as 100.

5.3.2 Effects of the correlation length on the reservoir performance

The section presents the influence of correlation length (CL) of heterogeneous permeability distribution on the geothermal reservoir performance. The standard deviation (STD) and the mean permeability (μ_K) are kept as 0.3 and $5 \times 10^{-12} \text{ m}^2$. The relationships between the performances from homogeneous and heterogeneous permeability fields are consistent with the results in the former section, and are not furtherly discussed here.

Figure 5.10 illustrates the distributions of preferential flow path, which is presented by scCO₂ velocity. Compared to standard deviation, the enlargement of correlation length does not significantly increase the number of preferential flow path, but the length is

obviously prolonged. As presented in the middle part of **Figure 5.10** (10th year), the areas with high scCO₂ velocity are disjointed for the case with CL = 50 and 100, while the areas for the case with CL = 200 are nearly connecting injection and production wells. On the other hand, the scCO₂ movement is considerably enhanced by the longer preferential flow path. At the end of the first year, the scCO₂ plume for the case with CL = 200 is going to arrive the production well. However, the that for the cases with lower CL only reach to half of the geothermal reservoir.

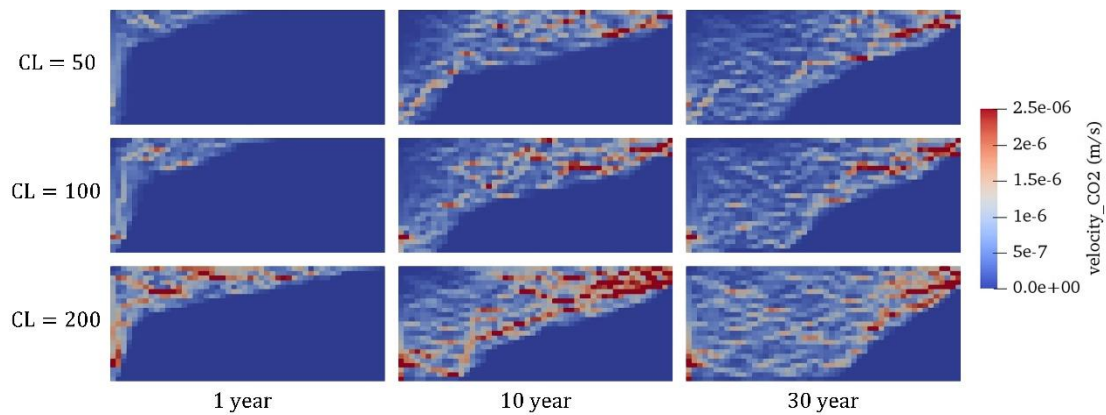


Figure 5.10. Example of scCO₂ velocity distributions with different CLs at 1st, 10th, and 30th year. The high velocity areas (red areas) represent the preferential flow pathway of scCO₂. The STD for the heterogeneous permeability field is kept as 0.3.

Figure 5.11 presents the variation of the production scCO₂ saturation (S_n) over the production period with different correlation lengths (CLs) of heterogeneous permeability distribution for (a) long-term, i.e., 30 years, production, and (b) short-term, i.e., first 3 years, production. It is observed that the long-term S_n -CL relationship is identical with standard deviation, in which the effects of CL on S_n are minimal for the

long-term production. Moreover, the S_n is also proportional to the CL during the initial production period, in which the $scCO_2$ breakthrough time shows an inversely proportional relationship with CL, as presented in **Figure 5.11(b)**. The possible reason is presented in **Figure 5.10**, i.e., the $scCO_2$ flow rate is furtherly accelerated by the longer preferential flow, which is due to the larger CL, compared to the homogeneous case and cases with lower CL.

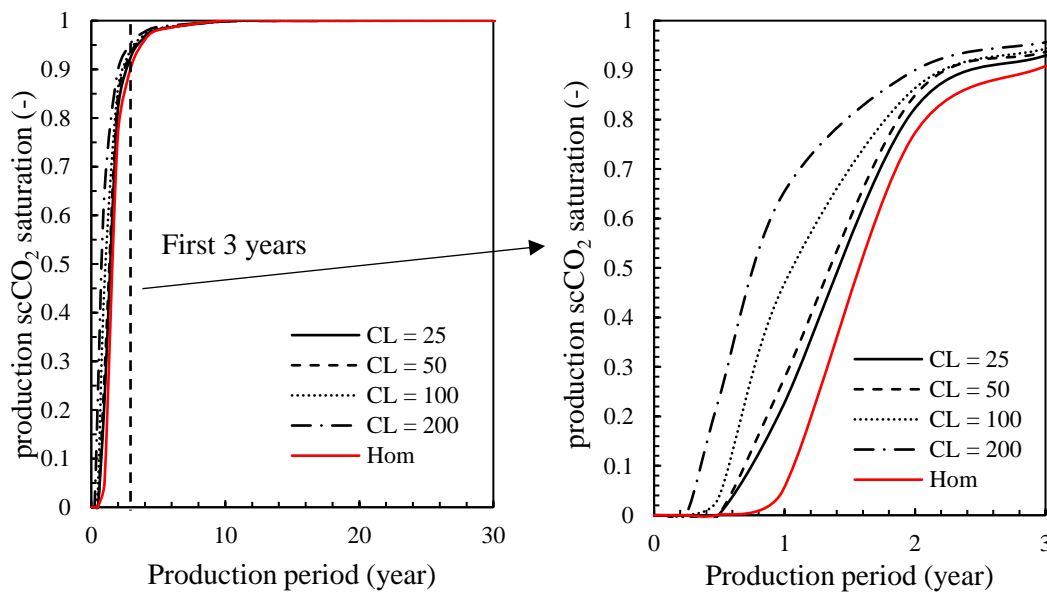


Figure 5.11. (a) Relationship between $scCO_2$ saturation at production well and production period with different correlation length of gauss distribution; and (b) Relationship between $scCO_2$ saturation at production well and correlation length at different time points. The standard deviation is kept as 0.3.

Figure 5.12 presents the relationships of (a) $scCO_2$ production rate and (b) production temperature with production period with CL = 25, 50, 100, and 200, in which the proportional relationship between $scCO_2$ production rate and CL can be observed. The $scCO_2$ production rate of the case with CL = 200 is largest and closest to the

homogeneous case for the long-term production, which corresponds to the definition of the correlation length, i.e., within the correlation length, the permeability is nearly unchanged. A step further, the ranked scCO₂ production rates result in the proportional relationship between production temperature and CL as presented in **Figure 5.12(b)**. The production temperatures maintain the same order until the end of the simulation.

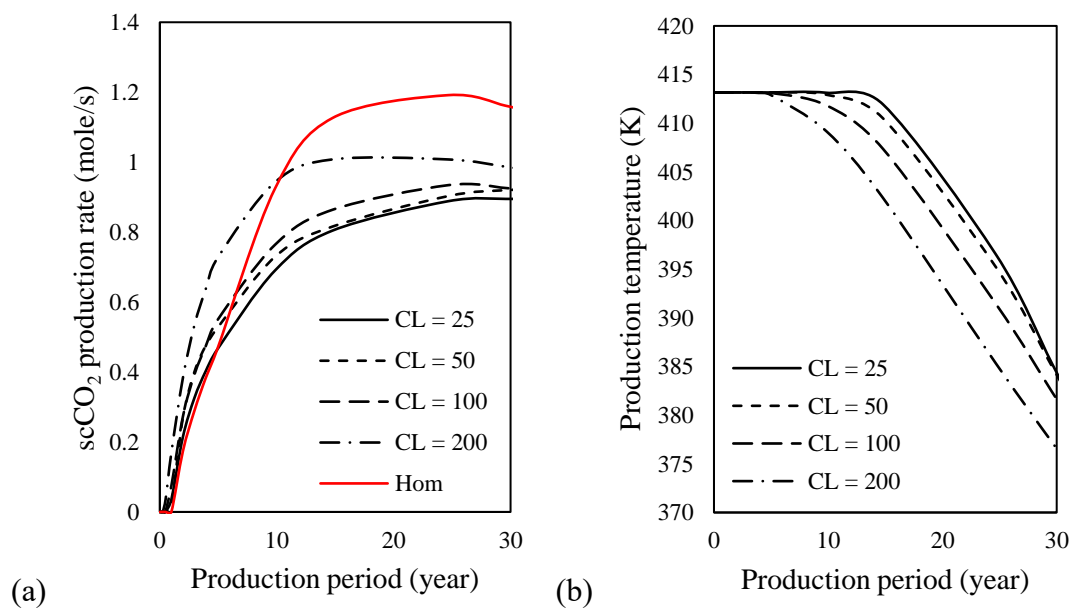


Figure 5.12. Variation of (a) scCO₂ production rate and (b) production temperature per time as a function of CL. The STD is kept as 0.3.

Figure 5.13 presents the relationship of (a) cumulative produced energy (E_c) and (b) the total sequestered scCO₂ mass with production period with different correlation lengths (CLs) It is observed in **Figure 5.13(a)** that the case with CL = 200 has the largest E_c , while that of the case with CL = 25 is the lowest during the entire production period. The reason is discussed before, and not presented in this section. In contrast to the standard deviation (STD), CL shows to have little influence on the amount of

sequestered scCO_2 (M_{CO_2}) over the production period (**Figure 5.13(b)**).

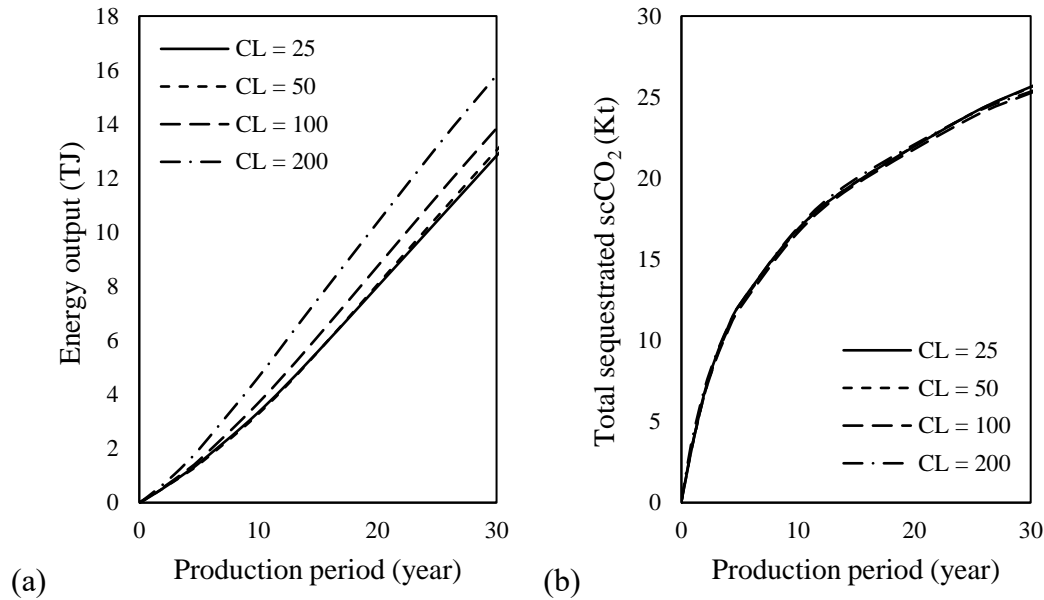


Figure 5.13. The variation of (a) cumulative produced energy and (b) total mass of sequestered scCO_2 over the production period for different CL. The STD is kept as 0.3.

5.3.3. Effects of the type of working fluid on reservoir performance

In this section, the performances of the reservoir using scCO_2 , i.e., $\text{scCO}_2\text{-H}_2\text{O}$ combined EGS, and H_2O , i.e., H_2O -saturated EGS, as working fluids are investigated and compared. Here, except the working fluid, the other parameters and boundary conditions are kept exactly the same for the two kinds of reservoirs, as presented in **Table 5.1** and **Figure 5.1**.

Figure 5.14 compares the cumulative produced energy of the two geothermal reservoirs having a homogeneous permeability, i.e., $5 \times 10^{-12} \text{ m}^2$. It is observed that with the same injection and production pressures, the scCO_2 reservoir produces much more

considerable energy, i.e., nearly three times larger, than H₂O reservoir. This is because scCO₂ has lower viscosity and density than that of H₂O, i.e., ca. $31.8 \times 10^{-6} \text{ Pa} \cdot \text{s}$ and 327 kg/m^3 for scCO₂ compared to $140 \times 10^{-6} \text{ Pa} \cdot \text{s}$ and 881 kg/m^3 for H₂O. According to Eq. (2), scCO₂ has a larger flow rate, and as a result, a better energy performance than H₂O.

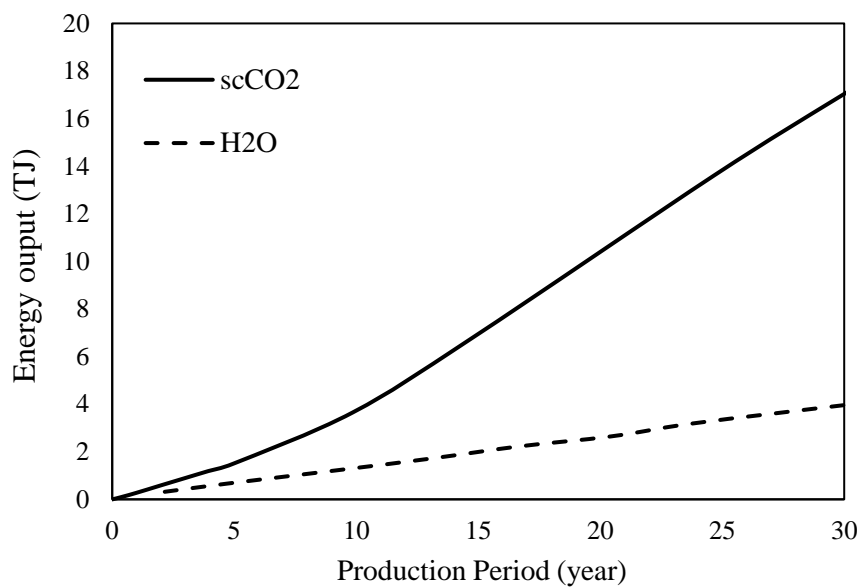


Figure 5.14. Comparison of the cumulative energy produced over the entire production period of a geothermal reservoir using scCO₂ and H₂O as working fluids. The permeability is isotropic and homogeneous.

Figure 5.15 depicts the energy variations in homogeneous and heterogeneous permeability fields with different standard deviations (STD) and correlation lengths (CL). The energy variations (V_E , see Eq. (13)) in the 1st year, 10th year, 15th year, and 30th year are presented. It is observed that the standard deviation and correlation length of the permeability field have the same effects on reservoir energy performance

between the two-phase scCO₂-H₂O combined EGS and the single-phase H₂O-saturated EGS, i.e., the reservoir performs worse with increasing standard deviation and decreasing correlation length. The same observation has been obtained in Zhou et al., 2022 using the model with a discrete fracture network [5]. On the other hand, it should be noted that for the CO₂-H₂O combined EGS, the influences of standard deviation and correlation length significantly vary with production proceeding, but their effects in H₂O-saturated EGS are irrelevant on production period. For long-term production, the energy variations (V_E) between the cases with homogeneous and heterogeneous permeability fields become much more considerable. For example, provided that the standard deviation is 0.7 and the correlation length is 100, in the first year, the maximum V_E is around -5%, but in the 30th year, V_E reaches to -30%, which indicates the unevenly distributed permeability leads to a more inferior reservoir energy performance for the long-term production. The relationship between V_E and production period can be explained by that in two-phase scCO₂-H₂O combined EGS, the scCO₂ distribution enlarges with the production period. In this case, a larger number of preferential flow path is involved into scCO₂ movement, which prevents scCO₂ to flow toward the production well. On the other hand, in H₂O-saturated EGS, without the engagement of buoyance force, the flow direction is fixed during the initial production period, and is nearly unchanged with the production proceeding. Thus, the V_E in H₂O-saturated EGS is independent of production period.

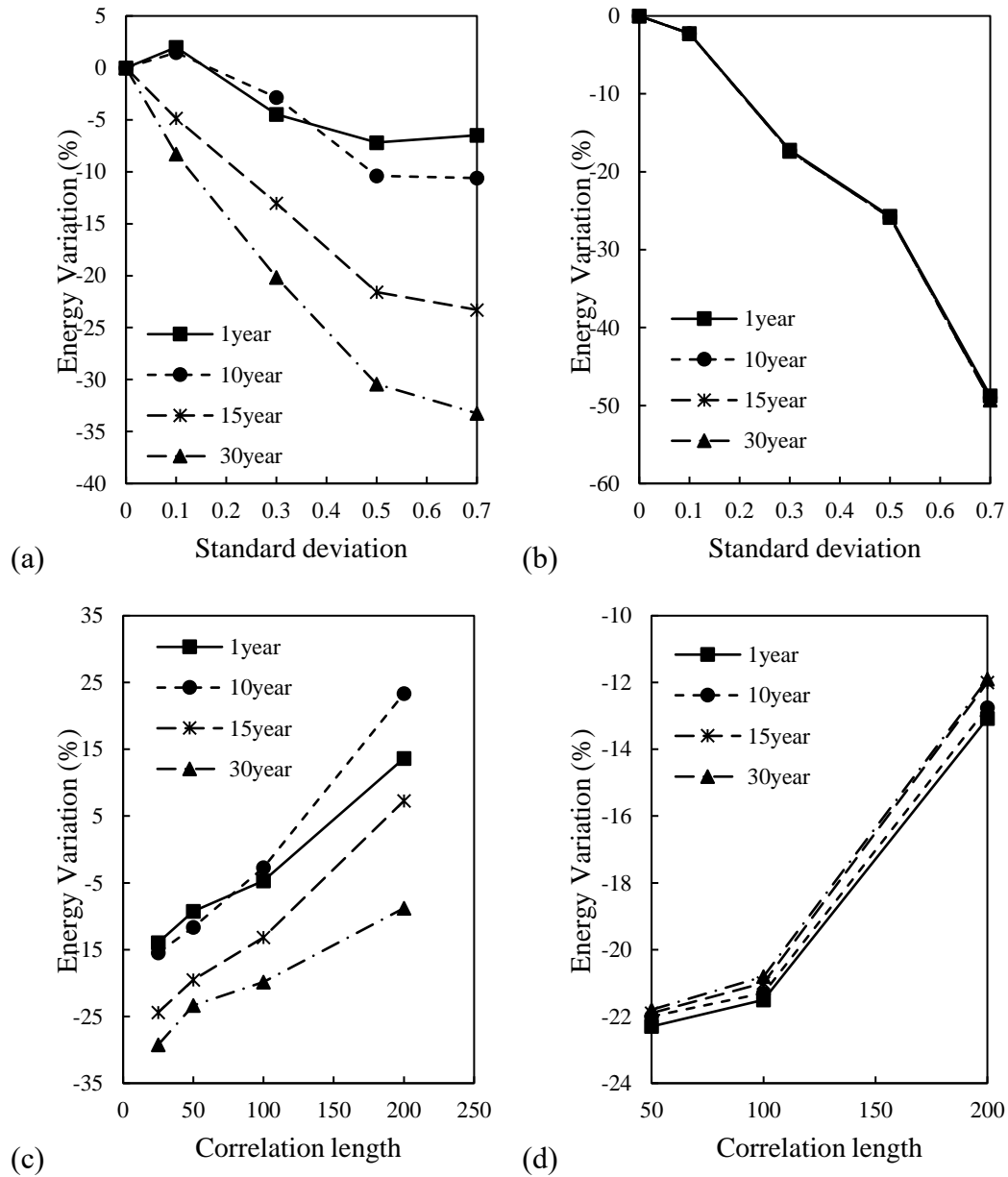


Figure 5.15. Relationships among energy variation, STD and CL in different production periods for (a) scCO₂-H₂O combined EGS, (b) H₂O-saturated EGS, (c) scCO₂-H₂O combined EGS, and (d) H₂O-saturated EGS.

5.4. Conclusion

In this work, a two-phase two-dimensional thermal-hydraulic (TM) coupled model with heterogeneous permeability field is implemented using the open-source software,

DuMu^X. The influences of preferential flow pathways existing in heterogeneous permeability fields on the geothermal reservoir performances, i.e., the scCO₂ saturation at production well, production temperature, cumulative produced energy, and the sequestered scCO₂ mass, are investigated. The correlation length (CL) and standard deviation of permeability distribution (STD) are the two variables under investigation. The Monte Carlo method is applied to avoid the interference from the randomly generated heterogeneous permeability distribution. For each CL-STD combination, one hundred and fifty realizations are generated and simulated to ensure the reservoir performances reach statistical equilibrium. Based on the simulation results, the following conclusions can be obtained:

1. The unevenly distributed permeability generated preferential flow has limited influence on scCO₂ movement. The shapes of scCO₂ distributions are similar between homogeneous case and heterogeneous cases, and the long-term production The scCO₂ saturation (S_n) is independent on the heterogeneous permeability field. However, for the short-term production, S_n is proportional to the standard deviation and correlation length of permeability distribution.
2. The unevenly distributed permeability enhanced the energy production rate during the initial production period, but it leads to a reduction of the reservoir energy performance for the long-term production. Moreover, the long-term cumulatively produced energy and the total sequestered scCO₂ mass both present the inversely proportional relationship with standard deviation of the heterogeneous permeability field.

3. The longer correlation length results in a more considerable output energy during the entire production period. However, the reservoir performance in terms of scCO₂ sequestration is independent of the correlation length.
4. Under the same injection and production pressure, using H₂O as working fluid leads to a much lower output energy, i.e., only approximately 25%, compared to the reservoir using scCO₂ as working fluid. Furthermore, the influences of standard deviation and correlation length vary with the production proceeding for the reservoir using scCO₂ as working fluid. On the other hand, for the reservoir whose working fluid is H₂O, the influences are independent of the production period.
5. The heterogeneous aperture distribution of the conducting fracture results in considerably and slightly inferior reservoir performance in terms of energy output and scCO₂ sequestration. Thus, if possible, an unevenly distributed fracture permeability should be avoided during the creation of geothermal reservoir.

Acknowledgements

This work acknowledges financial support from the China scholarship council (CSC).

Reference

- [1] G. Hutterer, "Geothermal Power Generation in the World 2015-2020 Update Report," p. 17.
- [2] S.-M. Lu, "A global review of enhanced geothermal system (EGS)," *Renew. Sustain. Energy Rev.*, vol. 81, pp. 2902–2921, Jan. 2018, doi: 10.1016/j.rser.2017.06.097.
- [3] J. W. Lund, L. Bjelm, G. Bloomquist, and A. K. Mortensen, "Characteristics, development and utilization of geothermal resources, – a Nordic perspective,"

- Episodes*, vol. 31, no. 1, pp. 140–147, 2008, doi: <https://doi.org/10.18814/epiiugs/2008/v31i1/019>.
- [4] International Energy Agency, “Key World Energy Statistics 2019”, doi: <https://doi.org/10.1787/71b3ce84-en>.
- [5] D. Zhou, A. Tatomir, A. Niemi, C.-F. Tsang, and M. Sauter, “Study on the influence of randomly distributed fracture aperture in a fracture network on heat production from an enhanced geothermal system (EGS),” *Energy*, vol. 250, p. 123781, Jul. 2022, doi: 10.1016/j.energy.2022.123781.
- [6] P. Olasolo, M. C. Juárez, M. P. Morales, S. D’Amico, and I. A. Liarte, “Enhanced geothermal systems (EGS): A review,” *Renew. Sustain. Energy Rev.*, vol. 56, pp. 133–144, Apr. 2016, doi: 10.1016/j.rser.2015.11.031.
- [7] G. Kosakowski, B. Berkowitz, and H. Scher, “Analysis of field observations of tracer transport in a fractured till,” *J. Contam. Hydrol.*, vol. 47, no. 1, pp. 29–51, Jan. 2001, doi: 10.1016/S0169-7722(00)00140-6.
- [8] Y. Méheust and J. Schmittbuhl, “Flow enhancement of a rough fracture,” *Geophys. Res. Lett.*, vol. 27, no. 18, pp. 2989–2992, Sep. 2000, doi: 10.1029/1999GL008464.
- [9] C. Zhang *et al.*, “Effects of the spatial heterogeneity in reservoir parameters on the heat extraction performance forecast based on a 3D thermo-hydro-mechanical coupled model: A case study at the Zhacang geothermal field in the Guide basin, northeastern Tibetan plateau,” *Geothermics*, vol. 95, p. 102161, Sep. 2021, doi: 10.1016/j.geothermics.2021.102161.
- [10] D. B. Fox, D. L. Koch, and J. W. Tester, “The effect of spatial aperture variations on the thermal performance of discretely fractured geothermal reservoirs,” *Geotherm. Energy*, vol. 3, no. 1, p. 21, Dec. 2015, doi: 10.1186/s40517-015-0039-z.
- [11] K. Pruess, “Enhanced geothermal systems (EGS) using CO₂ as working fluid—A novel approach for generating renewable energy with simultaneous sequestration of carbon,” *Geothermics*, vol. 35, no. 4, pp. 351–367, Aug. 2006, doi: 10.1016/j.geothermics.2006.08.002.
- [12] K. Pruess, “On production behavior of enhanced geothermal systems with CO₂ as working fluid,” *Energy Convers. Manag.*, vol. 49, no. 6, pp. 1446–1454, Jun. 2008, doi: 10.1016/j.enconman.2007.12.029.
- [13] A. Borgia, K. Pruess, T. J. Kneafsey, C. M. Oldenburg, and L. Pan, “Simulation of CO₂-EGS in a Fractured Reservoir with Salt Precipitation,” *Energy Procedia*, vol. 37, pp. 6617–6624, 2013, doi: 10.1016/j.egypro.2013.06.594.
- [14] C.-L. Wang, W.-L. Cheng, Y.-L. Nian, L. Yang, B.-B. Han, and M.-H. Liu, “Simulation of heat extraction from CO₂-based enhanced geothermal systems considering CO₂ sequestration,” *Energy*, vol. 142, pp. 157–167, Jan. 2018, doi: 10.1016/j.energy.2017.09.139.
- [15] A. D. Atrens, H. Gurgenci, and V. Rudolph, “Economic Optimization of a CO₂-Based EGS Power Plant,” *Energy Fuels*, vol. 25, no. 8, pp. 3765–3775, Aug. 2011, doi: 10.1021/ef200537n.
- [16] A. Borgia *et al.*, “Simulations of CO₂ injection into fractures and faults for improving their geophysical characterization at EGS sites,” *Geothermics*, vol. 69,

- pp. 189–201, Sep. 2017, doi: 10.1016/j.geothermics.2017.05.002.
- [17] M. Th. van Genuchten, “A Closed-form Equation for Predicting the Hydraulic Conductivity of Unsaturated Soils,” *Soil Sci. Soc. Am. J.*, vol. 44, no. 5, pp. 892–898, Sep. 1980, doi: 10.2136/sssaj1980.03615995004400050002x.
- [18] R. Helmig, *Multiphase Flow and Transport Processes in the Subsurface: A Contribution to the Modeling of Hydrosystems*. 1997.
- [19] T. A. Davis, “Algorithm 832: UMFPACK V4.3---an unsymmetric-pattern multifrontal method,” *ACM Trans. Math. Softw.*, vol. 30, no. 2, pp. 196–199, Jun. 2004, doi: 10.1145/992200.992206.
- [20] F. Gong *et al.*, “Evaluation of geothermal energy extraction in Enhanced Geothermal System (EGS) with multiple fracturing horizontal wells (MFHW),” *Renew. Energy*, vol. 151, pp. 1339–1351, May 2020, doi: 10.1016/j.renene.2019.11.134.
- [21] T. Guo, F. Gong, X. Wang, Q. Lin, Z. Qu, and W. Zhang, “Performance of enhanced geothermal system (EGS) in fractured geothermal reservoirs with CO₂ as working fluid,” *Appl. Therm. Eng.*, vol. 152, pp. 215–230, Apr. 2019, doi: 10.1016/j.applthermaleng.2019.02.024.
- [22] Z. Sun, “Numerical simulation of the heat extraction in EGS with thermal-hydraulic-mechanical coupling method based on discrete fractures model,” *Energy*, vol. 120, pp. 20–33, 2017, doi: <https://doi.org/10.1016/j.energy.2016.10.046>.
- [23] International Association for the Properties of Water and Steam, IAPWS R7-97(2012), “Revised Release on the IAPWS Industrial Formulation 1997 for the Thermodynamic Properties of Water and Steam (The revision only relates to the extension of region 5 to 50 MPa)”.
- [24] R. Span and W. Wagner, “A New Equation of State for Carbon Dioxide Covering the Fluid Region from the Triple-Point Temperature to 1100 K at Pressures up to 800 MPa,” *J. Phys. Chem. Ref. Data*, vol. 25, no. 6, pp. 1509–1596, Nov. 1996, doi: 10.1063/1.555991.
- [25] C.-F. Tsang and I. Neretnieks, “Flow channeling in heterogeneous fractured rocks,” *Rev. Geophys.*, vol. 36, no. 2, pp. 275–298, May 1998, doi: 10.1029/97RG03319.
- [26] Y. W. Tsang and C. F. Tsang, “Channel model of flow through fractured media,” *Water Resour. Res.*, vol. 23, no. 3, pp. 467–479, Mar. 1987, doi: 10.1029/WR023i003p00467.
- [27] B. Guo, P. Fu, Y. Hao, C. A. Peters, and C. R. Carrigan, “Thermal drawdown-induced flow channeling in a single fracture in EGS,” *Geothermics*, vol. 61, pp. 46–62, May 2016, doi: 10.1016/j.geothermics.2016.01.004.
- [28] M. Bonnet *et al.*, “Determining Crack Aperture Distribution in Rocks Using the ¹⁴C-PMMA Autoradiographic Method: Experiments and Simulations,” *J. Geophys. Res. Solid Earth*, vol. 125, no. 1, Jan. 2020, doi: 10.1029/2019JB018241.
- [29] S. P. Bertels, D. A. DiCarlo, and M. J. Blunt, “Measurement of aperture distribution, capillary pressure, relative permeability, and in situ saturation in a rock fracture using computed tomography scanning,” *Water Resour. Res.*, vol. 37, no. 3, pp. 649–662, Mar. 2001, doi: 10.1029/2000WR900316.

- [30] E. J. Pebesma, “Multivariable geostatistics in S: the gstat package,” *Comput. Geosci.*, vol. 30, no. 7, pp. 683–691, Aug. 2004, doi: 10.1016/j.cageo.2004.03.012.
- [31] B. Gräler, E. Pebesma, and G. Heuvelink, “Spatio-Temporal Interpolation using gstat,” *R J.*, vol. 8, no. 1, p. 204, 2016, doi: 10.32614/RJ-2016-014.

Chapter 6.

Conclusion and Outlook

6.1. Conclusion

The development of the enhanced geothermal system (EGS) makes geothermal energy one of the renewable energy having the potential to solve the global energy shortage and global warming. Improved understanding of fluid flow and heat transfer within discrete fracture networks helps to design the EGS reservoirs to obtain a higher energy performance. The simulation of fluid flow within an EGS reservoir is considerably complex due to the complicated multiphase system and high heterogeneity of fracture networks. The reliability of the numerical method depends on the appropriate representation of the fractured zones and fracture network within rocks.

The doctor's thesis, based on the numerical simulations, is structured to six chapters. In which chapters 2, 3, 4, and 5 are the primary research for the doctoral thesis. In chapter 2, the thermal-hydraulic-mechanical effects among different fracture zones are investigated. In chapter 3, a novel representation of the discrete fracture network is proposed, and the effects of aperture distribution on EGS reservoir performance are studied. In chapter 4, the possibility of using scCO₂ as working fluid for EGS reservoir is addressed, and three different EGS setups are raised and compared. In Chapter 5, provided that the scCO₂ is the working fluid, the roles of geochemical reactions between scCO₂ and minerals and water evaporation played on EGS reservoir performance are discussed.

The primary conclusions can be summarized as follows:

6.1.1. The effects of multi-fracture zones on EGS reservoir performance

1. The production temperature is affected by fracture zone spacing and location, but only in a limited water, i.e., a lower spacing result in a lower production temperature. The production temperature of middle fracture zone is lower than that of side fracture

zones. However, during the first period (approx. 2000d), there is almost no difference in temperatures.

2. The multi-fracture zone system can effectively extend the service lifespan of the EGS compared to the single fracture system. The heat production rate and average produced energy are proportional to the number of fracture zones. Additionally, a larger spacing between the neighbouring fracture zones leads to a higher heat production rate.

3. A larger flow rate results in higher initial pressure difference values, which are subsequently followed by a steeper reduction. Due to the hydraulic-mechanical effects, the pressure difference from a larger flow rate can be lower than that from a lower flow rate. The final production temperature and breakthrough time have an inversely proportional relationship with the flow rate.

6.1.2. The influences of DFNs properties on EGS reservoir performance

1. The variation coefficient of fracture aperture plays a critical role in evaluating the performance of a geothermal reservoir. The performance can be divided into three stages depending on the variation coefficient: at the low and high variation coefficient stage, the average heat production rates keep at a nearly constant level, while at middle variation coefficient stage, the average heat production rates sharply reduce.

2. The increase of average heat production rate with the average fracture aperture is highly related to the variation coefficient. The high variation coefficient inhibits the effects from average fracture aperture, resulting in the lower growth of average heat production rate compared to the low variation coefficient.

3. The average heat production rate (A_r) has a linear relationship with fracture density (ρ_{21}). Their relationship is proportional to average fracture aperture: the higher average fracture aperture leads to a more considerable growth rate of the average heat production rate. Additionally, their relationship is also related to the variation coefficient. The slopes of A_r - ρ_{21} curves are inversely proportional to the variation coefficient.

4. The increase heat production rate of an existing geothermal reservoir with the discrete fracture network can be achieved by the enlargement of fracture density or aperture.

Provided that the base value of aperture is 0.3 mm and of density is 0.0121 1/m, the performance from enlarging DFN aperture is obviously better than creating new fractures.

6.1.3. The advantage of scCO₂ as working fluid of EGS reservoir over H₂O

1. The EGS using scCO₂ as working fluid significantly differ from that using H₂O as working fluid. The cold plume in H₂O-saturated EGS migrates much faster than the scCO₂ based EGS.
2. With a given injection rate, the production temperature of the EGS reservoirs using scCO₂ as working fluid keeps at a constant level during the 30-year heat production, while the production temperature of the H₂O saturated EGS starts to decrease from approximately year five onwards.
3. The injection rate highly affects heat production rates and production temperatures. With a higher injection rate, the total produced thermal energy and lifespan of H₂O saturated EGS display sharp drops because of the decrease in production temperature. On the other hand, the reservoirs with scCO₂ as working fluid perform better at higher injection rates; the total produced geothermal energy shows a considerable increase while the reservoir lifespan are kept nearly unchanged.
4. The decrease in production temperature of the reservoirs with scCO₂ as working fluid is considerably more significant than that of H₂O-saturated EGS before the thermal breakthrough.

6.1.4. The role of preferential flow path on the performance of EGS reservoir using scCO₂ as working fluid.

1. The flow channeling induced growth in fluid mass flow rate leads to the linear reductions of production scCO₂ saturation with the CL and σ_K . On the other hand, the production temperature has an earlier breakthrough time compared to the homogeneous cases, whose permeability is isotropic and homogeneous.
2. During the initial production period, buoyance determines the fluid flow, and the fluid flow rate is proportional to both CL and σ_K . However, as the production continues,

the buoyance effect diminishes, and partial scCO₂ starts to congregate beneath the production well, which cannot be effectively extracted. Thus, the scCO₂ production rate has a reduction with the wider scCO₂ distribution, i.e., the larger σ_K , which decreases the heat production rate as well as the cumulative produced energy.

3. the larger CL only extends the preferential flow pathway and increases the scCO₂ production rate. As a result, the cumulative produced energy shows a proportional relationship with CL during the entire production rate.

4. The scCO₂ distribution plays a role in the sequestered scCO₂ mass. The larger σ_K leads to the more sequestered mass of scCO₂, but it presents an irrelevance with the CL.

5. The reservoir using scCO₂ as working fluid performs better than that whose working fluid is H₂O. In H₂O-saturated EGS, the flow rate reaches equilibrium in a very short time. Thus, the energy variation between the case with homo- and heterogeneous permeability fields is independent of the production period.

6.1.5. General conclusion of the thesis

The performances of EGS reservoirs are highly dependent on the properties of the fractures. Generally, the larger fracture zone area and the fracture density can significantly promote the geothermal reservoir energy production ability. On the other hand, the heterogeneity of fracture apertures also plays a critical role in the EGS reservoir heat production rate. Provided that the apertures follow the normal distribution, with the increase of aperture standard deviation, the reservoir heat production rate initially reduces, then stables at a nearly constant level. Compared to increasing the fracture zone or fracture density, the enlargement of the fracture aperture is a more effective method to promote the EGS reservoir energy performance for an existing EGS reservoir.

The employment of scCO₂ as EGS working fluid presents many strengths over H₂O, including the higher energy production rate, high production temperature, and later temperature breakthrough time. Another advantage is that during the working circulation, part of the scCO₂ is sequestered in the reservoir, which is a benefit to

inhibiting the tendency of global warming. In addition, the existence of the preferential flow pathway within the heterogeneous permeability field enhances the scCO₂ migration toward to the production well, which increase the scCO₂ flow rates and the reservoir energy performance. However, because the extraction area of production well is limited, a more considerable number of preferential flow pathways leads to a wider scCO₂ distribution, such that the scCO₂ production rate is reduced, leading to a worse reservoir energy performance.

6.2. Current research and Outlook

6.2.1. Current research

The current work investigates the effects of the fracture aperture variation caused by the changes in pore pressure and temperature on the performance of the fractured porous geothermal reservoir. The two-phase single-dimensional model is applied to investigate the thermal-hydraulic-mechanical (THM) coupled effects with the Monte Carlo method. The THM model is simplified based on the former benchmark conclusion, i.e., only the fracture displacement is considered while the strain of the surrounding rock matrix is neglected. The influence of the preferential flow pathway within the heterogeneous permeability on the THM effects is also studied based on the open-source software Gstat.

6.2.2. Outlook

One of the primary purposes of numerical modelling is to simulate the multi-physical processes in the fractured porous media and provide reliable predictions and suggestions for the EGS design. However, due to the complexity and high heterogeneity of fracture networks, the accuracy of the current numerical simulations is unsatisfactory. Thus, finding a reliable method to predict the performance of EGS reservoirs is the purpose of further research.

The development of computer technology makes the statistical scale simulations of physical processes underground possible. Based on the published results and the current

work, the variables at injection well and production well, i.e., fluid flux, pressure, temperature, phase saturation, breakthrough time of temperature and phase, are related to the underground structures. The further work is going to look for the relationships among the variables by statistical method with the following steps:

1. Developing the two-phase three-dimensional (3D) numerical model with discrete fracture network, which considers the fracture aperture distribution and fracture surface roughness, and using the Monte Carlo method to investigate the effects of fracture network randomness on the EGS performances.
2. Employing statistical methods to look for the relationships among the variables at the injection well, observation wells, and the production well, and find the empirical equations to predict the EGS performances.
3. Combining the laboratory-scale experiments and field-scale experiments to verify the conclusions of numerical investigations.